Perturbation Dynamics and Impact of Different Perturbation Methods in Tropical Cyclone Ensemble Forecasting

Zur Erlangung des akademischen Grades eines
DOKTORS DER NATURWISSENSCHAFTEN
von der Fakultät für Physik des
Karlsruher Institut für Technologie

genehmigte

DISSERTATION

von

Dipl.-Met. Simon T. K. Lang
aus Aachen

Tag der mündlichen Prüfung:	28 Oktober 2011
Referent:	Prof. Dr. Sarah C. Jones
Korreferent:	Prof. Dr. Christoph Kottmeier

Abstract

Tropical cyclones pose a serious threat to human lives and property. However, tropical cyclone forecasts are still associated with large uncertainties, which result from both uncertainty of the initial conditions and errors of the forecast model. Ensemble prediction systems are used to quantify the uncertainties associated with a forecast . In the operational configuration of the ensemble prediction system of the European Centre for Medium-Range Weather Forecasts different methods are applied to account for initial condition and model uncertainty. Singular vectors, also known as optimal perturbations, and an ensemble of data assimilations are used to generate perturbations to the initial conditions. Two stochastic tendency perturbation schemes aim to mimic model errors: the stochastic kinetic energy backscatter scheme and the stochastically perturbed parametrisation tendency scheme. Detailed knowledge of the properties of the different perturbation methods is highly relevant for future configurations of the ensemble prediction system. In this study we explored the dynamics and the impact of the different perturbation methods for tropical cyclone forecasts.

In the first part of the study the sensitivity of singular vectors associated with Hurricane Helene (2006) to resolution and diabatic processes is investigated. Furthermore, the dynamics of their growth are analyzed. The SVs are calculated using the tangent linear and adjoint model of the integrated forecasting system of the European Centre for Medium-Range Weather Forecasts with a spatial resolution up to TL255 ($\approx$ 80 km) and 48 hours optimization time. The TL255 moist (diabatic) singular vectors possess a three-dimensional spiral structure with significant upshear tilt within the tropical cyclone in both the horizontal and vertical direction. Also, their amplitude is larger than that of dry and lower resolution singular vectors closer to the center of Helene. Both higher resolution and diabatic processes result in stronger growth being associated with the tropical cyclone compared to other flow features. The growth of the singular vectors in the vicinity of Helene is associated with baroclinic and barotropic mechanisms. The combined effect of higher resolution and diabatic processes leads to significant differences of the singular vector structure and growth dynamics within the core and in the vicinity of the tropical

cyclone. The high resolution singular vectors reveal that baroclinic growth within the tropical cyclone core region has a strong impact on the predictability of tropical cyclones. If used to initialize ensemble forecasts with the integrated forecasting system, the higher resolution moist singular vectors cause larger spread of the wind speed, track and intensity of Helene than their lower resolution or dry counterparts. They impact the outflow of the tropical cyclone more strongly, resulting in a larger downstream impact during recurvature. High resolution singular vectors are able to identify tropical cyclones as one of the most uncertain systems in the tropics emphasizing their impact on the predictability of the atmosphere. Increasing the resolution or including diabatic effects degrades the linearity of the singular vectors. While the impact of diabatic effects on the linearity is small at low resolution, it becomes large at high resolution.

In the second part of this study, the impact of the different perturbation methods on the ensemble spread during tropical cyclone events is compared. Furthermore, the time evolution of the spatial perturbation structure is investigated. The structure of the perturbations due to the different methods is quite different initially. However, our results show that they converge toward a tropical cyclone displacement and intensity-change pattern during the first two days of the forecast on average. The perturbations generated by the stochastic tendency perturbation methods grow rapidly and effectively excite growing modes of the flow. After 48 hours, a large part of the total energy of the singular vector perturbations in the vicinity of the tropical cyclones can be explained by the perturbations of the other methods. In the case of a tropical cyclone, the perturbations by the ensemble of data assimilations dominate the ensemble spread for a rather short lead time (around 24 hours). In about 40% of the cases, the perturbations due to the tendency perturbation schemes or the perturbations generated from singular vectors produce a larger tropical cyclone track and central pressure spread than the perturbations by the ensemble of data assimilations, after two days forecast time. If all methods are applied, the average tropical cyclone track spread of the ensemble matches the average error of the ensemble-mean quite well. In addition, the ensemble captures the anisotropy in the position uncertainty of the tropical cyclones.

Contents

1 Introduction **1**

2 Theoretical Background **5**

2.1 Tropical Cyclones 5
2.2 Singular Vectors 7
2.2.1 Mathematical Formalism 8
2.2.2 Growth Mechanisms 9
2.2.3 Sensitivity of Calculations 12
2.3 Numerical Weather Forecasting at ECMWF 13
2.3.1 The Ensemble Prediction System 16
2.4 Perturbation Methods for Ensemble Forecasting 17
2.4.1 Singular Vectors 17
2.4.2 Ensemble of data assimilations 18
2.4.3 Stochastic kinetic energy backscatter scheme 19
2.4.4 Stochastic perturbations of parameterized tendencies 20
2.4.5 Impact on Tropical Cyclone forecasts 21
2.5 Energy Flow Analysis 22
2.6 Potential Vorticity 24
2.7 Linearity Indices 24

3 Singular Vectors Associated with Tropical Cyclones **27**

3.1 Experiments 27
3.1.1 Singular Vector Experiments 27
3.1.2 EPS Experiments 28
3.2 Observed Evolution of Helene 29
3.3 Sensitivity of Singular Vectors 30
3.4 Growth Mechanisms 36
3.5 Potential Impact on the EPS 47
3.6 Quantification of Nonlinearities 51
3.7 Further Cases 55

3.8 Downstream Impact 57
3.9 Summary 61

4 Impact of different perturbation methods used in the ECMWF ensemble prediction system on tropical cyclone forecasts 63
4.1 Experiments 64
4.2 Perturbation growth and structure 65
4.2.1 Mean growth of perturbations 67
4.2.2 Projection of SVINI perturbations 68
4.2.3 Composite Structure 69
4.3 Impact on ensemble forecasts 79
4.4 Summary 87

5 Summary 91

References 97

1 Introduction

Tropical cyclones (TCs) are one of the strongest forces of nature. They pose a considerable threat to both human lives and property. To mitigate the impact of such a threat, for example to initiate an evacuation, society needs reliable TC track and intensity forecasts. However, these forecasts still have large uncertainties regarding the TC track, structure and intensity. The uncertainties arise from both uncertainty of the initial conditions and errors of the forecast model. Ensemble forecasts are used to quantify the uncertainties associated with a single forecast. For an ensemble forecast, in addition to the single control forecast a number of additional forecasts are performed, the so called perturbed forecasts or ensemble members. For the perturbed forecasts, the initial conditions of the model and the model tendencies are perturbed. If the ensemble forecast properly represents the uncertainties of the particular single forecast, the ensemble forecast can be used to determine how trustworthy the single forecast is. Furthermore, it is possible to distinguish between different outcome scenarios and to assign probabilities to the different scenarios.

As an example Figure 1.1 shows the different tracks within a ten day ensemble forecast of Hurricane Ike (2008). It is clear that the location of Ike's landfall is still uncertain at this time, since the tracks of the TC within the different forecasts diverge strongly. This is important information for decision makers who need to coordinate the emergency-response.

Different techniques are used to generate perturbations for the ensemble members within the ensemble prediction system (EPS) of the European Centre for Medium-Range Weather Forecasts (ECMWF). In general, one can distinguish between two classes of perturbation methods. One class of perturbation methods accounts for the fact that the atmospheric state from which the forecast is started is imperfectly known, the so called initial condition uncertainty. The other class aims to cover uncertainties associated with imperfections of the forecast model, so called model error.

One of the techniques in the ECMWF EPS that aims to represent initial condition uncertainty is the singular vector (SV) approach. The SV formalism identifies

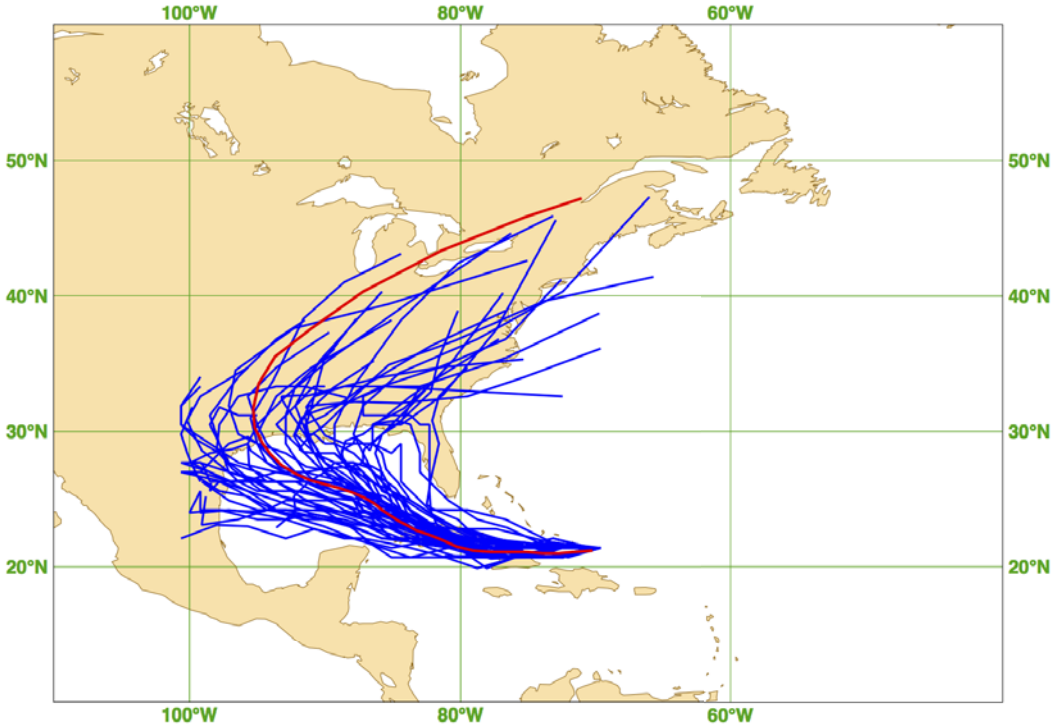

Figure 1.1: Tracks (perturbed forecasts in blue and control forecast in red) of Hurricane Ike (2008) from EPS forecast initialized on 09 September 2008 00 UTC.

the perturbations to a given forecast that produce the strongest growth in a linear framework (Buizza and Palmer, 1995). The rationale behind using SVs as perturbations to the initial conditions is to sample the dynamically most relevant structures that will dominate the uncertainty some time in the future (Ehrendorfer and Tribbia 1997, Leutbecher and Palmer 2008). A further area where SV techniques are applied is for targeted observations (Palmer et al. 1998, Leutbecher 2003). It is assumed that the SVs identify the region where errors in the analysis matter most. Then, to reduce these errors, extra observations are deployed within these regions. Since the SV formalism correspond to a generalized stability analysis of the flow (Farrell and Ioannou, 1996a) the SVs can provide important information about the processes that dominate the predictability of weather systems such as TCs. Identifying and understanding these processes is an important step in improving the forecast models and observation networks for TC forecasting.

Calculating SVs is costly in terms of computing time and, therefore, they are calculated operationally at lower spatial resolution than the actual forecasts (Leutbecher and Palmer, 2008). As a consequence, weather systems like TCs might not be well represented in the computations. For example, the operational spatial reso-

lution for the SV computations at ECMWF is approximately 320 km, far to coarse to represent a TC properly. So far it is not understood how the reduced resolution impacts the performance of the SVs for predicting perturbation growth and identifying the relevant processes in case of a TC event. This issue is assessed in the first part of this study. Here, we investigate the properties of SVs associated with TCs. We assess their sensitivity to resolution and diabatic processes and study the mechanisms that lead to their growth. Furthermore we quantify the potential impact of high resolution SVs on TC ensemble forecasts.

Recently, the configuration of the ECMWF EPS was altered significantly. New perturbation methods have been introduced into the EPS in addition to the SV method. Singular vectors and an ensemble of data assimilations are used to generate perturbations to the initial conditions, while two stochastic tendency perturbation schemes account for model error (see Sect. 2.4 for a descriptions of the different methods). In contrast to the SV perturbation method which is purely dynamically motivated, the other methods try to account for the actual uncertainty associated with a forecast.

It is important to quantify the impact of the different methods on TC forecasts both for ensemble design as well as for studies that use the ensemble to explore the dynamics of TCs. It is important to assess whether the different methods generate growing perturbations that increase the ensemble spread and what mechanisms they exploit for their growth, whether the perturbation patterns vary between the perturbation methods, and how much of the ensemble variance can be assigned to each method in case of a TC event. The second part of the study focuses on the properties of the new methods used in the EPS to generate perturbations in case of TCs. We analyse the spatial structure of the perturbations generated by the different methods and how they change over time. Furthermore, we quantify the impact of the different methods on the spread of TC forecasts and link their growth to the growing modes, as identified by the SVs, of the flow.

The results of our investigations are of high relevance for the design of future versions of TC ensemble prediction systems. One of the challenges in designing these systems will be to decide what methods should be used to generate the ensemble perturbations and how much variance should be introduced into the system by each method. Therefore, detailed knowledge is needed of the properties, dynamics and impact of the perturbations generated by the different methods.

The thesis is organised as follows. In Chapter 2, we describe the theoretical background needed for our studies. We investigate the sensitivity and dynamics

of SVs associated with TCs in chapter 3 and assess the impact of the different perturbation methods used in the operational EPS on TC forecasts in chapter 4. In chapter 5 we give concluding remarks.

2 Theoretical Background

In this chapter we present the theoretical background for the analysis methods we use and the state of knowledge relevant for our study. First the properties of TCs are described (Sect. 2.1). In Section 2.2 we introduce SVs, give details about the mathematical formalism and describe their growth dynamics. We give an overview of numerical weather prediction at ECMWF with focus on the EPS in Section 2.3 and introduce the different perturbation methods used at ECMWF for ensemble forecasting in Section 2.4. The energy flow analysis used to diagnose the growth mechanisms of the SVs is described in Section 2.5. Finally, we introduce Potential Vorticity in Section 2.6 and in Section 2.7 we describe the indices we use to quantify the impact of nonlinearities associated with the nonlinear growth of the SV perturbations.

2.1 Tropical Cyclones

Tropical cyclones are some of the most intense weather phenomenons, causing loss of lives and substantial economic losses every year. Aim of this Section is to give a brief overview over TCs. A detailed review of the properties and dynamics of TCs can be found in Emanuel (2003) and Chan and Kepert (2010).

A TC is defined as a cyclone that develops over the tropical oceans from which it obtains its energy by heat transfer (Emanuel, 2003). The maximum of the 10 m time-averaged winds are used for categorizing observed TCs (Emanuel, 2003). A 10-minute period (1 minute in the United States) is used for the time averaging. Tropical cyclones with windspeeds below or equal to 17 $m\ s^{-1}$ are called tropical depressions, while TCs with windspeeds in the range of 18 to 32 $m\ s^{-1}$ are called tropical storms. If the maximum winds of the TC equal 33 $m\ s^{-1}$ or even exceed this value, it is called a Hurricane in the North Atlantic and eastern North Pacific region, a typhoon in the western North Pacific and a severe TC anywhere else (Emanuel, 2003). In general a sea surface temperature above 26° C is needed for TCs to develop. Tropical cyclones usually form at latitudes greater than 5° North or South,

thus the Coriolis force is important for TC genesis. They normally form during the summer and early autumn.

The energetics of a mature Hurricane can be approximated as an ideal Carnot engine (Emanuel, 2003). Heat is taken from the ocean by evaporation and released by radiative cooling to space at the top of the TC. This potential energy conversion is performed by the transverse secondary circulation, which is overlaid by the strong primary azimuthal circulation. Because of this conversion the TC can maintain its kinetic energy in the presence of boundary layer dissipation (Chan and Kepert, 2010). The maximum upward motion within a TC is located within the eyewall that consist of a ring of deep convective clouds around the inner core of the TC (Emanuel, 2003). In the eye itself the air slowly subsides and as a result the eye is cloud free.

A TC can be characterized as an predominantly axisymmetric vortex. The TC circulation is dominated by cyclonic winds over most of the depth of the troposphere. While it is calm within the TC center, the maximum winds are to be found at approximately a radius of 10 - 100 km, usually within the eyewall region. Beyond this radius the wind speed decreases again. The azimuthal velocity in a TC is approximately in gradient wind balance and on the scale of a Hurricane, the hydrostatic balance still holds (Holton, 2004). This implies that the vertical shear of the azimuthal velocity is controlled by the radial temperature gradient. Winds are strongest near the surface and decay with height because TCs possess a warm core, especially at higher altitudes. That is, the temperature within the TC core is higher that the temperature of its environment at the same height (Emanuel, 2003). Near the top of the TC the cyclonic direction of the wind is reversed and the air flows anticyclonically out of the storm, in the so called outflow. The ouflow is often concentrated in outflow jets (outflow channels) and thus often asymmetric (Emanuel, 2003). The outflow of a TC possesses a clearly larger scale, of up to 3000 km, than the cyclonic vortex and is comparable to the synoptic scale of extratropical weather systems (Merrill, 1988).

To a first order approximation TCs move with the background wind of the environmental flow, the so called steering flow (Emanuel, 2003). However, studies with barotropic models and idealized TC like vortices have shown that the planetary vorticity gradient can impact the TC track (Fiorino and Elsberry, 1989). By acting on the vorticity distribution of its environment the TC induces asymmetries, so called beta-gyres. The large scale flow between the gyres then advects the vortex causing a track deflection. Tropical cyclones are baroclinic vortices (Emanuel, 2003) and environmental shear can have complex effects on the motion of a TC (Wu and Emanuel,

1993, Jones, 2000). The movement of the TC with the environmental flow leads to asymmetries in the ground relative windfield. These asymmetries can be approximated as the vector product of the TC relative wind velocities and the translation velocity (Emanuel, 2003).

Within the tropics and subtropics the environment of the TC is dominated by the subtropical high. If the TC moves further towards the midlatitudes extratropical systems, like midlatitude troughs, become increasingly important for the TC motion. These systems can steer the TC into the midlatitude flow which can result in the TC recurving and undergoing extratropical transition (ET). If the TC moves into the midlatitude flow it faces changes in its environment, such as increased baroclinity and vertical shear, meridional humidity gradients, changes in the sea surface temperature (SST) and an increased Coriolis parameter. During the interaction of the TC with the midlatitude environment it undergoes extensive structural changes. It develops strong asymmetries, becomes broader, develops frontal structures and eventually transforms into a midlatitude system (Jones et al., 2003). Furthermore, during ET the TC can trigger rossby wave trains that impact regions far downstream of the ET event (Anwender et al., 2008, Harr et al., 2008, Riemer et al., 2008). For example, an ET event can affect Europe by influencing Mediterranean cyclones (Grams et al., 2011).

2.2 Singular Vectors

Following Lord Rayleigh (1880), the classical stability analysis in meteorology searches for exponential growing normal modes of the relevant linearized equations. For such an analysis, a constant (time independent) background state is specified. Then the assumption is made that for $t \rightarrow \infty$ the strongest growing normal modes dominate the perturbation growth. However, Orr (1907) pointed out that for certain fluid dynamics problems, perturbations can exhibit transient growth within finite time intervals. This is the case for perturbations that possess a tilt against the shear of the background state. The so called transient growth can exceed the growth of the leading normal modes of the system (Farrell, 1982). It is caused by the interaction of non-orthogonal modes (Farrell and Ioannou, 1996a). Transient growth can be observed also if the system under investigation possesses only damped normal modes (Farrell and Ioannou, 1996a). The SV formalism (Sect. 2.2.1) opens up the possibility of performing a generalized stability analysis and investigating the finite time

stability of systems (Buizza, 1994). Furthermore it makes it possible to examine systems with a time dependent background state for which the classical normal mode approach fails. This is the case for a time dependent background state for which it is not possible do define normal modes (Farrell and Ioannou, 1996b). Here the perturbations converge towards the leading Lyapunov vector of the flow for $t \to \infty$.

2.2.1 Mathematical Formalism

The SVs (also called optimal perturbations) identify the fastest-growing perturbations to a given trajectory (e.g. a weather forecast) within a finite time interval (the optimization interval) in a linear framework (Lorenz, 1965, Buizza, 1994, Palmer et al., 1998). Following Buizza (1994) we consider a discretised nonlinear dynamical system

$$\frac{d\mathbf{x}}{dt} = \mathcal{A}[\mathbf{x}] \tag{2.1}$$

with state vector $\mathbf{x}$. In this case the operator $\mathcal{A}$ represent the full nonlinear ECMWF forecast model. After linearisation the equation

$$\frac{d\mathbf{x}'}{dt} = \mathbf{A_l}\mathbf{x}' \tag{2.2}$$

results. Here $\mathbf{x}'$ represents a perturbation of the state vector and $\mathbf{A_l} = \frac{d\mathcal{A}}{d\mathbf{x}}|_{\mathbf{x}(t)}$ denotes the Jacobian matrix of (2.1) evaluated on the nonlinear trajectory $x(t)$ that is a solution of (2.1). Solutions of (2.2) describe the perturbation dynamics of (2.1) as long as the initial perturbation is sufficiently small and the examined time interval is short enough. Equation (2.2) defines the tangent linear model. The integral form of equation (2.2) is

$$\mathbf{x}'(t) = \mathbf{M}\mathbf{x}'(t_0) \tag{2.3}$$

with the forward tangent propagator $\mathbf{M}$ that maps small perturbations along the trajectory from initial time t_0 to the final time t. Thus $\mathbf{M}$ depends on the initial and final time. The SVs are the perturbations that maximize the quotient (in the following we set $\mathbf{x}' = \mathbf{x}'(t_0)$)

$$\sigma^2 = \frac{\langle \mathbf{PMx}', \mathbf{EPMx}' \rangle}{\langle \mathbf{x}', \mathbf{Ex}' \rangle} \tag{2.4}$$

where $\langle \cdot, \cdot \rangle$ represents a Euclidean inner product. Here $\mathbf{P}$ denotes a local projection operator (Buizza, 1994) and $\mathbf{E}$ is the metric used to measure perturbation growth.

At ECMWF the metric used is dry total energy and is defined as follows (Leutbecher and Palmer, 2008):

$$\mathbf{x}'^T \mathbf{E} \mathbf{x}' = \frac{1}{2} \int_{p_0}^{p_1} \int_S (u'^2 + v'^2 + \frac{c_p}{T_r} T'^2) dp\, ds + \frac{1}{2} R_d T_r p_r \int_S (\ln(p_{sfc})')^2 ds \qquad (2.5)$$

where u' and v' refer to perturbations of the wind components, T' denotes the perturbation of the temperature and $ln(p_{sfc})'$ the perturbation of the logarithm of surface pressure. The gas constant is given by R_d, and c_p denotes the specific heat at constant pressure of dry air, T_r a reference Temperature (300 K), p_r a reference pressure (800 hPa) and S the surface of the earth. By employing a local projection operator $\mathbf{P}$ (Buizza, 1994) it is possible to compute SVs targeted on a specific weather system such as a TC. The local projection operator sets a vector to zero outside a specific geographical domain and above (or below) a certain vertical level.

The first SV $\mathbf{x}'_1$ maximizes the ratio in equation (2.4), the second SV $\mathbf{x}'_2$ maximizes this ratio under the constraint of being orthogonal to the first SV, the third SV $\mathbf{x}'_3$ maximizes this ratio under the constraint of being orthogonal to the first and second SV, and so on (Peng and Reynolds, 2006). The initial SVs $\mathbf{x}'_i$ define an $\mathbf{E}$-orthonormal set of vectors at initial time, while the linearly evolved SVs $\mathbf{M}\mathbf{x}'_i$ form an $\mathbf{E}$-orthogonal set at optimization time in the domain defined in $\mathbf{P}$. The growth of the initial SVs is given by their respective singular value σ_i. The SVs fulfill the generalized eigenvector equation (Barkmeijer et al., 2001)

$$\mathbf{M^T P^T E P M x'} = \lambda^2 \mathbf{E x'} \qquad (2.6)$$

with the adjoint propagator $\mathbf{M}^T$. It is possible to reduce the generalized eigenvalue problem to an ordinary eigenvalue problem by multiplying both sides of equation (2.6) with the inverse of the square root of $\mathbf{E}$. Then it is possible to calculate the SVs numerically by an iterative approach, using the forward tangent and adjoint model of the nonlinear forecast model (Buizza et al., 1993).

2.2.2 Growth Mechanisms

Singular vectors for the atmosphere often show upshear titled structures that are untilted within the optimization interval (Buizza and Palmer, 1995, Hoskins et al.,

2000). The SVs tend to be located within regions of high Eady index values. The Eady index is defined as (Hoskins and Valdes, 1990):

$$\sigma_E = 0.31\frac{f}{N}\Lambda \tag{2.7}$$

Here f denotes the Coriolis parameter, $N^2 = g\dfrac{d\ \ln\theta}{dz}$ the Brunt-Väisälä frequency, θ the potential temperature and $\Lambda = \dfrac{d|\mathbf{v}|}{dz}$ the vertical wind shear. The Eady index is the growth rate of the strongest growing normal mode of the Eady model for baroclinic instability (Eady, 1949) and therefore it is a measure for baroclinic growth (Buizza and Palmer, 1995).

Buizza and Palmer (1995) link the growth of SVs to the evolution of a Rossby-wave packet in a baroclinic atmosphere. In Zeng (1983) the author shows that the energy of a Rossby-wave packet grows over time if it possesses a tilt against the shear of the flow. Because of the upshear tilt it is able to extract energy from the basic current. The basic current is weakened while the tilt of the wave packet is reduced and the wave packet moves into the jet region. If the wave packet possesses a down shear tilt, the Rossby-wave packet releases energy and decays. In this case the tilt increases (see also Pedlosky, 1987). For barotropic growth in a westerly jet (Fig. 2.1a), the phase lines of the wave packet need to tilt westward to the south of the jet and eastward to the north of the jet (Fig. 2.1b). This results in a downgradient horizontal momentum flux $\overline{u'v'}$ that weaks the jet. For baroclinic growth the phase lines of the wave packet need to tilt to the westward with height below and eastward with height above the jet (Fig. 2.1c). This configuration results in a downgradient momentum flux also that again weakens the jet.

Previous studies showed that if the SVs are optimized for longer time intervals, they exhibit a rapid initial growth phase followed by slower more modal growth (Badger and Hoskins, 2000, Hoskins et al., 2000). In a 2D linear quasigeostrophic model with an Eady-like background state, transient as well as modal perturbation growth is proportional to the static stability N and vertical shear Λ (Badger and Hoskins, 2000). While the unshielding processes and the Orr mechanism dominate at the initial time, the leading normal mode and thus the baroclinic instability dominates the perturbation growth on long time scales. The authors emphasize the importance of a rich vertical PV structure for rapid growth.

The presence of latent heating can enhance perturbation growth. This is shown by the idealized study of Tippett (1999) in an Eady model framework and for SVs

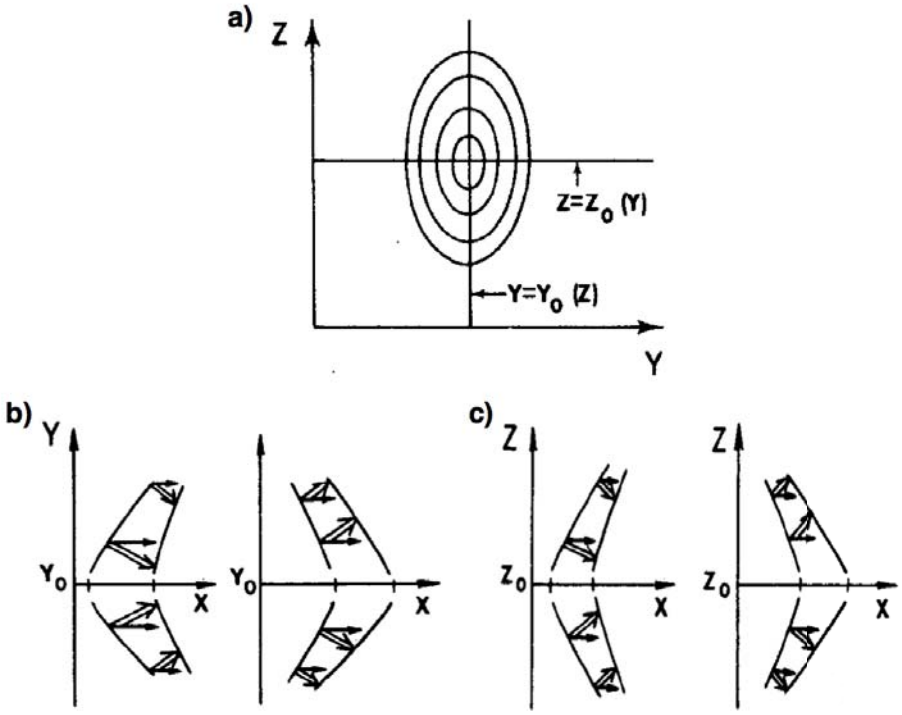

Figure 2.1: Profile (isotachs) of an idealized westerly jet and time development of the tilt of a Rossby-wave packet for a) barotropic and b) baroclinic growth. Both for a a growing (left) and a decaying (right) disturbance. The group velocity is indicated by the double arrows. The solid lines show the phase lines of the wave packet of two consecutive times (from Zeng, 1983).

for a primitive equation model by Coutinho et al. (2004). This is the case since the effective static stability N is reduced in saturated moist flow (Bennetts and Hoskins, 1979). As a consequence, baroclinic growth is enhanced. The reduction of the static stability is caused by the fact that condensation and latent heat release occurs in a saturated atmosphere, if an air parcel is displaced upwards (Durran and Klemp, 1982). In part this heating compensates for the cooling effect of the adiabatic expansion of the air parcel. As a result the density difference between the air parcel and its environment is less than if the air parcel was lifted dry adiabatic. Hence the buoyancy restoring force is decreased (Durran and Klemp, 1982).

Recently, various studies investigated the dynamics of SVs associated with TCs (Peng and Reynolds 2006; Kim and Jung 2009b; Chen et al. 2009). Peng and Reynolds (2006) linked their growth to barotropic instability in the TC outer region, 500 to 700 km away from the storm center. Yamaguchi and Majumdar (2010) investigated the growth of the initial condition perturbations of different ensemble prediction systems with respect to a TC. They found that the perturbations of the ECMWF EPS grow because of barotropic and baroclinic energy conversions in a vortex and baroclinic energy conversion in midlatitude waves. In this study the maxima of the total energy of the SVs are located 500 to 700 km away from the TC center also.

2.2.3 Sensitivity of Calculations

SV calculations are carried out usually at relatively low resolution (T42 - $\approx$ 320 km for the operational EPS) and therefore the forecast used to calculate the SVs are not able to resolve smaller scale systems like a TC. This is the case since at low resolution the the strong gradients associated with such an intense system can not be represented properly.

The sensitivity of extratropical SVs to physical processes has been investigated by Coutinho et al. (2004). They found that so called moist (diabatic) SVs show enhanced growth due to the reduced stability (see Sect. 2.2.2), and that higher resolution is more appropriate for moist SVs. However, they only increased the resolution of the SV calculations up to T63 ($\approx$ 210 km). Ancell and Mass (2006, 2008) tested the impact of spatial resolution and the representation of physical processes on adjoint sensitivities (Errico, 1997) with a regional model. They found large impacts and speculated that the same should be true for SVs since the two techniques are related.

In the case of TCs, moist processes are especially important and the inclusion of diabatic effects in the tangent-linear model has a significant effect on the SVs (Barkmeijer et al. 2001, Puri et al. 2001). Komori and Kadowaki (2010) investigated the effect of spatial resolution (up to TL159, $\approx$ 125 km) on dry SVs targeted on Typhoon Sinlaku for a single forecast. In this study higher resolution resulted in more of the SV structures being associated with the TC than with midlatitue systems. Kim and Jung 2009a assessed the impact of moist effects on the growth of SV associated with a TC in a local area model with a resolution of 100 km and for a single initialization date. The inclusion of moist effects brought the maximum of the vertically integrated total energy closer to the center of the TC, around 300 km. Although these study indicate that SV computations are sensitive to resolution and diabatic effects in case of TCs, a more systematical analysis of the sensitivities is needed to estimate how robust these effects are and to investigate the interaction between moist effects and higher resolution.

2.3 Numerical Weather Forecasting at ECMWF

At ECMWF the "Integrated Forecast System" (IFS) is used to generate numerical weather forecasts. Components of the IFS include the global atmospheric model, the ensemble prediciton system (EPS) and the data assimilation suite (IFS Documentation, 2010).

The first step in producing a numerical weather forecast is the data assimilation. During this analysis procedure the observations are combined statistically with a short range forecast resulting in the analysis which serves as the initial conditions for the model integrations (Kalnay, 2003). At ECMWF a four dimensional variation data assimilation system (4DVAR) is used (Courtier et al., 1994).

For a weather forecast with the ECMWF global forecast model a set of partial differential equations is solved numerically. A spectral method based on a spherical harmonic representation is used to compute the horizontal derivatives (Persson, 2005). In the vertical the atmosphere is divided into layers. For the vertical representation a hybrid coordinate η is used which is a function of pressure p and also depends on the surface pressure p_s (IFS Documentation, 2010):

$$\eta(0, p_s) = 0 \quad \text{and} \quad \eta(ps, ps) = 1 \tag{2.8}$$

In the lowermost troposphere the η-levels (model levels) follow the orography while

in the upper troposphere and above the η-levels correspond to surfaces of constant pressure. For the time integration a semi-Lagrangian scheme is used (Persson, 2005).

The equations that are solved are as follows (from IFS Documentation, 2010). The horizontal momentum equations are given by:

$$\frac{\partial U}{\partial t} + \frac{1}{a\cos^2\phi}\left\{U\frac{\partial U}{\partial \lambda} + V\cos\phi\frac{\partial U}{\partial \phi}\right\} + \dot{\eta}\frac{\partial U}{\partial \eta} - fV + \frac{1}{a}\left\{\frac{\partial \Phi}{\partial \lambda} + R_{dry}T_V\frac{\partial}{\partial \lambda}(\ln p)\right\} = P_U + K_U \tag{2.9}$$

and

$$\frac{\partial V}{\partial t} + \frac{1}{a\cos^2\phi}\left\{U\frac{\partial V}{\partial \lambda} + V\cos\phi\frac{\partial V}{\partial \phi} + \sin\phi(U^2+V^2)\right\} + \dot{\eta}\frac{\partial V}{\partial \eta} + fU + \frac{\cos\phi}{a}\left\{\frac{\partial \Phi}{\partial \phi} + R_{dry}T_V\frac{\partial}{\partial \phi}(\ln p)\right\} = P_V + K_V \ , \tag{2.10}$$

with $U = u\cos\phi$, $V = v\cos\phi$ (here u and v denote the components of the horizontal wind in spherical coordinates), ϕ denotes the latitude and λ the longitude. The radius of the earth is given by a, Φ is the geopotential and R_{dry} is the gas constant of dry air. The virtual temperature T_V is defined as:

$$T_V = T[1 + \{(R_{vap}/R_{dry}) - 1\}q] \ , \tag{2.11}$$

with the temperature T, and the specific humidity q. Here R_{vap} is the gas constant for water vapour and P_U and P_V denote the contributions of physical processes that cannot be resolved at the specific model resolution and therefore need to be parametrized. The horizontal diffusion terms are denoted by K_U and K_V. The thermodynamic equation is:

$$\frac{\partial T}{\partial t} + \frac{1}{a\cos^2\phi}\left\{U\frac{\partial T}{\partial \lambda} + V\cos\phi\frac{\partial T}{\partial \phi}\right\} + \dot{\eta}\frac{\partial T}{\partial \eta} - \frac{\kappa T_V\omega}{(1+(\delta-1)q)p} = P_T + K_T \ , \tag{2.12}$$

with $\kappa = R_{dry}/c_{Pdry}$ and $\delta = c_{Pvap}/c_{Pdry}$. Here c_{Pdry} denotes the specific heat of dry air at constant pressure and c_{Pvap} the specific heat of water vapour at constant pressure. The vertical velocity in pressure coordinates is given by $\omega = dp/dt$. Again, P_T

refers to the contributions of parametrized processes while K_T denotes the horizontal diffusion term. The moisture equation is:

$$\frac{\partial q}{\partial t} + \frac{1}{a\cos^2\phi}\left\{U\frac{\partial q}{\partial \lambda} + V\cos\phi\frac{\partial q}{\partial \phi}\right\} + \dot{\eta}\frac{\partial q}{\partial \eta} = P_q + K_q \ , \tag{2.13}$$

with the contributions P_q of parametrized processes and K_q, the horizontal diffusion term. The continuity equation is:

$$\frac{\partial}{\partial t}\left(\frac{\partial p}{\partial \eta}\right) + \nabla\cdot\left(\mathbf{v}_H\frac{\partial p}{\partial \eta}\right) + \frac{\partial}{\partial \eta}\left(\dot{\eta}\frac{\partial p}{\partial \eta}\right) = 0 \ , \tag{2.14}$$

with the horizontal wind $\mathbf{v}_H$ and the horizontal gradient operator in spherical coordinates ∇. The hydrostatic equation used to simplify the vertical momentum equation is given by:

$$\frac{\partial \Phi}{\partial \eta} = -\frac{R_{dry}T_V}{p}\frac{\partial p}{\partial \eta} \ . \tag{2.15}$$

Finally, the equation for the vertical velocity is:

$$\omega = -\int_0^\eta \nabla\cdot\left(\mathbf{v}_H\frac{\partial p}{\partial \eta}\right)d\eta + \mathbf{v}_H\cdot\nabla p \ , \tag{2.16}$$

and the surface pressure tendency is defined as:

$$\frac{\partial p_s}{\partial t} = -\int_0^1 \nabla\cdot\left(\mathbf{v}_H\frac{\partial p}{\partial \eta}\right)d\eta \ . \tag{2.17}$$

The equations (2.16) and (2.17) result from integrating the continuity equation (2.14).

Parametrisation schemes are used to account for physical processes that cannot be resolved by the model at a given resolution (IFS Documentation, 2010). These schemes define the impact of cloud processes and large scale condensation, moist convection, subgrid-scale orographic effects, longwave and shortwave radiation, boundary layer processes, processes associated with the surface, ocean waves and stratospheric processes. The effects of these processes are calculated using a gridpoint representation of the model fields, a so called reduced Gaussian grid (Persson, 2005).

2.3.1 The Ensemble Prediction System

An ensemble forecast at ECMWF consist of 51 forecasts (ensemble members) - one control forecast and 50 perturbed forecasts (Leutbecher and Palmer, 2008). The ensemble forecasts are performed at a horizontal resolution of TL639 ($\approx$ 32km) and with 62 vertical levels (Miller et al., 2010).

For the perturbed forecasts, perturbations are added to the initial conditions and stochastic tendency perturbation methods are used to represent model errors (Leutbecher and Palmer, 2008). This procedure is depicted schematically in Figure 2.2. The initial (control) analysis in the state space of the model is represented by the red dot, while the black dots represent the perturbed analyses. These are generated by adding perturbations to the control analysis to account for the analysis uncertainty (depicted by the blue circle on the left). This uncertainty is then propagated in time by the forecast model. To represent model error, the stochastic tendency perturbation schemes operate as a continuous forcing. Perturbations are injected into the flow over the whole integration time of the model.

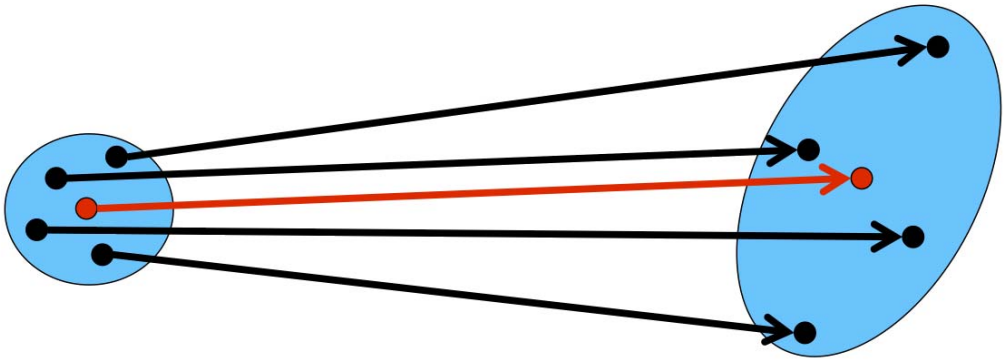

Figure 2.2: Schematic diagram of an ensemble forecast. The control forecast is depicted in red, the perturbed forecasts are black. The blue circles represent the uncertainty of the initial analysis and the forecast (for further explanations see text).

In the operational setup of the EPS, four different methods are applied to generate perturbations for the ensemble (Palmer et al., 2009). Each ensemble member is perturbed by all four methods. To account for the analysis uncertainty, perturbations generated from SVs and perturbations generated from an ensemble of data assimilations are used. Two stochastic tendency perturbation schemes, the kinetic energy backscatter scheme and the stochastically perturbed parametrisation tenden-

cies scheme aim to mimic the effects of errors in the model formulation. The different methods are described in Section 2.4.

2.4 Perturbation Methods for Ensemble Forecasting

2.4.1 Singular Vectors

The resolution of the operational SV calculations for the EPS is T42 ($\approx$ 320 km) with an optimization time of 48 hours. Singular vectors are calculated for the extratropics of the Northern and Southern Hemisphere (Fig 2.3). Extra sets of SVs are added for TCs (Puri et al., 2001). The SVs targeted on TCs are calculated with the ECMWF linearized physics package included in the tangent linear and adjoint model (Barkmeijer et al., 2001). Linearized schemes for vertical diffusion, surface drag, sub-grid-scale orographic effects, large scale condensation and deep convection are used in the SV computations (Mahfouf 1999, Tompkins and Janiskova 2004, Lopez and Moreau 2005). The SVs targeted on TCs are optimized below 500 hPa (Puri et al., 2001).

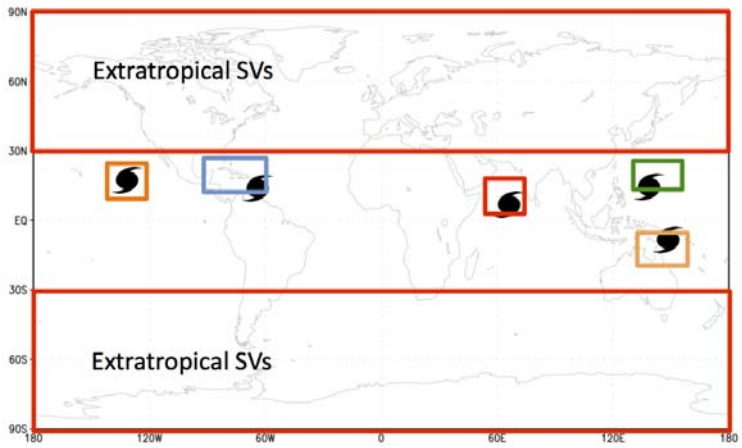

Figure 2.3: Optimization regions (colored boxes) of the SVs for the operational EPS. TC positions are given by the black markers.

As already mentioned, the rationale behind using SVs as perturbations to the initial conditions is to sample the most dynamically relevant structures that will dominate the uncertainty at some time in the future (Ehrendorfer and Tribbia 1997, Leutbecher and Palmer 2008). Therefore, generating ensemble perturbation from SVs is dynamically motivated. The SVs do not account for the actual analysis

uncertainty if computed using a total energy norm (Palmer et al., 1998). To generate the initial condition perturbations from the SVs, each ensemble member is perturbed by a combination of SVs from all SV sets. Until June 2010, evolved extratropical SVs from two days earlier were added to represent analysis uncertainty that developed in the past. In the current operational version, the evolved SVs were replaced by perturbations generated from the ensemble of data assimilations (Buizza et al., 2008, see Sect. 2.4.2). Each SV is scaled with a random number drawn from a Gaussian distribution (see Leutbecher and Palmer (2008) for a in depth description of the generation of the SV based initial perturbations).

The amplitude of the SV perturbations has been reduced substantially in recent years (Martin Leutbecher, personal communication). In November 2007, their amplitude was reduced by 30% after a more active model physics package was implemented (Bechtold et al., 2008). Further reductions of the amplitude by 10% and 50% respectively were made following the implementation of the initial perturbations from the Ensemble of Data Assimilations (EDA) in June 2010 and the revision of the representation of model uncertainty in November 2010. The reductions of the amplitude of the SV perturbations led to an improved reliability of the ensemble variance in the extra-tropics. In these revisions, the perturbations targeted on tropical cyclones have been reduced by the same factor as the extra-tropical perturbations, i.e. they have not been tuned separately. The experiments of the first part of this study (Chapt. 3) use the SV perturbation amplitude that was operational until November 2010, while the experiments of the second part of this study (Chapt. 3) use the SV perturbation amplitude implemented operationally since November 2010.

2.4.2 Ensemble of data assimilations

The ensemble of data assimilations (EDA) is designed to estimate the uncertainty of analyses and short-range forecasts (Isaksen et al., 2010). In June 2010, perturbations generated from the EDA replaced the evolved SVs used in previous EPS configurations (Buizza et al., 2008). Four dimensional variational data assimilation (4D-Var) is used for generating the initial conditions for the forecast model (Courtier et al., 1994). The EDA system consists of one unperturbed control and 10 perturbed 4D-Var analyses, which are run at lower resolution than the deterministic analysis. A spatial resolution of TL399 ($\approx$ 50 km) with 91 vertical levels is used for the outer loop, while two inner loops with a spatial resolution of TL95 ($\approx$ 210 km) and TL159 ($\approx$ 125 km) respectively are used for the minimization (Isaksen et al., 2010). To gen-

erate the perturbed analyses, the observations are perturbed by random numbers drawn from a Gaussian distribution that matches the observation error estimates from the 4D-Var system. In addition, a stochastic tendency perturbation scheme is used to represent model error within the analysis cycle (the scheme is described in Sect. 2.4.4). A detailed description of the generation of the ensemble of analyses can be found in Isaksen et al. (2010).

To generate initial perturbations for the EPS, the difference between two 6-hour forecasts, one started from an unperturbed analysis and one started from the control analysis, is added to one ensemble member (Buizza et al., 2008). The perturbations are centered symmetrically around the high resolution deterministic analysis. Thus the perturbations of the even ensemble members have the opposite sign to the perturbations of the odd ensemble members (Isaksen et al., 2010).

2.4.3 Stochastic kinetic energy backscatter scheme

The stochastic kinetic energy backscatter scheme (SKEB) aims to represent model error associated with the upscale kinetic energy transfer of unresolved subgrid-scale processes (Berner et al., 2009). Part of this error arises since conventional parametrisation schemes do not account for statistical fluctuations in the fluxes between the resolved and unresolved components of the flow. Another source of error is structural deficiencies of parametrisation schemes (Palmer et al., 2009). For example, the kinetic energy generated by buoyancy forces within convective clouds is often not accounted for properly by convective parametrisation schemes (Shutts, 2005). The SKEB scheme computes a stochastic streamfunction forcing that is applied to each model level during the integration of the forecast model, so as a result the rotational component of the wind is perturbed during the forecast time (Palmer et al., 2009). The forcing is modulated by estimates of the three-dimensional kinetic energy dissipation at each grid point.

The streamfunction forcing is generated as follows (Palmer et al., 2009):

$$F_\Psi = \left(\frac{b_r D_{tot}}{B_{tot}} \right)^{1/2} F_{\Psi^*} \ , \tag{2.18}$$

here F_{Ψ^*} denotes a three-dimensional random pattern field and $D_{tot}(x, y, z, t)$ is the

total dissipation rate. The pattern evolves in time using AR(1) processes in spectral space (Berner et al., 2009):

$$\Psi'^{m}_{n}(t + \Delta t) = (1 - \alpha)\Psi'^{m}_{n}(t) + g_n\sqrt{\alpha\epsilon(t)} \ . \tag{2.19}$$

Here Ψ'^{m}_{n} denotes the coefficient of the spherical harmonics decomposition of F_{Ψ^*} for zonal wavenumber m and total wavenumber n. The linear autoregressive parameter is $1 - \alpha$, g_n is a wavenumber-dependent noise amplitude and ϵ a Gaussian white-noise process with mean zero. The variance as function of total wavenumber follows a power law that has been estimated from coarse graining studies. The decorrelation time is 7 hours. If F_{Ψ^*} were used directly as a streamfunction forcing, the forcing would correspond to an ensemble-mean energy input rate of B_{tot} (Palmer et al., 2009) which is used as a scaling factor. The parameter b_r denotes the backscatter ratio. The total dissipation rate D_{tot} accounts for the numerical dissipation, gravity / mountain wave drag and deep convection (Berner et al., 2009). The three components are estimated as follows. The numerical dissipation rate D_{num} is given by $D_{num} = \alpha_{num}K|\nabla\zeta|^2$, with the relative vorticity ζ, the bi-harmonic diffusion coefficient K and the factor α_{num} to account for the effects of the semi-Lagrangian interpolation error. The dissipation due to orographic gravity wave drag is estimated from the vector product of the wind vector tendency from the parametrisation scheme with the actual wind. Finally, the dissipation due to convection is proportional to the updraft convective mass flux rate and the updraft detrainment rate. The detailed description of the SKEB can be found in Berner et al. (2009) and Palmer et al. (2009). The scheme was implemented in the operational EPS in November 2010.

2.4.4 Stochastic perturbations of parameterized tendencies

The stochastically perturbed parametrisation tendencies scheme (SPPT3) aims to represent model uncertainty associated with the physics parametrisation schemes. The total tendencies from the model physics are perturbed with multiplicative noise during the forecast time (Palmer et al., 2009). The tendencies for the wind components (u, v), temperature (T) and humidity (q) are perturbed using

$$X_p = (1 + r\mu)X_c \ . \tag{2.20}$$

Here X_c denotes the unperturbed and X_p the perturbed tendency for one of the variables u, v, T and q. In one grid column the perturbed tendencies are generated with the same random number r for all variables. The random number is drawn from a distribution that is close to a Gaussian distribution except for a clipping of the perturbations at +/- 1.8 standard deviations. The clipping avoids excessive perturbation amplitudes that may result in numerical instabilities. To reduce the amplitude of the perturbation close to the surface and in the stratosphere, the factor μ is applied, which ranges between 0 and 1. The evolving random pattern that defines r has three correlation scales (Martin Leutbecher, personal communication). The temporal correlation scales are 6 hours, 3 days and 30 days and the corresponding spatial correlation scales are 500, 1000 and 2000 km respectively. The variance decreases with the correlation scale. The standard deviations for the three components are 0.52, 0.18 and 0.06. A detailed description of an earlier two-scale version of the scheme is presented in Palmer et al. (2009).

2.4.5 Impact on Tropical Cyclone forecasts

Only a few studies have focused on the effect of stochastic physic schemes and methods for generating ensemble perturbations on TC forecasts. Puri et al. (2001) assessed the respective impact of initial condition perturbations and perturbations introduced by an older version of the stochastically perturbed parametrisation tendency scheme (Buizza et al., 1999) in case of a TC event. They found that within the EPS of ECMWF the stochastically perturbed parametrisation tendency scheme strongly influenced the central pressure of the TC but had less influence on the TC track. In contrast, the perturbations to the initial conditions generated by SVs had a larger impact on the TC track. Anwender et al. (2010) investigated the impact of the two different methods with a focus on the extratropical transition of a Typhoon. They found that the SV perturbations influenced the TC intensity more strongly than the stochastically perturbed parametrisation tendency scheme. Reynolds et al. (2011) assessed the impact of a stochastic convection scheme and a kinetic energy backscatter scheme on TC forecasts within the U.S. Navy global atmospheric ensemble prediction system. The authors concluded that the schemes have a large influence on the TC motion and that the backscatter scheme increases the ensemble standard deviation, especially in the tropics, but does not improve the mean TC track error of the ensemble-mean.

2.5 Energy Flow Analysis

To analyse the mechanisms the SVs exploit for their growth, we use an energy flow analysis. Kwon and Frank (2008) derived the energy equations for a moist Hurricane-like vortex. Their analysis describes the energy conversion relative to a time varying axisymmetric background state. For this purpose the trajectory is separated into an azimuthal mean state (centered on the TC) and the deviation from the azimuthal mean. The governing equations are the energy equation for azimuthal mean kinetic energy, azimuthal mean available potential energy, eddy kinetic energy and eddy available potential energy. The authors define a baroclinic energy conversion term, that represents a conversion between mean potential energy ($\overline{A}$) and eddy potential energy:

$$\frac{\partial \bar{A}}{\partial t}_{baroclinic} = -\left(\frac{h}{s}\right)^2 \left(\overline{u_r' \theta_A'} \frac{\partial \overline{\theta_A}}{\partial r} + \overline{\omega' \theta_A'} \frac{\partial \overline{\theta_A}}{\partial p}\right) \tag{2.21}$$

where $h \equiv (R/P)\,(P/P_R)^{\kappa}$ and $\kappa = (R/C_P)$ with the gas constant R and a reference pressure P_R. An overbar denotes an azimuthal mean. The stability parameter is defined by $s^2 \equiv -h\,(\partial\theta_0/\partial p)$. Radius and pressure are denoted by r and p, while u_r' and ω' are the eddy radial and eddy vertical velocity. Here the potential temperature is split into a base state, that depends only on height and deviations therefrom ($\theta(r, \lambda, p, t) = \theta_0(p) + \theta_A(r, \lambda, p, t)$). $\overline{\theta_A}$ is the azimuthal mean potential temperature and θ_A' the eddy potential temperature.

The barotropic energy conversion term represents a conversion between mean kinetic energy ($\overline{K}$) and eddy kinetic energy. It is defined as follows:

$$\frac{\partial \bar{K}}{\partial t}_{barotrop} = -r\overline{u_r' v_a'} \frac{\partial}{\partial r}\left(\frac{\overline{v_a}}{r}\right) - \overline{u_r' \omega'} \frac{\partial \overline{u_r}}{\partial p} - \overline{v_a' \omega'} \frac{\partial \overline{v_a}}{\partial p} - \overline{u_r' u_r'} \frac{\partial \overline{u_r}}{\partial r} - \frac{\overline{u_r}}{r} \overline{v_a' v_a'} \tag{2.22}$$

with the eddy tangential velocity v_a', the azimuthal mean tangential velocity $\overline{v_a}$ and the azimuthal mean radial velocity $\overline{u_r}$.

A growing perturbation extracts energy from the background state. The baroclinic energy conversion term (2.21) consists of a radial and a vertical eddy heat flux with respect to the radial and vertical gradient of the mean temperature field respectively (Kwon and Frank, 2008). A growing perturbation is associated with a downgradient eddy heat flux, while a decaying perturbation is associated with an upgradient eddy heat flux. The barotropic energy conversion term describes the generation of eddy

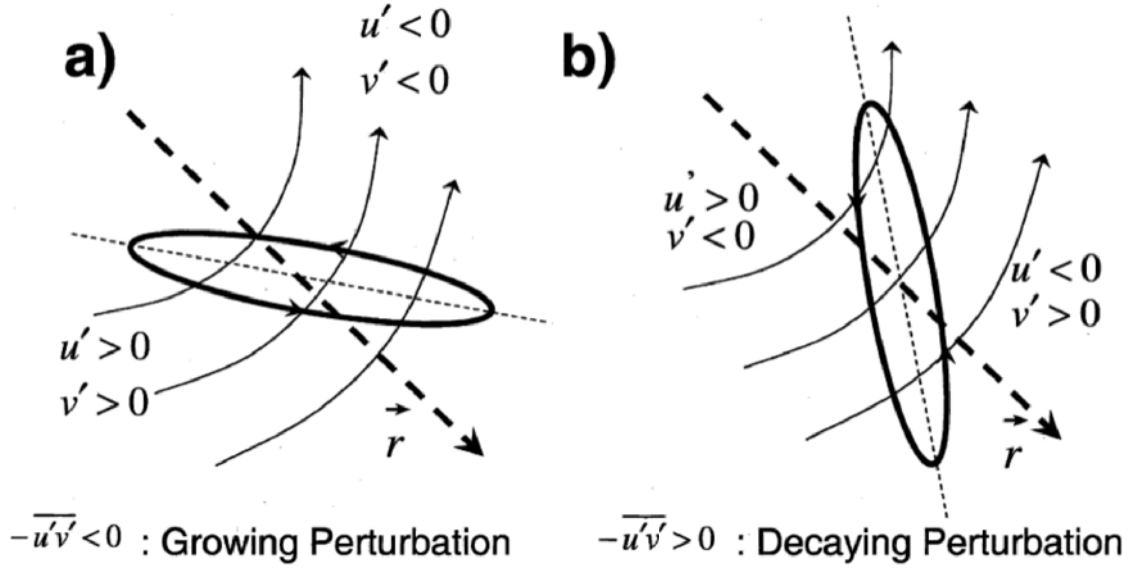

Figure 2.4: Schematics of a barotropically growing (a) and decaying (b) perturbation. The radial gradient of the mean angular velocity is negative. The thin solid lines indicate the tangential winds of the vortex, while the thick solid lines indicate the circulation of the perturbations. The regions of the perturbations that have opposite signs of tangential and radial wind directions are separated by the thin dashed lines. The thick dashed arrows point in the positive radial direction. The growing perturbation tends to reduce the shear of the mean angular velocity by downgradient momentum transfer. In contrast, the decaying perturbation increases the shear by upgradient momentum transfer (from Kwon and Frank (2008)).

kinetic energy by eddy momentum flux in radial direction ($-r\overline{u'_r v'_a}(\partial/\partial r)\,(\overline{v_a}/r)$), the eddy momentum fluxes in vertical direction with respect to the vertical shear of the mean horizontal winds ($-\overline{u'_r\omega'}\partial\overline{u_r}/\partial p$ and $\overline{v'_a\omega'}\partial\overline{v_a}/\partial p$) and the radial convergence of azimuthal mean radial winds ($-\overline{u'_r u'_r}\partial\overline{u_r}/\partial r$ and $-(\overline{u_r}/r)\overline{v'_a v'_a}$) (Kwon and Frank, 2008). An example for a barotropically growing perturbation in case of a hurricane-like vortex is depicted in Figure 2.4 (see also Sect. 2.2.2). A growing perturbation tends to reduce the shear of the mean angular velocity ($\overline{v_a}/r$), while a decaying perturbation increases the shear of the mean angular velocity.

2.6 Potential Vorticity

At several points in our studies potential vorticity is used to diagnose the state of the atmosphere. The potential vorticity is a measure of the ratio of the absolute vorticity to the effective depth of the vortex (see Holton, 2004). It is conserved in a Lagrangian sense for adiabatic, frictionless motion (Hoskins et al., 1985). Under the hydrostatic approximation, the potential vorticity in isobaric coordiantes is defined as (Hoskins et al., 1985)

$$P = -g(f\mathbf{k} + \nabla_p \times \mathbf{v}) \cdot \nabla_p \Theta \tag{2.23}$$

and isentropic coordinates as

$$P = -g(f + \mathbf{k} \cdot \nabla_\Theta \times \mathbf{v})/(\partial p/\partial \Theta)\ , \tag{2.24}$$

with $\nabla_p = (\partial_x, \partial_y, \partial_p)$ and $\nabla_\Theta = (\partial_x, \partial_y, \partial_\Theta)$. PV is usually given in PV units, with 1 PVU $= 10^{-6} m^2 s^{-1} K\ kg^{-1}$. The paper by Hoskins et al. (1985) provides an in-depth review of the concepts of potential vorticity thinking.

2.7 Linearity Indices

If one uses SVs to explore the dynamics of weather systems such as TCs it is important to assess the impact of nonlinearities on the evolution of the SVs in the nonlinear model. If nonlinearities become large the SV formalism might fail to identify the fastest growing modes of the flow. To quantify the impact of nonlinearities associ-

ated with the nonlinear growth of SV perturbations Gilmour et al. (2001) define the relative nonlinearity:

$$\Theta\left(\hat{\delta}, \|\delta\|, t\right) = \frac{\|\delta^+(t) + \delta^-(t)\|}{0.5\{\|\delta^+(t)\| + \|\delta^-(t)\|\}} \tag{2.25}$$

with the unit vector $\hat{\delta}$. Here $\|\cdot\|$ denotes a metric which is defined by an inner product. The difference between an unperturbed forecast and a forecast in which a SV is either added (δ^+) or subtracted (δ^-) from the analysis is denoted by δ. The relative nonlinearity measures relative magnitudes as well as the orientations of the evolved perturbations. Gilmour et al. (2001) note that if the evolution of the positive and negative perturbation is linear then $\Theta = 0$ (since $\delta^+ + \delta^- = 0$), while $\Theta = 0.5$ implies that the error caused by assuming linear evolution will be at least 50% of the average magnitude of the evolved perturbations. The time at which "nonlinearity becomes dominant" is defined by Buizza (1995) as the time when the anticorrelation between the negative and the positive perturbation becomes smaller than 0.7. The anticorrelation is given by

$$l = -\frac{\langle \delta^+(t), \delta^-(t) \rangle}{\|\delta^+(t)\| \|\delta^+(t)\|}. \tag{2.26}$$

If $l = 1$ the perturbations are completely antiparallel. A value of 0.7 equals a deviation by $\sim 45°$ from that state (from the definition of the inner product). In this case assuming linear evolution of the perturbations would result in an error of at least 75% of the mean magnitude of the evolved perturbations. This corresponds to a relative nonlinearity $\Theta > 0.75$ (Gilmour et al., 2001).

3 Singular Vectors Associated with Tropical Cyclones

To assess the utility of the SVs for ensemble construction and for observation targeting, it is important to elucidate the dynamical processes that lead to the growth of the SVs and how these depend on resolution and diabatic processes. In this study, we analyse the characteristics of SVs for Atlantic Hurricane Helene (2006). Analysing the structure of the SVs provides information about the dynamics of perturbation growth in case of a TC event and allows us to identify the relevant growth mechanisms. The content of this chapter has been published in Lang et al. (2011).

We describe the design of our experiments in Section 3.1. In Section 3.2 an overview of the development of Helene is given. In Section 3.3 the sensitivity of the SVs to spatial resolution and physical processes is presented, while in Section 3.4 the mechanisms that lead to the growth of the SVs are investigated. The potential impact on the ECMWF EPS of higher resolution SVs than used in the operational configuration is assessed in Section 3.5 and the justification of the linearity assumption of the SVs is tested in Section 3.6. We test the generality of our sensitivity results by investigating further TC cases in Section 3.7 and analyse the downsteam impact of Helene in Section 3.8. Section 3.9 contains the conclusions derived from this study.

3.1 Experiments

3.1.1 Singular Vector Experiments

Our experiments are designed to investigate the sensitivity of the SVs to spatial resolution and diabatic processes. SV calculations are performed with a horizontal resolution of T42 ($\approx$ 320 km, the operational resolution for SVs in the ECMWF EPS), TL95 ($\approx$ 210 km, typical resolution for SVs for targeted observations at ECMWF), TL159 ($\approx$ 125 km) and TL255 ($\approx$ 80 km), all with 62 vertical levels. We calculate the leading five SVs. At ECMWF a forecast from the full (moist) nonlinear model

with the same resolution as the SVs acts as the trajectory of the SV computations. The optimization time for the calculations is 48 hours. A local projection operator is employed to target the SVs on a specific region (see Section 2.2.1).

The geographic domain over which TC SVs are optimized (the optimization region) is based on the predicted positions of the TC from the previous EPS forecast (van der Grijn et al. 2004, Leutbecher 2007). First, a box is chosen in such a way that it includes all the 48-h forecast positions of the TC in the 50 ensemble members of the operational ensemble (a detailed description of the operation EPS configuration is given in Leutbecher and Palmer 2008). Then the box is extended 7° to the east and west and 5° to the north and south. If the TC cannot be identified in more than 10 ensemble members a $22.5° \times 30°$ box is centered around the reported position of the TC. In addition, we calculated SVs optimized over the global tropical band (30°N to 30°S).

We calculate so called moist (diabatic) and dry SVs. For the moist SVs, the ECMWF linearized physics package is included in the tangent linear and adjoint model (Barkmeijer et al., 2001). Linearized schemes for vertical diffusion, sub-grid-scale orographic effects, large scale condensation, surface drag and deep convection have been used in the moist SV computations (Mahfouf 1999, Tompkins and Janiskova 2004, Lopez and Moreau 2005). In contrast to the moist SVs, the dry SVs are calculated only with the linearized scheme for vertical diffusion and surface drag. The dry total energy norm (Eqn. 2.5) is used to calculate both dry and moist SVs. The SVs are optimized over the depth of the troposphere (from the surface to 200 hPa). For this study, SVs targeted on Hurricane Helene (2006) have been calculated daily from 16 to the 24 September. The initialisation time for the SV calculation was 12 UTC.

3.1.2 EPS Experiments

In addition to the SV calculations, we conducted idealized experiments with 10 ensemble members. These were used to assess the potential impact of the higher resolution SVs on the EPS, to carry out the energy flow analysis and to quantify the nonlinearities. The EPS experiments have a resolution of TL255. Each ensemble member was perturbed with only one of the leading five SVs by either adding or subtracting it from the analysis. For our experiments, all SVs are scaled with the same fixed value, chosen to make their amplitude correspond to estimates of analysis errors (see Leutbecher and Palmer 2008 for a detailed discussion of the scaling

of the SVs for ensemble generation). In our experiments the maximum zonal wind perturbation in 500 hPa ranges between $0.8m\ s^{-1}$ and $1.9m\ s^{-1}$. In the operational EPS configuration, the weighting factors of the SVs are drawn from a Gaussian distribution (Leutbecher and Palmer, 2008) and the ensemble members are perturbed by a linear combination of different sets of SVs (see Sect. 2.4.1). However, we chose a fixed scaling factor to concentrate on the impact of the SV structure on the EPS forecasts and to filter out effects due to variable scaling. Also, in order to investigate the nonlinear growth of the SVs, different scaling factors were tested. In contrast to the operational setup, the EPS forecasts and the SV computations are started from the same analysis. In the operational setup the SV trajectory is initialized from a 6-hour forecast (Leutbecher, 2005).

3.2 Observed Evolution of Helene

Hurricane Helene (2006) was selected for this case study as it exhibited a classical recurvature and ET over the Atlantic, so that the interaction with the midlatitude flow can be considered without taking into account structural modifications during landfall (Fig. 3.1). Helene formed as a tropical depression on 12 September 2006 12 UTC and reached Hurricane strength on 16 September 12 UTC (Brown, 2006). It started to recurve on 21 September and was classified as an extratropical system on 25 September. Thus our experiments cover the period from before recurvature to ET (see Section 3.1).

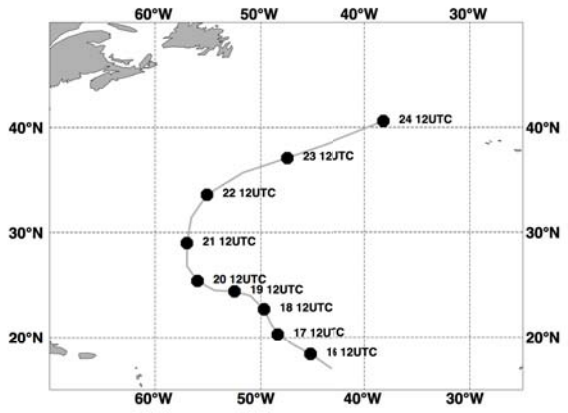

Figure 3.1: Track of Helene (2006) from 16 September 2006 00 UTC to 24 September 2006 12 UTC. Black circles mark Helene's position at 12 UTC - the initialization times for the experiments (from Lang et al., 2011).

Between 17 and 19 September 2006, Helene intensifies and develops a strong asymmetric outflow jet, a so called outflow channel (Fig 3.2a and b). At this time Helene moves northwestwards, while to the northwest Hurricane Gordon (located around 30°N, 60°W) moves into the midlatitudes. On 19 September 12 UTC, Helene continues to move northwestwards and approaches an upper-level positive PV anomaly (Hoskins et al., 1985) that is about to cut off (Fig. 3.2b). This PV anomaly formed during the interaction of Hurricane Gordon with the midlatitude jet. The approaching PV anomaly strengthens the PV gradient between the low PV of Helene's outflow and the surrounding flow (Fig. 3.2b and c). This leads to a further enhancement of Helene's outflow, which then starts to interact with the positive PV anomaly. During this process the PV anomaly thins and elongates markedly. On 21 September 12 UTC the remnants of the PV anomaly are advected around Helene's outflow anticyclone (Fig. 3.2c). An upstream trough located at approximately 40°N, 70°W (Fig. 3.2c) moves towards Helene from the northwest and steers the TC into the midlatitude flow. During this process Helene's outflow interacts with the midlatitude jet, advecting low PV air into the ridge forming downstream of Helene (Fig. 3.2d).

3.3 Sensitivity of Singular Vectors

The structure and location of the initial SVs in the vicinity of Helene changes systematically if the resolution of the SV calculations is increased and diabatic effects are accounted for. Thus different regions of the flow are identified by the SV formalism as being most favorable for perturbation growth. These dependencies are illustrated in Fig. 3.3 using composites of the sum of the vertically integrated total energy of the leading five SVs for all initialisation dates for each category (different resolutions, dry, or moist). The composite fields are centred on the position of the TC on each date[1].

The trajectory for the SV calculations is a forecast of the full nonlinear model with the same resolution as the SV calculations (see Section 3.1.1). Thus there could be differences between the trajectories at different resolutions concerning the strength and position of Helene and other synoptic systems. Comparisons of the structure and the tracks of Helene in the higher and lower resolution trajectories show that there are rather small differences of the position of Helene and surrounding features of the flow (e.g. of the upstream upper-level positive PV anomaly) between higher and

[1]For the composites, the SVs are not weighted with their respective singular value. However, the qualitative structure of the composites is not altered if weighting is applied.

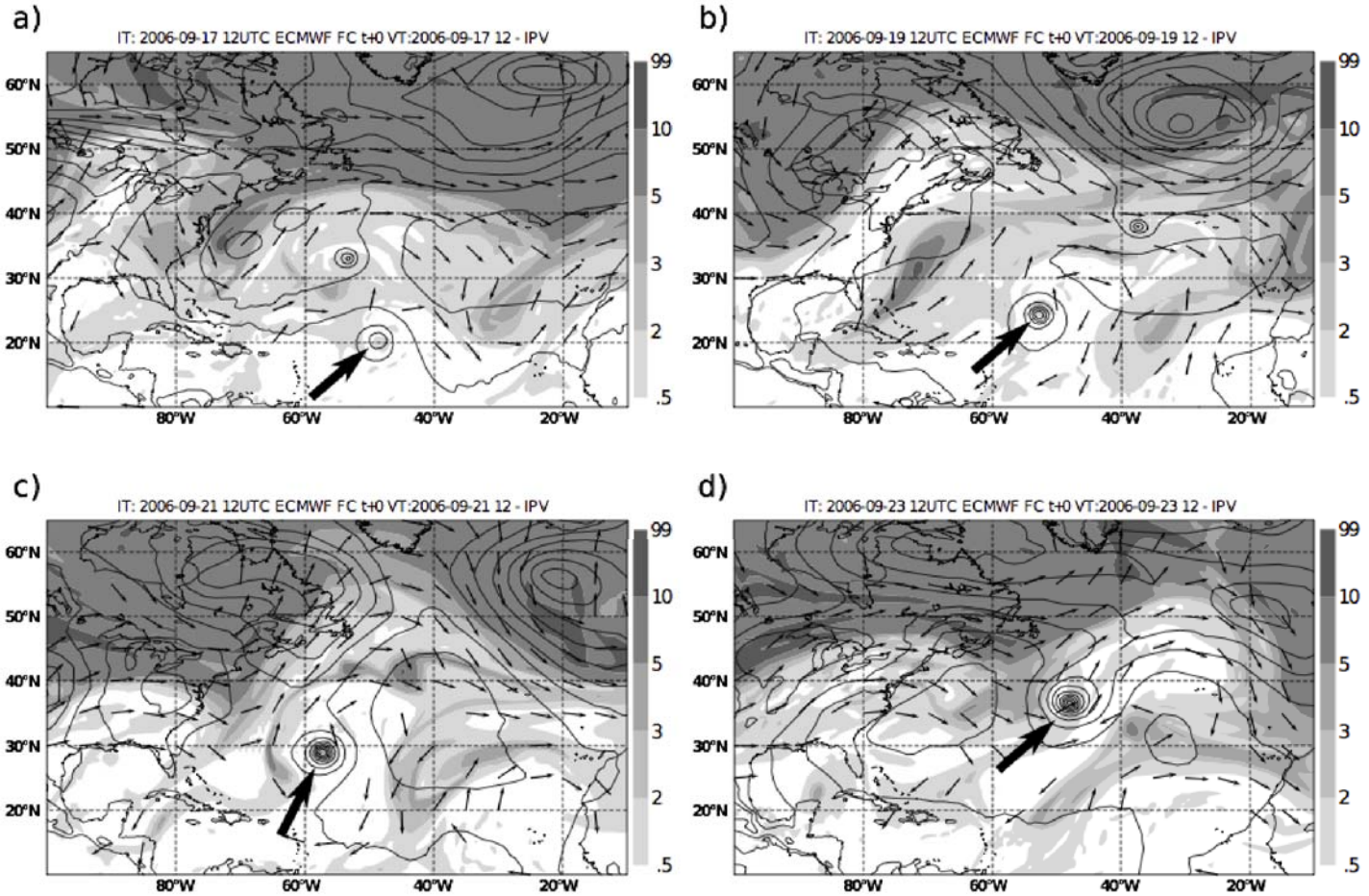

Figure 3.2: PV (in PVU, shaded) and wind direction (indicated by arrows) on $\theta = 350K$ surface and mean seal level pressure (in hPa, black contours) at: a) 17 September 2006 12 UTC, b) 19 September 2006 12 UTC, c) 21 September 2006 12 UTC and d) 23 September 2006 12 UTC. The position of Helene is marked by the arrow (from Lang et al., 2011).

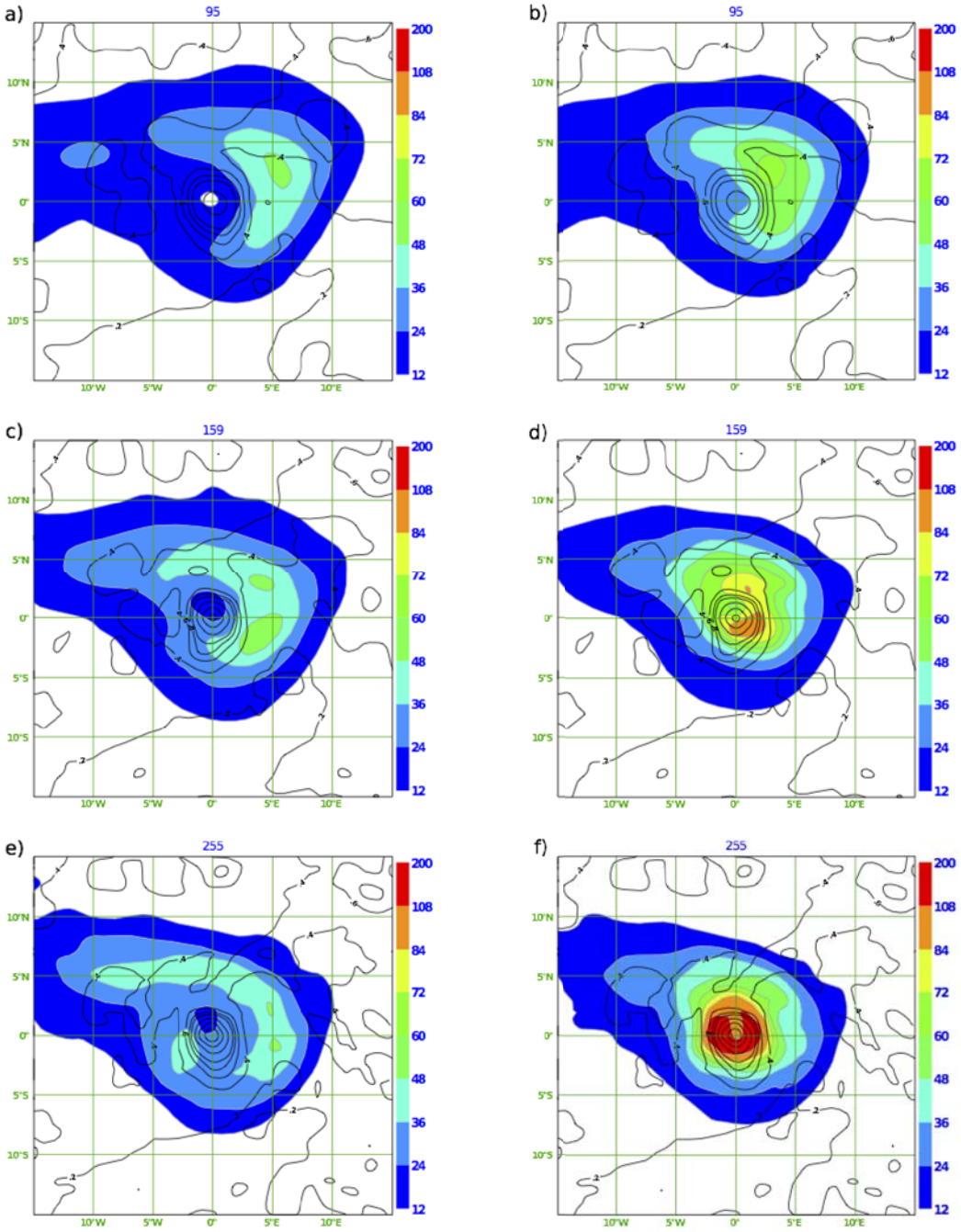

Figure 3.3: Composites of the sum of the vertically integrated total energy (in J $kg^{-1}N\ m^{-2}$; shaded) of the leading five dry (a, c, e) and moist (b, d, f) initial SVs for initialisation dates from 16 September 2006 12 UTC to 24 September 2006 12 UTC and PV (in PVU, black contours) on model level 50 ($\approx$ 850 hPa). a) and b) TL95 resolution, c) and d) TL159 resolution and e) and f) TL255 resolution (from Lang et al., 2011).

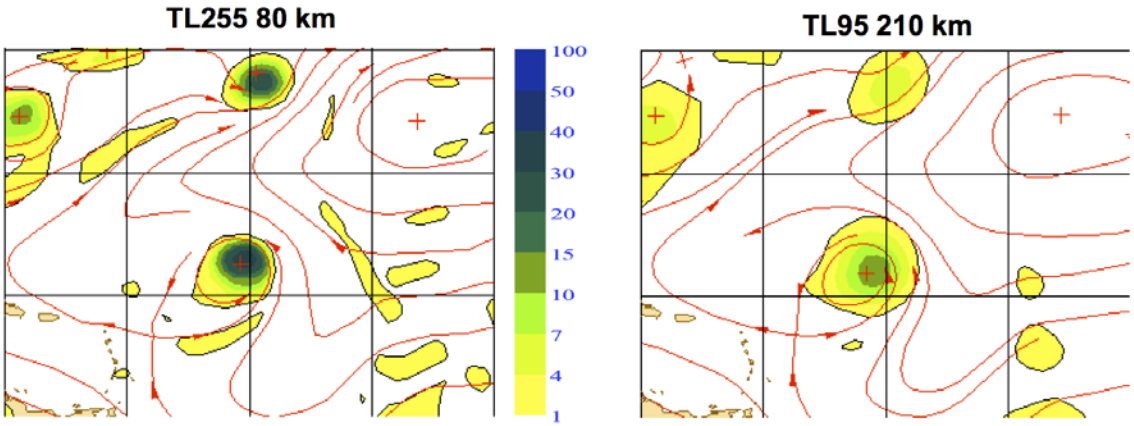

Figure 3.4: Relative vorticity (colored; in $\times 10^{-5} s^{-1}$) and streamlines (red) in 850 hPa of a) TL255 trajectory and b) TL95 trajectory after 24 hours forecast time from 17 September 2006 12 UTC.

lower resolution. However, there is a systematic difference in the intensity of Helene (compare Fig. 3.4a and b; the relative vorticity maximum in the middle of the plots is associated with Helene). As would be expected, Helene is a more intense system at higher resolution than at lower resolution, as indicated by the higher relative vorticity values at TL255 resolution. Initially these intensity differences arise solely through interpolation, since the operational high resolution analysis (TL799; approx. 25 km) is interpolated to initialize the lower resolution SV calculations. Within the forecast range the intensity differences become larger, since the gradients present in the initial fields are still too large to be sustained in the lower resolution trajectory, even after the interpolation of the initial fields to coarser resolution. An adjustment process occurs within the first hours of the forecast during which the TC weakens and broadens. Larger scale systems like the midlatitude jet are weakened also, but to a lesser extent than the TC. The trajectories of dry and moist SVs calculations with the same resolution are identical.

In general, higher resolution leads to higher growth rates of the SVs in our experiments and, as indicated by total energy spectra (not shown), more small scale structure. This is consistent with the resolution dependence of extratropical SVs (Hartmann et al. 1995, Buizza et al. 1997, Coutinho et al. 2004). Also, at higher resolution more energy is associated with the TC than at lower resolution, for which more energy is associated with other synoptic features, e.g. the subtropical high or the midlatitude jet region upstream of Helene (compare Fig. 3.5a and c). Here our composites support the findings of Komori and Kadowaki (2010), who investigated

the resolution dependence of dry SVs targeted on a TC for a single initialization date.

The horizontal distribution of the vertically integrated total energy of the leading five initial SVs is more sensitive to changes in resolution in the moist case than in the dry case. At TL95 resolution (Fig. 3.3b) the maximum of the total energy curves around the east and northeast side of the TC, approximately 300 to 500 km from its center. This typical distance was also found in previous studies (e.g. Peng and Reynolds 2006, Kim and Jung 2009a). At higher resolution, the maximum becomes more small scale and more pronounced (compare Figs. 3.3b, d and f). At TL159 resolution it moves closer to the center of Helene and for our high resolution TL255 SVs an annular structure around the center emerges with a radius of approximately 100 to 200 km (Fig. 3.3f).

The distribution and amplitude of the total energy of the dry SVs around the TC does not change as much with resolution as in the case of the moist SVs. At lower as well as at higher resolution the maximum is located east of the center of the TC (Figs. 3.3a, c and e) and the curved structure remains. The dry SVs at higher resolution do exhibit more small scale structure and higher growth rates than the lower resolution SVs, as is seen for the moist SVs. However, even though the structure of the maximum of the total energy is somewhat modified and more energy is associated with the outer core region of the TC, the curved structure persists in all calculations.

At lower resolution (TL95) the vertically integrated total energy of the leading five initial moist and dry SVs looks similar (Figs. 3.3a and b), even though the area of high vertically integrated total energy is located somewhat closer to the center of the TC and more energy is associated with the TC for the moist SVs in comparison to other synoptic systems (compare Fig. 3.5a and b). This is in line with studies by Peng and Reynolds (2006) and Kim and Jung (2009a). However, at TL255 resolution the differences between dry and moist SVs within Helene's core are striking (e.g. Figs. 3.3e and f). These differences are caused only by the inclusion of moist processes in the SV calculations since the trajectories are identical for the moist and dry SVs of the same resolution.

By examining individual initialization dates it becomes apparent that the differences in the total energy composites between higher resolution dry and moist SVs are largest for forecasts initialized before and especially during recurvature. After recurvature, the total energy signature of the leading dry and moist SVs become more similar in the vicinity of Helene (especially for the first SVs), with the maximum of

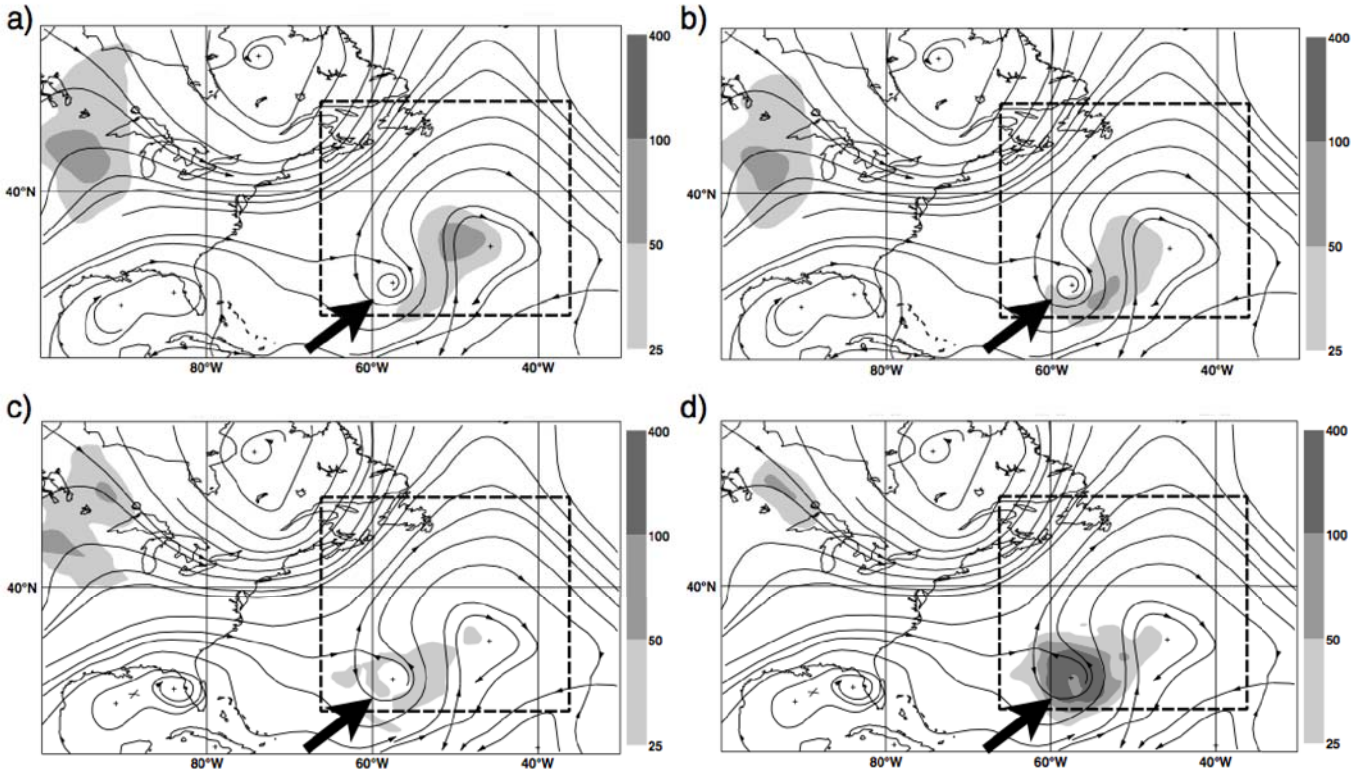

Figure 3.5: Streamlines of trajectory at 500 hPa and vertically integrated total energy (in J $kg^{-1}N\ m^{-2}$; shaded) of the leading five initial SVs from 21 September 2006 12 UTC. The SVs are targeted on Helene (the optimization region is indicated by the dashed rectangle). a) TL95 dry SVs, b) TL95 moist SVs, c) TL255 dry SVs and d) TL255 moist SVs. The position of Helene is marked by the arrow (from Lang et al., 2011).

the total energy at some distance from Helene's center. At all resolutions the region of high total energy stretches to the northwest indicating the importance of other synoptic systems, especially the upstream jet region during and after recurvature.

The potential for increased growth with increased resolution and diabatic effects can be larger for SVs associated with TCs than for SVs associated with phenomena that are already well resolved at lower resolution. As a consequence the SVs associated with TCs can be found within the leading global SVs at higher resolution. This is depicted using the total energy of the leading 20 initial SVs (Fig. 3.6) optimized for the global tropical band (30°N to 30°S). The calculations are initialized on 17 September 2006 12 UTC. At low resolution (T42) there is no signal of Helene within the leading 20 moist SVs (Fig. 3.6a). This is in line with the results of Puri et al. (2001) who found, that tropical T42 SVs do not isolate TCs as major sources of perturbation growth. However, our results show that at higher resolution (TL255) some of the leading moist SVs are associated with Helene (Fig. 3.6b). Northern Hemisphere midlatitude systems that could not be properly resolved at lower resolution also appear now in the leading high resolution SVs.

3.4 Growth Mechanisms

To identify the processes leading to the growth of the SVs and therefore dominating the predictability of the TC, we investigated the three-dimensional structure of the SVs and performed an energy flow analysis following Kwon and Frank (2008) (see Section 2.5). We illustrate some features of the SV structure using the leading (first) TL255 SV from the calculation initialised on 17 September 12 UTC (Fig. 3.7). In the PV of the trajectory (grey surface) the PV tower of Helene in the middle of the plot extends to the tropopause (indicated by the high PV values at upper levels). It is apparent that the tropopause in the vicinity of Helene is richly structured. The upper-level positive PV anomaly, which Helene encounters during its recurvature, is located northwest of Helene.

A significant part of the total energy of the leading high resolution (TL255) moist SV is embodied in a spiral structure (Fig. 3.7a). The spiral winds tightly and cyclonically upwards around the upper part of Helene's PV tower. The spiral observed here is orientated in such a way that it tilts in the horizontal and vertical against the shear of the TC (Fig. 3.8a and b). In Helene the wind speed decreases with height above approximately 900 hPa (Fig. 3.8b). A perturbation that is oriented in such

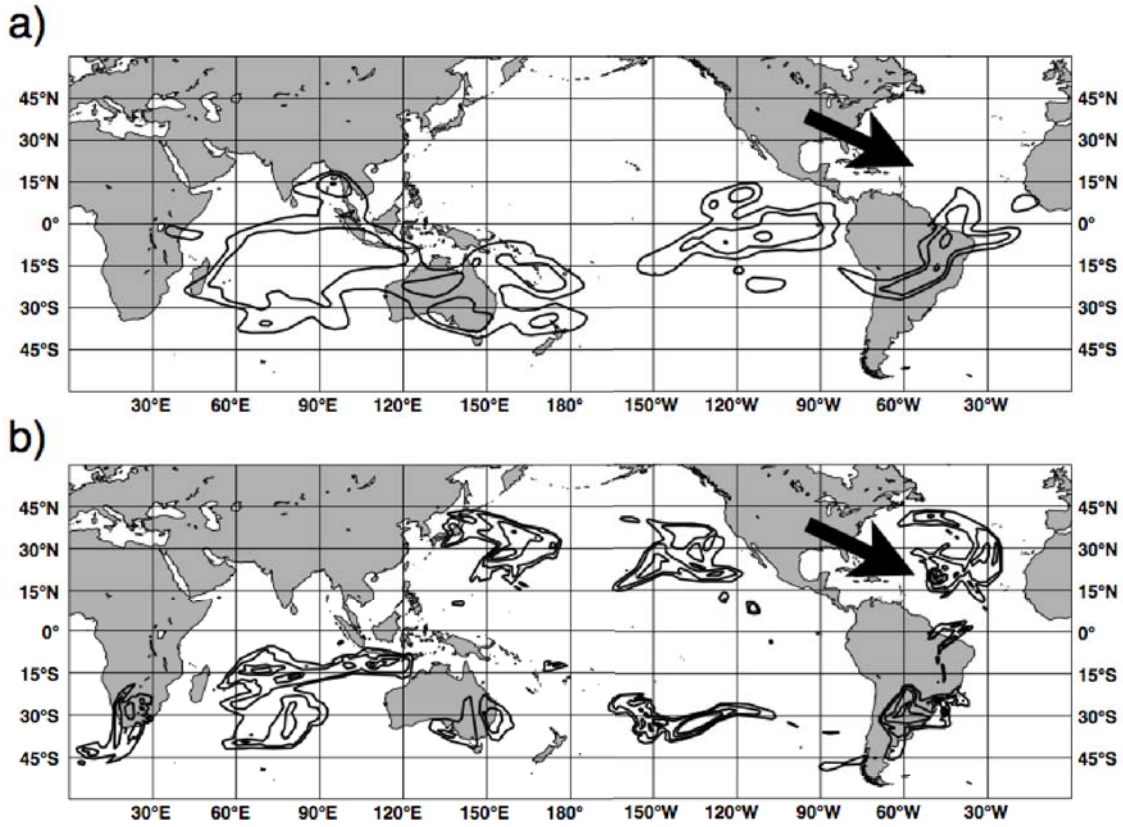

Figure 3.6: Vertically integrated total energy (black contours) of the leading 20 initial SVs from 17 September 2006 12 UTC optimized for the tropical belt (30°N to 30°S). a) T42 SVs and b) TL255 SVs. Contour lines are drawn at 5, 10, 25 and 50 $J\ kg^{-1}N\ m^{-2}$. The position of Helene is indicated by the arrow (from Lang et al., 2011).

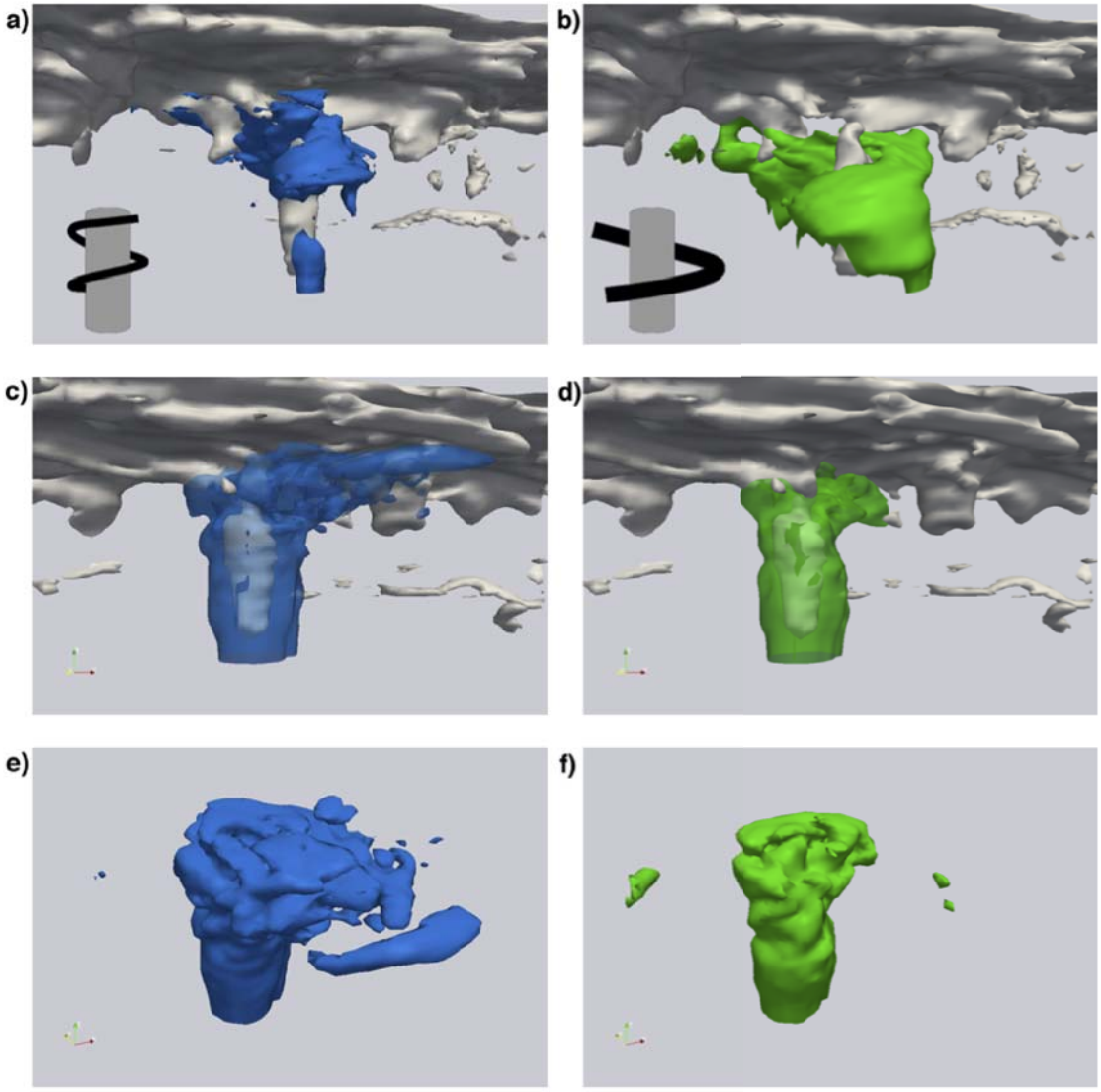

Figure 3.7: Total energy (colored surfaces) of the leading TL255 SV from 17 September 2006 00 UTC and potential vorticity (1PVU; grey surface) of accompanying trajectory. a) initial moist SV, b) initial dry SV, c) evolved moist SV and d) evolved dry SV; view is from the south. e) and f) as c) and d) but view is from the southwest top corner. For a) and b) the colored surfaces enclose 60% of the total energy of the a) moist and b) dry SV. For c), d), e) and f) the same total energy value is used to define the surface. The value is chosen so that 60% of the total energy of the evolved dry SV is enclosed. The schematic in the lower left of a) and b) sketches the PV tower of Helene and the spiral structure of the SVs (from Lang et al., 2011).

a way can extract energy from the basic current (Zeng 1983, Buizza and Palmer 1995) and grow by transient mechanisms (Orr 1907, Nolan and Farrell 1999). The horizontal and vertical tilt indicates growth by barotropic and baroclinic processes (Zeng, 1983). Most of the total energy is located around model level 30 ($\approx$ 300 hPa), where the vertical shear of the azimuthal velocity has its maximum.

A large part of the total energy of the leading TL255 dry SVs is also wrapped around the TC (Fig. 3.7b), but the structure is deeper, possesses a smaller vertical tilt and is not wound as tightly around the PV tower of Helene as in the case of the leading moist SV. If a surface were chosen that encloses a higher percentage of the total energy, it would become apparent that part of the structure that is dominant for the dry SV is still present for the moist SV. So a part of the energy of the leading moist SVs is shifted from one region where the dry SV detects the largest instability to a "new" one that features even stronger growth in the presence of diabatic effects.

For the moist SV, the total energy (Eqn. 2.5) is dominated by the potential energy (associated with the temperature perturbation T'). The maximum of the potential energy is located around 300 hPa, while most of the kinetic energy (associated with the wind perturbation u' and v') is located between 700 and 200 hPa (Fig. 3.9a). For dry SVs, the total energy is split more equally between kinetic and potential energy (Fig. 3.9b). Here, most of the kinetic energy is located in the mid to lower troposphere around 600 hPa and most of the potential energy between 500 and 200 hPa.

Within the optimization interval the spiral structures of the initial SVs are untilted by the flow. The total energy of the evolved SVs is dominated by the kinetic energy and thus the wind perturbations are more pronounced than the temperature perturbation (not shown). Examination of the perturbation vorticity indicates that the leading (moist and dry) SV develops a deep dipole structure in the mid to lower troposphere. The dipole is associated with a horizontal displacement of the TC. However, from the structure of the dipole, it is apparent that the leading evolved SVs, if added to the trajectory, would not only cause a horizontal displacement but also a structural modification of the TC.

After 48 hours the PV tower of Helene is enclosed by the total energy signature of the evolved SV (Fig. 3.7c and d). At upper levels, around 200 hPa, the leading evolved moist SV is associated with the low PV anomaly of Helene's outflow, which possesses a larger horizontal extent than Helene's PV tower. This leads to a mushroom like appearance of the evolved moist SV. It is apparent that while the leading moist and the leading dry SV show comparable growth in the lower to mid

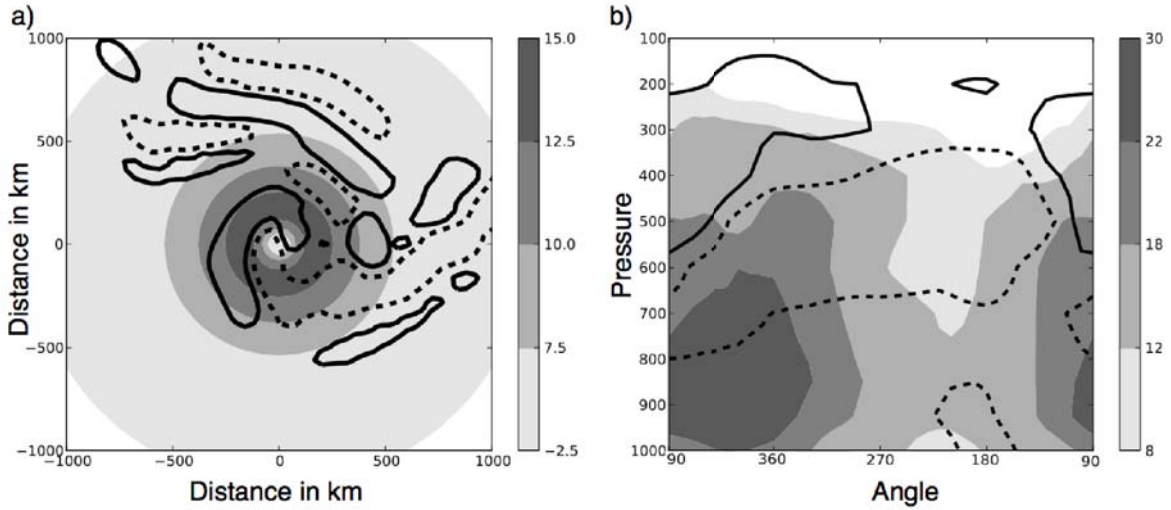

Figure 3.8: a) Azimuthally averaged azimuthal wind speed of trajectory ($m\ s^{-1}$; shaded) at 400 hPa and relative vorticity perturbation of leading TL255 moist SV (contours) from 17 September 12 UTC. Contour lines are drawn at $-0.2 \times 10^{-5} s^{-1}$ (dashed) and $0.2 \times 10^{-5} s^{-1}$ (solid). b) Azimuth-pressure section around Helene at a radius of 200km. The azimuthal angle is measured anticlockwise from North. Plotted are the azimuthal wind speed of the trajectory ($m\ s^{-1}$; shaded) and the temperature perturbation of the leading TL255 moist SV (contours). Contour lines are drawn at $-0.3K$ (dashed) and $0.3K$ (solid) (from Lang et al., 2011).

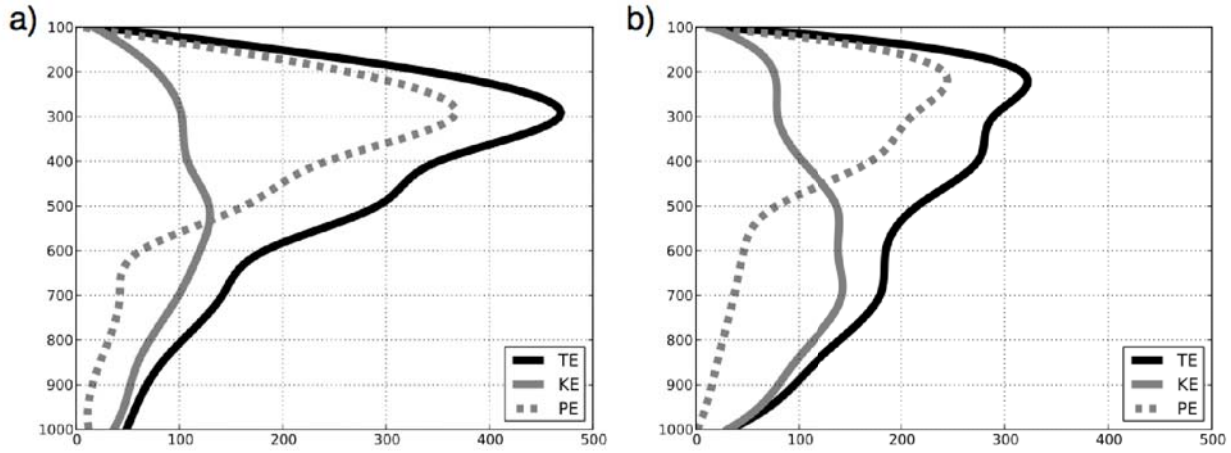

Figure 3.9: Averaged vertical profiles of the energy of the sum of the leading five initial a) moist and b) dry SVs. Depicted are total energy (solid black line), kinetic energy (solid gray line) and potential energy (dashed gray line). Horizontally integrated total energy (in J $kg^{-1}m^2$) on the x-axis and pressure in hPa on the y-axis (from Lang et al., 2011).

troposphere, differences are large in the upper troposphere within the outflow region of Helene (Fig. 3.7c, d, e and f). Here the leading moist SV grows more strongly than its dry counterpart. The leading five dry SVs do show a signal associated with upper tropospheric features. However, the signal is weaker than in the moist case and emphasizes structures associated with the approaching upper-level positive PV anomaly more strongly than those associated with the outflow region of Helene.

To further investigate and quantify the processes that lead to the growth of the initial SVs we apply the energy flow analysis (Kwon and Frank, 2008) to our EPS experiments (see Section 3.1.2). We calculate the conversion terms for the unperturbed control forecasts and the perturbed forecasts. To analyse how the conversion terms are changed by the SV perturbations, the conversion terms of the unperturbed forecast are subtracted from the conversion terms of the perturbed forecasts. Since we focus on the initial SVs, and therefore investigate the energy fluxes at $t = 0$, the nonlinear evolution of the SVs does not impact the results discussed in this Section.

Figure 3.10 shows composites of the changes induced by the leading five initial SVs to the barotropic and baroclinic energy conversion terms (hereafter called energy fluxes). To generate the composites we sum the magnitude of the changes caused by the leading five SVs and average over all initialization dates. As done previously, the fields are composited relative to the cyclone center. Finally, the composites are integrated azimuthally. As a result, the composites display the areas where, on average, the largest changes to the energy fluxes are induced by the SVs.

The composite of the changes to the barotropic energy fluxes due to the higher resolution (TL255) dry SVs indicate several regions where the SVs have an impact on the TC energetics. The changes to the barotropic energy fluxes are large in a region between 400 and 700 km from the center of Helene, with a local maximum between 700 and 500 hPa and another local maximum in the upper troposphere around 200 hPa (Fig. 3.10a). Furthermore, there is a region with high values at 200 hPa and approximately 1000 km from Helene's center. This feature is connected to synoptic features of the storm environment. The changes to the baroclinic energy fluxes due to the dry SVs are largest in the upper troposphere between 300 and 200 hPa (Fig. 3.10b). These changes have a higher amplitude than the changes to the barotropic energy fluxes, but are more localized. In comparison to the dry SVs, the moist SVs induce larger changes to both baroclinic and barotropic energy fluxes. The maximum of the changes to the barotropic energy fluxes is located approximately 200 km from the center of the TC (Fig. 3.10c). This is significantly closer to the center than in case of dry SVs. The two local maxima near 600 hPa and 200 hPa

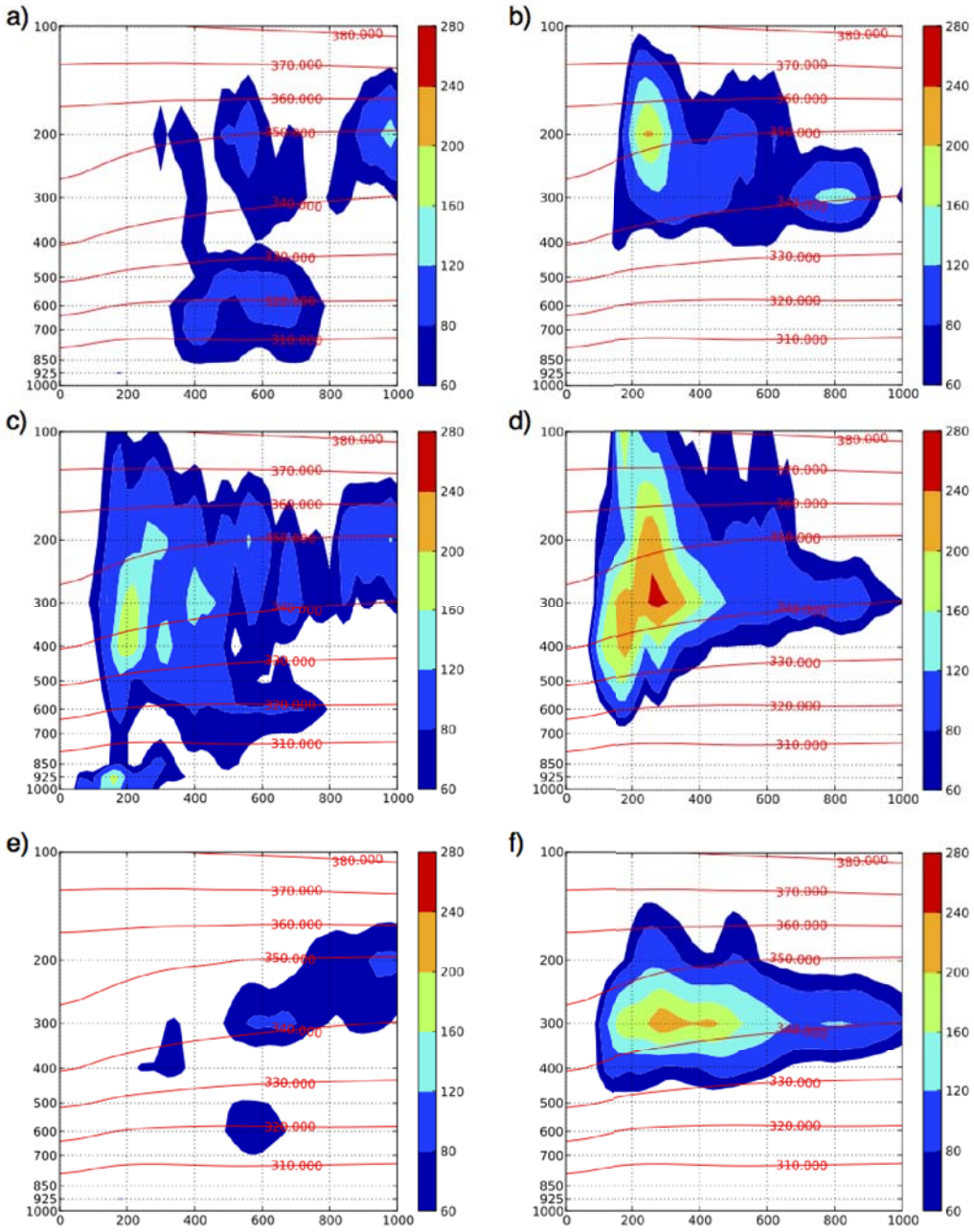

Figure 3.10: Composites of the sum of the absolute values of the changes induced by the leading five initial SVs to the barotropic (a, c, e) and baroclinic (b, d, f) energy conversion terms (color shading) and θ (red contours) of the unperturbed TL255 trajectory. a) and b) TL255 dry SVs, c) and d) TL255 moist SVs and e) and f) TL95 moist SVs. Distance from the center in km on the x-axis and pressure in hPa on the y-axis. For a detailed explanation see text (from Lang et al., 2011).

observed in the dry SV case remain in the moist SV case. The moist SVs also induce stronger changes in the barotropic energy fluxes close to the surface (1000 - 925 hPa). The amplitude of the changes to the baroclinic energy fluxes (Fig. 3.10d) due to the moist SVs have a larger amplitude than the changes to the barotropic energy fluxes. The highest values are located around 300 hPa, and 100 to 300 km from the center of Helene. Thus the maximum is located at lower levels than for the dry SVs and it has a significantly larger amplitude. Again, the moist SVs show a mixture of structures present in the dry SVs and new structures not seen in the dry SVs.

The lower resolution (TL95) moist SVs exhibit features of both higher resolution moist and dry SVs. Their changes to the barotropic energy fluxes (Fig. 3.10e) are more similar to those of the TL255 dry SVs since the structures of the TL255 moist SVs close to Helene's center are not present. The changes to the baroclinic energy fluxes (Fig. 3.10f) show some features of the TL255 moist SVs. The maximum is located at 300 hPa at a distance of approximately 300 km from Helene's center. But the region of high values has a much smaller vertical extent than the maximum of the TL255 moist SVs and also a smaller amplitude. This is consistent with the differences of the horizontal distribution of the total energy of the TL255 and TL95 moist SVs (see Section 3.4).

The SVs exploit different processes within and in the vicinity of Helene to achieve their growth. In the mid to lower troposphere a local maximum of the TL255 dry SV is located approximately 600 km from Helene's center. At this distance the radial PV gradient changes sign (Fig. 3.11a), the criterion for barotropic instability (Montgomery and Shapiro, 1995), which was also observed by Peng and Reynolds (2006). For the dry SVs, baroclinic growth takes place at upper levels. Here the maximum is located at a height and at a distance from Helene's center where the criterion for baroclinic instability is fulfilled, i.e. the radial PV gradient along an isentrope changes sign with height (Kwon and Frank, 2005). This is the case between the 350K and 360K surface, 300 km from Helene's center (Fig. 3.11b).

In our calculations the initial SVs are tilted against the shear of the TC and are located close to regions where instability criteria are satisfied. The horizontal and vertical tilt indicates growth by transient processes (Farrell 1982, Nolan and Farrell 1999). This may indicate that, after a phase of rapid initial growth, the SVs exploit the existing barotropic and baroclinic instability mechanisms of the flow. This behaviour is consistent with studies of the growth of extratropical SVs (Badger and Hoskins 2000, Hoskins et al. 2000) and with the results of Yamaguchi et al.

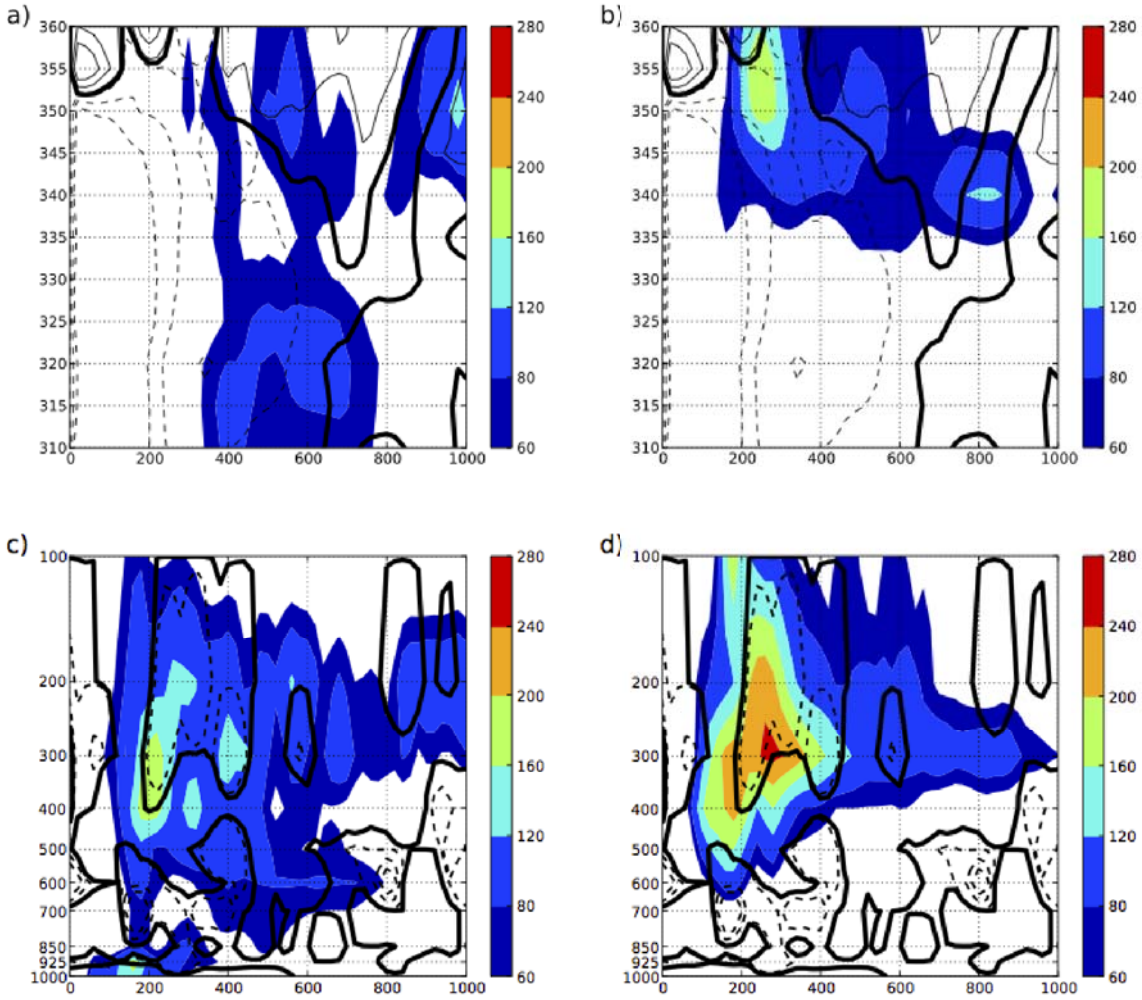

Figure 3.11: Changes to a) barotropic and b) baroclinic energy conversion terms by TL255 dry SVs (color shading) and radial PV gradient along θ-surface of trajectory at initialization time (thick line zero-contour, dashed lines indicate negative values). c) changes to the barotropic and d) to the baroclinic energy conversion terms by TL255 moist SV (color shading) and saturated moist PV (calculated with the saturated equivalent potential temperature; thick line zero-contour, dashed lines indicate negative values) . Distance in km on the x-axis and pressure in hPa on the y-axis (from Lang et al., 2011).

(2011) who assessed the growth of SVs targeted on idealised TC-like vortices in a barotropic model. These studies show that if longer optimization intervals are applied the SVs exhibit a rapid initial growth phase followed by slower more modal growth. The inclusion of moist processes in the SV calculations brings the maximum of the SVs close to where the vertical shear of the azimuthal velocity is largest, at around 300 hPa (compare Figs. 3.12a and 3.10c). In addition, as stated above, the structure of the SV becomes more baroclinic.

This change in structure and location can be explained by considering growth mechanisms of extratropical SVs which are usually located close to regions where shear is large (Buizza and Palmer 1995, Reynolds et al. 2001). This comparison is justified, since the low level circular jet of a TC and its warm core can be viewed as analogous to a midlatitude jet (Nolan and Montgomery 2002, Yamaguchi and Majumdar 2010). In the Eady model for baroclinic instability, the maximum growth rate is proportional to vertical shear and inversely proportional to the static stability N (Badger and Hoskins, 2000). Modal and transient growth in the Eady model is enhanced in the presence of latent heating (Tippett 1999, Badger and Hoskins 2000), because the effective static stability is reduced in saturated moist flow (Bennetts and Hoskins, 1979). As a consequence, the baroclinic growth of extratropical moist SVs is enhanced (Coutinho et al., 2004). From our results we conclude that these arguments also apply for SVs associated with Helene's TC core region.

The maximum changes to the baroclinic and barotropic energy fluxes due to the TL255 moist SVs tend to be co-located with regions where the saturated moist PV (calculated with the saturated moist potential temperature, θ_e^*) is negative (Fig. 3.11c and d). Thus a further candidate for SV growth in our calculations is the exploitation of conditional symmetric instability (CSI; Bennetts and Hoskins 1979, Jones and Thorpe 1992). For a TC, CSI is considered to exist in the upper eyewall region (Emanuel 1989, Schultz and Schumacher 1999), which is consistent with our results.

It is apparent that no single process can be held responsible for the SV growth, but a mixture of processes is relevant. However, diabatic processes are necessary to attain the strong growth within the core region of Helene.

The SV perturbations propagate into regions of high wind speed within the optimization interval. This property is seen also for extra tropical SVs propagating upward to the jet level (Buizza and Palmer, 1995). In contrast to extratropical SVs, that are usually located below the jet, the SVs in Helene are located between the upper-level outflow jet and the lower-level maximum winds (Fig. 3.13a). The pertur-

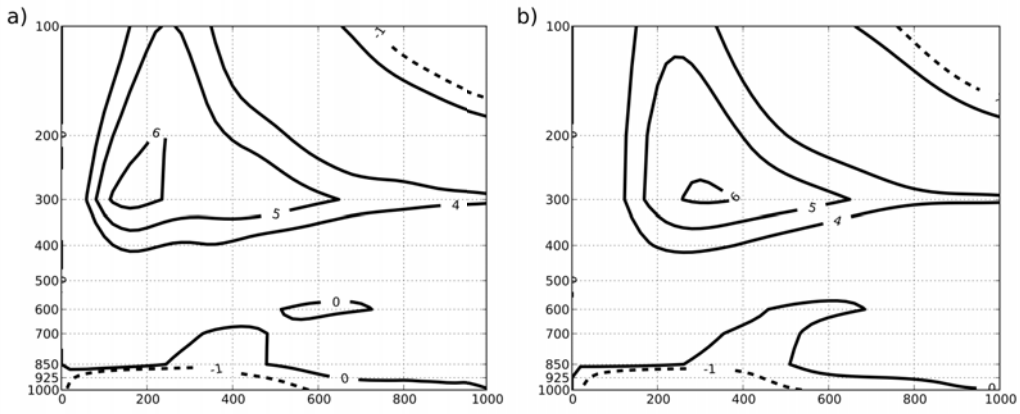

Figure 3.12: Composites of vertical gradient of azimuthal velocity (in $10^{-4} m\ s^{-1} Pa^{-1}$) at initialization time of a) TL255 and b) TL95 trajectory. Distance from center in km on the x-axis and pressure in hPa on the y-axis (from Lang et al., 2011).

bations then propagate upwards and downwards, as indicated by the position of the local total energy maxima at the different times (Fig. 3.13a to d). After 48 hours, the local maxima of the total energy of the leading SVs are located at the lower and upper tropospheric maxima of the azimuthal wind speed (Fig. 3.13d). Before recurvature the strongest upper-level flow is associated with the anticyclonic outflow jet of Helene and later, when Helene moves into the midlatitudes, with the midlatitude jet also. The lower maximum is collocated with Helene's radius of maximum winds.

As described in Section 3.2, the TC is better resolved at TL255 resolution, resulting in a more intense system featuring larger vertical and horizontal velocities along with stronger vertical and horizontal shear. The static stability within the core of the TC is reduced. These effects become more pronounced within the forecast time. In addition, at lower resolution, the region of maximum vertical shear moves further away from Helene's center (compare Fig. 3.12a and b). This explains the differences of the horizontal distribution of the total energy and the energy fluxes between the higher and lower resolution moist SVs.

3.5 Potential Impact on the EPS

In the previous sections we described the characteristics of SV growth for Helene as a function of resolution and diabatic processes. The question arises what is

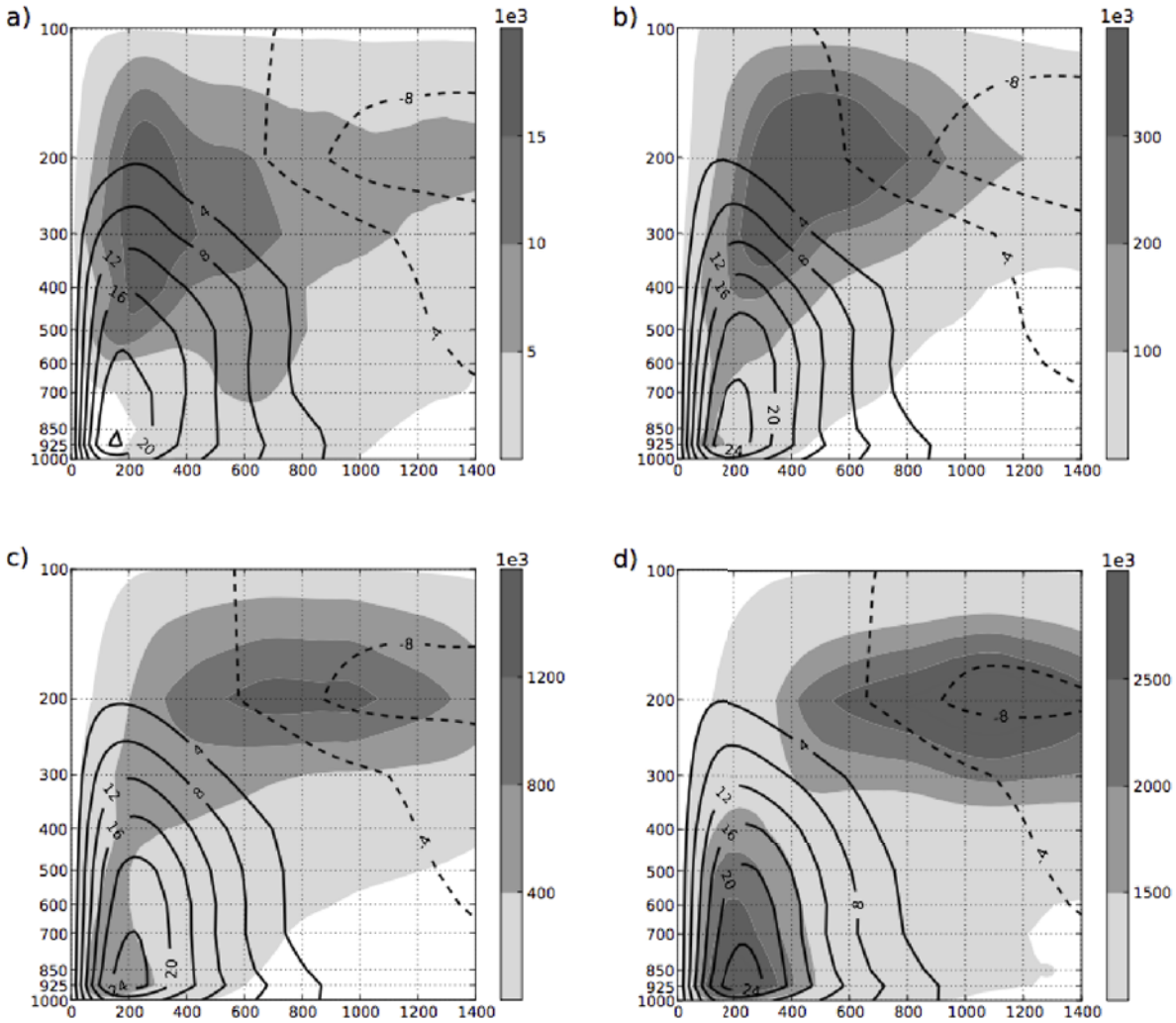

Figure 3.13: Composites of the azimuthally integrated total energy of TL255 moist SVs (shaded) and the azimuthal velocity (in $m\ s^{-1}$; black contours) of the TL255 trajectory after a) 0h, b) 12h, c) 24h and d) 48 hours forecast time. Distance from center in km on the x-axis and pressure in hPa on the y-axis (from Lang et al., 2011).

the impact of these different SVs on the EPS. To address this issue we conducted idealized EPS experiments, designed as described in Section 3.1.2. To compare the spread (ensemble standard deviation) of the different setups the 200 hPa and 850 hPa spread of the wind speed is integrated within the optimization region, area weighted and then averaged over all initialization dates. The spread after 48 hours of the experiments with TL255 moist, TL95 moist and TL255 dry SVs are listed in table 3.1.

Varying resolution and including diabatic effects in the SV computations results in different spread characteristics. The EPS experiments initialised with TL255 moist SVs exhibit larger spread than the EPS experiments initialised with TL255 dry SVs and than the EPS experiments with lower resolution moist and dry SVs. The spread differences between TL255 and TL95 moist SVs are larger than the differences between TL255 moist and dry SVs. When Helene is located within the tropics the spread at upper levels for the TL255 moist SVs is considerably larger in comparison to the TL255 dry SVs (up to 130%), with smaller differences at lower levels.

For the case initialized on 17 September 2006 12 UTC Helene is still located in the subtropics after 48 hours forecast time. At 850 hPa (Fig. 3.14a) there is an increase of spread in the vicinity of and within the TC for the TL255 moist SVs relative to the TL255 dry SVs. There are some minor remote changes that are induced by very small changes of the initial fields caused by adding the localized SV perturbation to the spectral fields, which then amplify due to strong instabilities in dynamically unrelated locations (Hodyss and Majumdar, 2007). At 200 hPa the differences between the experiments are associated with the outflow of Helene. The biggest differences are located along the outflow channel Helene develops during the forecast (Fig. 3.14b, the outflow channel is indicated by the blue arrow). Here the streamlines are curved anticyclonically originating from Helene's center (at 23°N, 53°W). This highlights the impact of the TC on the predictability of the upper troposphere. The differences between the EPS experiments travel along the outflow deep into the tropics. The differences between the TL255 moist and TL95 resolution SVs draw a qualitatively similar picture (not shown). The same structures as for TL255 moist SVs versus TL255 dry SVs emerge, but the differences are larger (as indicated by the mean values in table 3.1).

For the case initialized on 21 September 2006 12 UTC, Helene moves into the midlatitude flow and starts to undergo ET. After 48 hours forecast time the outflow of Helene has already started to interact with the midlatitude jet. In the lower to

Res.	type	mean spread 850 hPa	mean spread 200 hPa	mean ratio 850 hPa	mean ratio 200 hPa
TL255	moist	1.8	2.9	-	-
TL255	dry	1.6	2.6	1.11	1.13
TL95	moist	0.8	1.4	2.29	2.11

Table 3.1: Area weighted ensemble standard deviation of wind speed (in $m\ s^{-1}$) of the EPS experiments initialized with different set of SVs after 48 hours (averaged over all initialization dates). The mean ratio indicates how much larger the spread of the EPS experiments initialized with TL255 moist SVs is on average (from Lang et al., 2011).

mid troposphere the largest differences between the TL255 moist and dry SVs are associated with Ex-Helene itself (Fig. 3.14c; at this time Helene is located at 38°N and 47°W), but there is also a clear downstream impact. Large differences exist at upper levels, especially in the region downstream of Helene (Fig. 3.14d). These differences are injected by the outflow of Helene into a very broad region in the midlatitude flow, including the subtropical high east of Helene. This results in an increased spread within the subtropics that then propagates along the anticyclonic circulation of the subtropical high into the tropics. Therefore there is a midlatitude and a subtropical-tropical downstream effect to be observed. Again the differences between the TL255 moist and TL95 lower resolution SVs show qualitatively similar structures but quantitatively larger differences. Both increasing the resolution of the SVs or including moist processes leads to a decrease in spread over the North American continent upstream of Ex-Helene. This decrease is caused by the fact that a larger part of the total energy of the initial SVs is associated with the upstream jet region than in case of higher resolution moist SVs.

For TCs the minimum pressure and and track are important forecast parameters. Before recurvature the TL255 moist and dry SVs cause a similar spread of the position of Helene after 48 hours. In the early tropical phase (16 and 17 September) the position spread caused by the TL255 dry SVs is slightly larger in comparison to the TL255 moist SVs (Fig. 3.15a). During and after recurvature the position spread caused by the TL255 moist SVs is larger. Furthermore, TL255 moist SVs cause larger spread in minimum pressure than TL255 dry SVs (Fig. 3.15b). The differences in the early tropical phase are consistent with the fact that for moist SVs more energy is located at higher levels and associated with the TC core. Apparently this leads to a stronger modification of TC intensity. At this time the TL255 dry SVs have larger amplitude at lower levels at some distance from the center, resulting in a larger spread of Helene's track. However, the subsequent larger growth of the moist SVs compensates for this effect. The largest spread is observed for the EPS forecast from 21 September 2006 12 UTC as the TC moves into the midlatitudes.

3.6 Quantification of Nonlinearities

If SVs are used to study atmospheric phenomena such as a TC, it is important to check whether the linearity assumption is justified and hence if the SVs evolve in a similar manner when they are added to the nonlinear model or the linear model. If

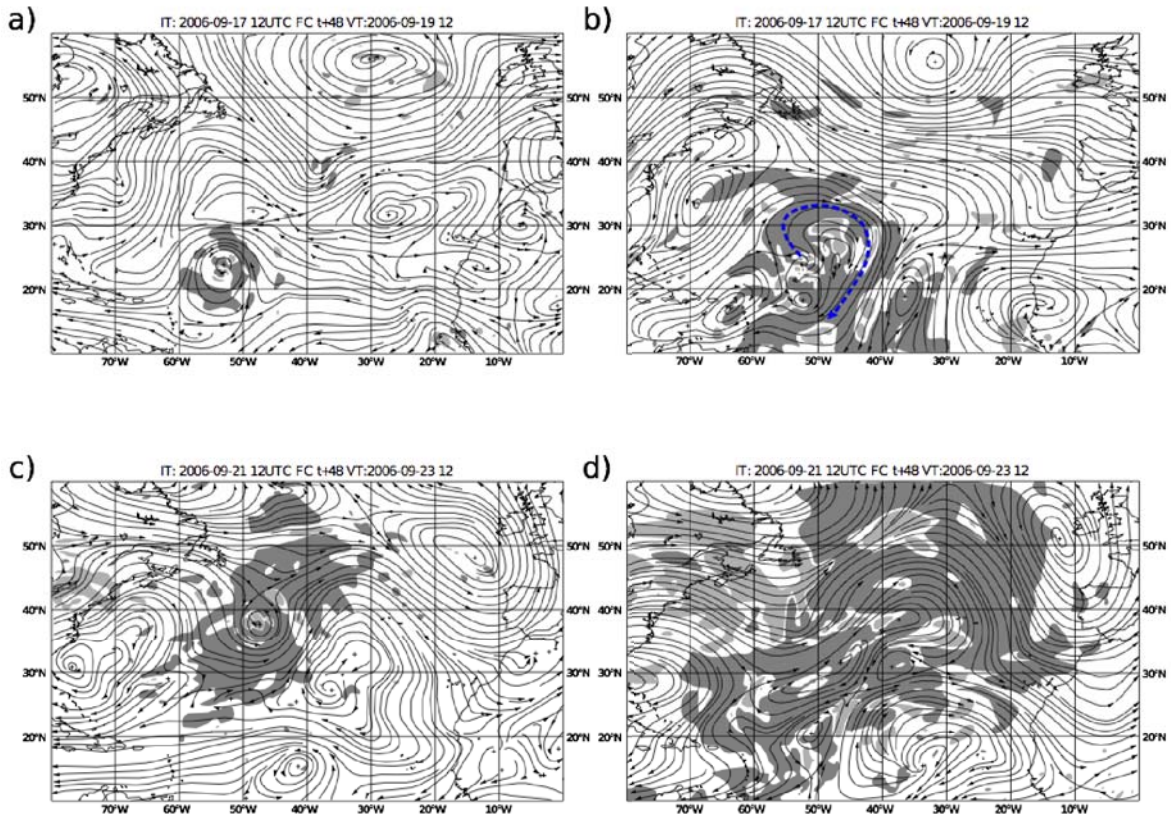

Figure 3.14: Plots show differences of ensemble standard deviation of wind speed between two EPS-experiments initialized with TL255 moist and TL255 dry SVs after 48 hours forecast time. Dark grey shading indicates increased ($> 0.5\ m\ s^{-1}$) and light grey shading decreased ($< -0.5\ m\ s^{-1}$) spread relative to the experiment with TL255 dry SVs. a), c) 850 hPa and b), d) 200 hPa. Black streamlines show flow from unperturbed (control) forecast. a), b) initialized on 17 September 2006 12 UTC and c), d) initialized on 21 September 2006 12 UTC (from Lang et al., 2011).

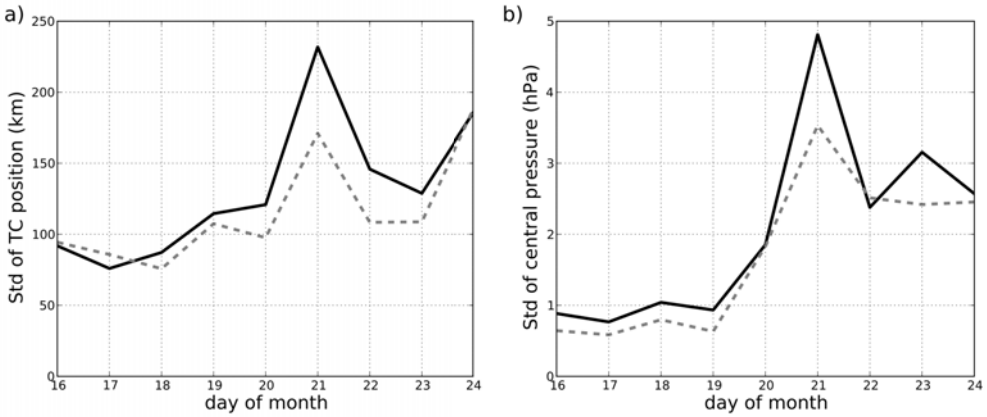

Figure 3.15: Spread (standard deviation) of Helene's position (a) and of minimum pressure (b) at 48 hours forecast time for the EPS experiment with TL255 moist SVs (solid black line) and TL255 dry SVs (dashed grey line) (from Lang et al., 2011).

this is the case, then the perturbations identified by the SV formalism are relevant for the nonlinear predictability of the phenomenon under consideration.

To quantify how linear the evolution of the SV perturbations is we follow the approach of Gilmour et al. (2001) and Buizza (1995) (see Section 2.7). The experiments to test the linear assumption were performed by evolving the SVs with the nonlinear model at a resolution of TL255. The scaling of the SVs was carried out as described in Section 3.1.2. We use streamfunction variance at 500 hPa as the metric to calculate the anticorrelation and the relative nonlinearity. The manner in which the linearity of the SVs in the nonlinear model changes if the resolution of the SVs is increased or diabatic effects are accounted for is given in table 3.2. The measures of linearity are evaluated in the optimization region after 48 hours forecast time. The mean values of the anticorrelation and the relative nonlinearity are averaged for all SVs and initialisation dates. In addition to the mean value, the upper and the lower bound of the linearity measures are given.

The upper bounds of the relative nonlinearity and the anticorrelation are given by the highest values that occur for all SVs from all initialization dates at the specific forecast time. Similarly, the lower bounds are given by the lowest values of the relative nonlinearity and anticorrelation that occur at the specific forecast time. An increase of resolution results in a decrease of linearity. This is indicated by both the relative nonlinearity and the anticorrelation (Table 3.2). In line with the mean, the upper and lower bound of the linearity measures show a reduction of linearity. The

Resolution	moist / dry	SVs	$\bar{l}$	$l\uparrow$	$l\downarrow$	$\overline{\Theta}$	$\Theta\uparrow$	$\Theta\downarrow$
T42	moist	1-5	0.85	0.98	0.31	0.53	1.19	0.22
TL95	moist	1-5	0.80	0.97	-0.16	0.63	1.52	0.24
TL159	moist	1-5	0.70	0.94	-0.80	0.75	1.91	0.34
TL255	moist	1-5	0.60	0.92	-0.80	0.86	1.91	0.42
T42	dry	1-5	0.87	0.97	0.64	0.52	0.85	0.24
TL255	dry	1-5	0.78	0.95	0.42	0.67	1.18	0.31
TL255*	moist	1-5	0.71	0.97	-0.71	0.72	1.89	0.29
TL255*	dry	1-5	0.82	0.96	0.17	0.58	1.29	0.28
TL255*	moist	1	0.83	0.91	0.58	0.60	0.92	0.46
TL255*	dry	1	0.87	0.95	0.69	0.51	0.79	0.32

Table 3.2: Relative nonlinearity Θ and anticorrelation l of the linearity experiments after 48 hours forecast time. An overbar denotes the mean over all SVs and all initialisation dates. $\uparrow$ denotes the upper bound and $\downarrow$ denotes the lower bound of the linearity indices. The * marks experiments with a reduced scaling of the initial amplitude of the SVs. The column labeled with "SVs" indicates the SVs that are considered for calculating the linearity measures (from Lang et al., 2011).

inclusion of diabatic effects reduces the linearity also. While this effect is relatively small at low resolution, it becomes more pronounced at higher resolution.

The T42, TL95 and TL159 moist SVs meet the criterion ($l > 0.7$, $\Theta < 0.75$) of Gilmour et al. (2001) for the usefulness of the linear assumption, while the TL255 moist SVs have a lower mean anticorrelation (0.6) and a higher mean relative nonlinearity (0.86) than required. In contrast, the TL255 dry SVs still meet the criterion. However, by reducing the initial amplitude of the SVs by a factor of 2 it is possible to improve the linear assumption in the case of TL255 SVs (Table. 3.2). The relative nonlinearity is reduced from above 0.8 to around 0.7 and the anticorrelation lies slightly above 0.7. A further reduction of the initial amplitude by a factor of 2 degraded the linearity due to a declined signal-to-noise ratio. The linearity is improved further if only the leading SV is taken into account (this does not change the results obtained in Section 3.4), which was also reported by Kim and Jung (2009a). In this case, the relative nonlinearity for the TL255 moist SVs with reduced initial amplitude drops to 0.6 and their anticorrelation increases to 0.83. Examination of the streamfunction fields after 48 hours forecast time of the positive (δ^+) and negative (δ^-) perturbations reveals that often the patterns are shifted relative to each other, which results in a low anticorrelation (high relative nonlinearity) even though the patterns look quite similar (Reynolds and Rosmond, 2003). Nevertheless, even

with reduced linearity in comparison to the the dry and lower resolution moist SVs, the TL255 moist SVs succeed in producing stronger growth and larger spread (as shown in Section 3.5). Therefore their physical relevance is clear since they identify faster-growing structures.

3.7 Further Cases

To obtain an indication of how general the results of the sensitivity experiments of the SVs associated with Helene are, we calculated SVs for selected initialization dates for the TCs Sinlaku (2008) and Jangmi (2008). These TCs were located in the western North Pacific, in contrast to the Atlantic case Helene (2006). Furthermore, we tested the effect of a vertically confined norm below 500 hPa on the SVs for these cases. In contrast to the Helene experiments, the leading 10 SVs are calculated. However, taking only the leading 5 SVs into account as for Helene, does not alter the findings. The results of the experiments for Typhoon Sinlaku and Jangmi are consistent with the results obtained for Hurricane Helene.

In the case of Sinlaku, the inclusion of diabatic effects within the TL255 SV calculations for 14 September 2008 00 UTC results in a destabilization of the TC core region. In contrast, the dry SVs feature large total energy values in the outer region of Sinlaku (compare Fig. 3.16a and b). If the norm is confined below 500 hPa, the upstream midlatitude structures are altered (compare Fig. 3.16a and c). Also, the amplitude of the total energy maximum within the core region of Sinlaku is reduced. This is caused by the fact that the inner core structures strongly affect the ouflow of the TC (see Sect. 3.4). If the norm is confined below 500 hPa, the upper level structures are not considered for measuring the SV growth. Hence their relative importance is somewhat reduced. Nevertheless the inner core is identified still by the SV formalism as a sensitive region in the case of Sinlaku.

In the case of Jangmi the inclusion of diabatic effects within the TL255 SV calculations for 26 September 2008 00 UTC destabilizes the TC core region also. The total energy maximum north of Jangmi moves closer to the TC center in the case of moist SVs (compare Fig. 3.17a and b). Confining the norm below 500 hPa emphasizes structures some distance away from the TC center (around 500 km) more strongly for both moist (compare Fig. 3.17a and c) and dry SVs (compare Fig. 3.17b and d). However, considerable total energy values are found still within Jangmi's core region in case of moist SVs. Reducing the resolution of the SV calculations to

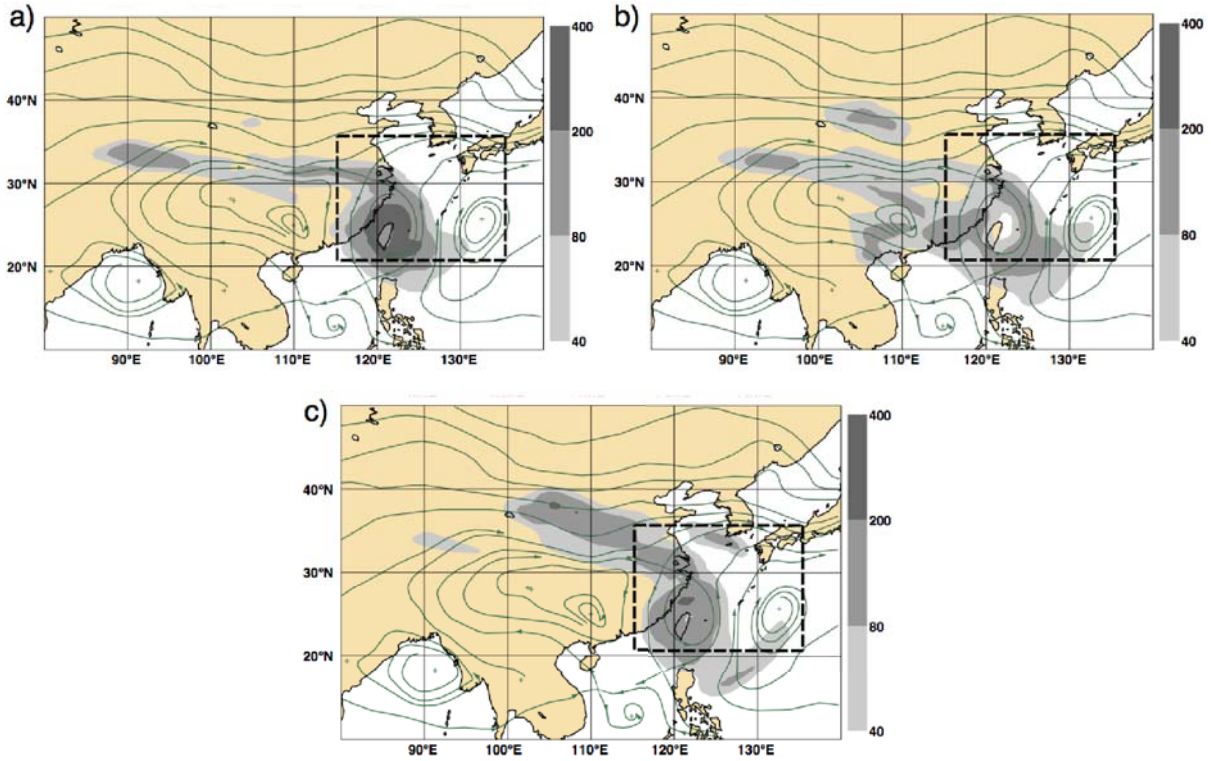

Figure 3.16: Streamlines of trajectory at 500 hPa and vertically integrated total energy (in J $kg^{-1}N\ m^{-2}$; shaded) of the leading 10 initial SVs from 14 September 2008 00 UTC. The SVs are targeted on Typhoon Sinlaku (the optimization region is indicated by the dashed rectangle). a) TL255 moist SVs, b) TL255 dry SVs, c) TL255 moist SVs optimized below 500 hPa.

TL95 results in lower total energy values in the vicinity of the TC (Fig. 3.17e and f). In the case of moist SVs, the local maxima within Jangmi's core region disappear (compare Fig. 3.17c and e).

3.8 Downstream Impact

During and after the ET of Hurricane Helene (2006) an intense hurricane-like vortex formed over the southeastern part of Italy (Moscatello et al., 2008). The Mediterranean cyclone crossed Italy on 26 September 2006. Recently, the impact of the ET of Hurricane Hanna (2008) on the formation of a Mediterranean cyclone was investigated by Grams et al. (2011). The authors found that the ET of Hanna influenced the formation process by modifying the formation of a upper level PV streamer.

To investigate if the ET of Helene affected the Mediterranean cyclone, we target SVs on the Mediterranean cyclone. The optimisation time for the calculations is 60 hours. The linear evolution (integrated with the tangent linear model) of the SV perturbations is depicted in Figure 3.18. At the initial time, 24 September 2006 00 UTC, the SVs indicate clearly that the forecast over Italy is sensitive to the circulation of Ex-Helene (indicated by the red arrow) and also the jet region upstream of Ex-Helene (Fig. 3.18a). These features are associated with the largest vertically integrated total energy values. Other local maxima of the vertically integrated total energy exist over Northwest Africa and to the Southwest of Ireland. During the first 12 hours of the optimization interval strong perturbation growth takes place within the jet region north of Ex-Helene and within the ET system itself (Fig. 3.18b). At this time Helene's outflow advects low PV air into the downstream ridge (see Sect. 3.2). The perturbation energy propagates downstream into the ridge and then further downstream, affecting the PV streamer over Europe (Fig. 3.18c, d, e and f). From the total energy maxima of the SVs at the final time it is apparent that modifying the PV streamer causes large perturbation growth within the target region over the Mediterranean cyclone. At final time the ET system is affected also as indicated by the local total energy maximum at Ex-Helene's position. Therefore the SV analysis shows that the PV streamer, the Mediterranean cyclone and Ex-Helene are dynamically linked (Fig. 3.18f).

For assessing Helene's the downstream impact, high resolution is important to properly account for processes associated with the Ex-Hurricane. At low resolution (TL95), no clear maximum is associated with Ex-Helene at the initial time

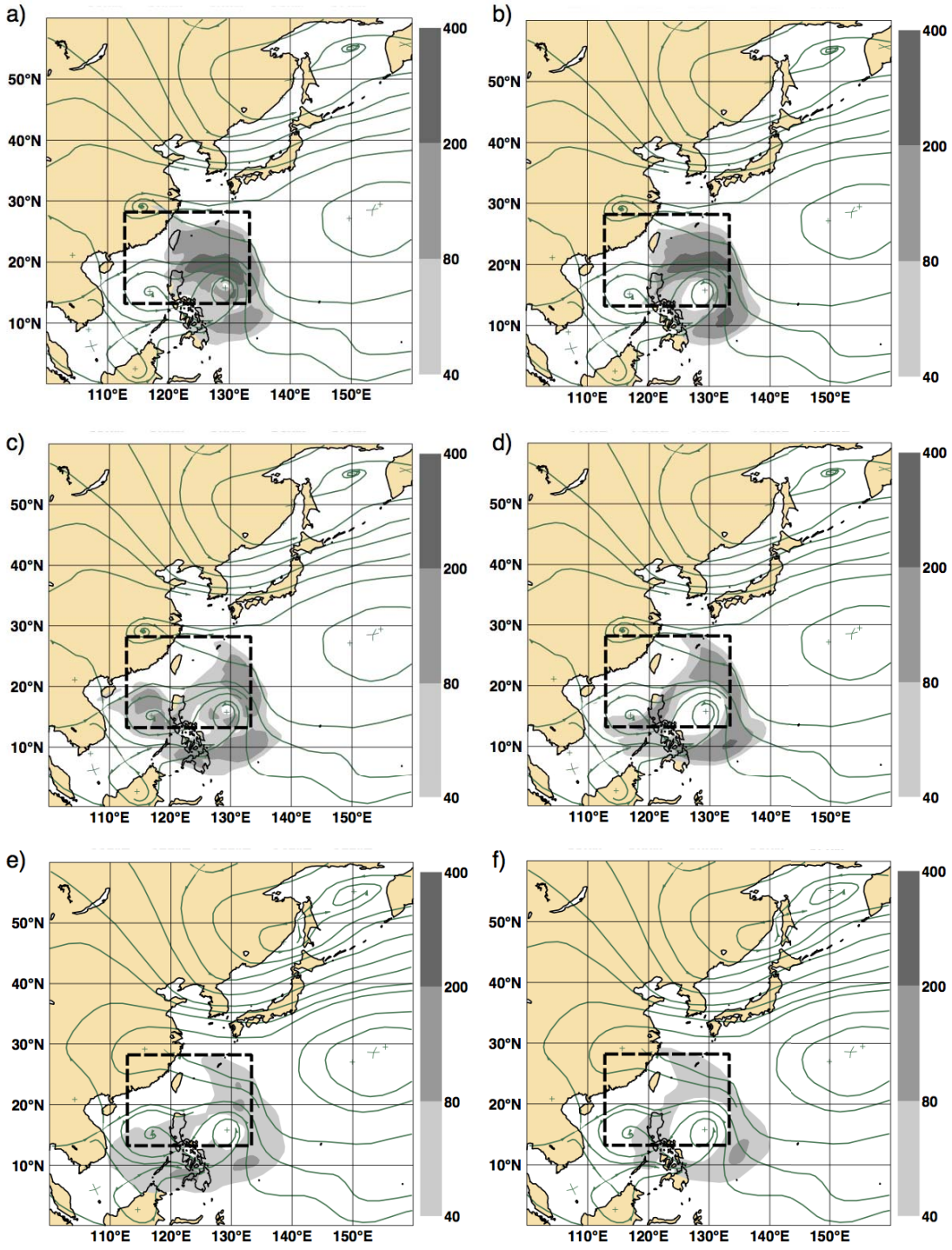

Figure 3.17: As 3.16 but for Typhoon Jangmi (26 September 2008 00 UTC); a) TL255 moist SVs, b) TL255 dry SVs, c) TL255 moist SVs optimized below 500 hPa, d) TL255 dry SVs optimized below 500 hPa, e) TL95 moist SVs optimized below 500 hPa, f) TL95 dry SVs optimized below 500 hPa.

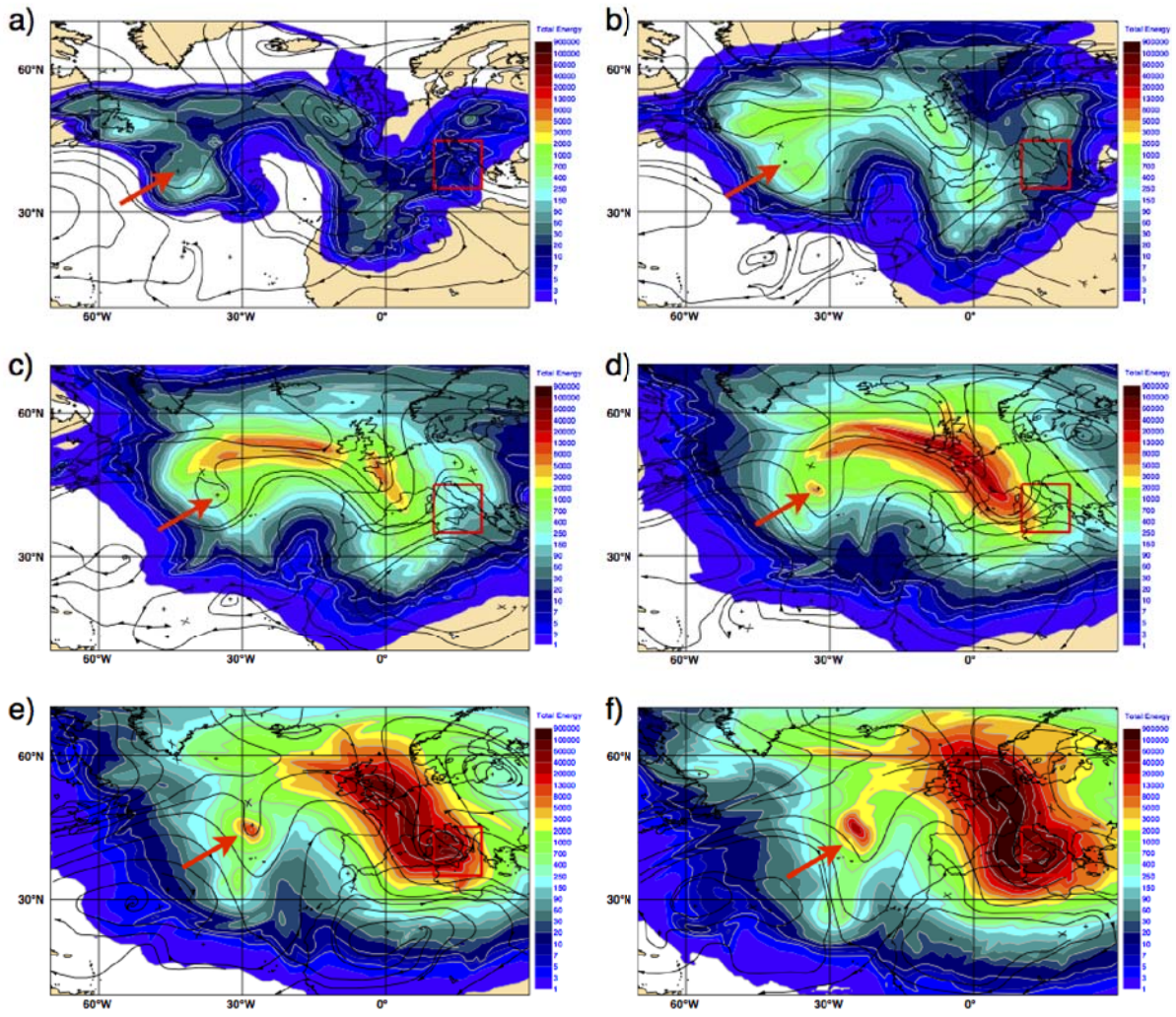

Figure 3.18: Streamlines of trajectory at 500 hPa and vertically integrated total energy (in $J\ kg^{-1}\ N\ m^{-2}$; colour shaded) of the leading 10 moist initial TL255 SVs from 24 September 2006 00 UTC. The SVs are targeted on the region where the Mediterranean cyclone forms (the optimization region is indicated by the red rectangle and the position of Ex-Helene by the red arrow). Depict is the linear evolution of the SV perturbations: a) 0 h, b) 12 h, c) 24 h, d) 36 h, e) 48 h and f) 60 h.

(Fig. 3.19a), only a tongue of high total energy values stretches into the flow associated with Ex-Helene. After 12 hours the perturbation growth within Ex-Hanna present for the TL255 SVs is missing at lower resolution (compare Fig. 3.18b and 3.19b). After 60 hours the largest total energy signal is associated with the PV streamer as in case of the TL255 SVs. However there is no distinct local total energy maximum associated with Ex-Helene (compare Fig. 3.18f and 3.19f). Therefore, the downstream impact of Helene is underestimated at lower resolution.

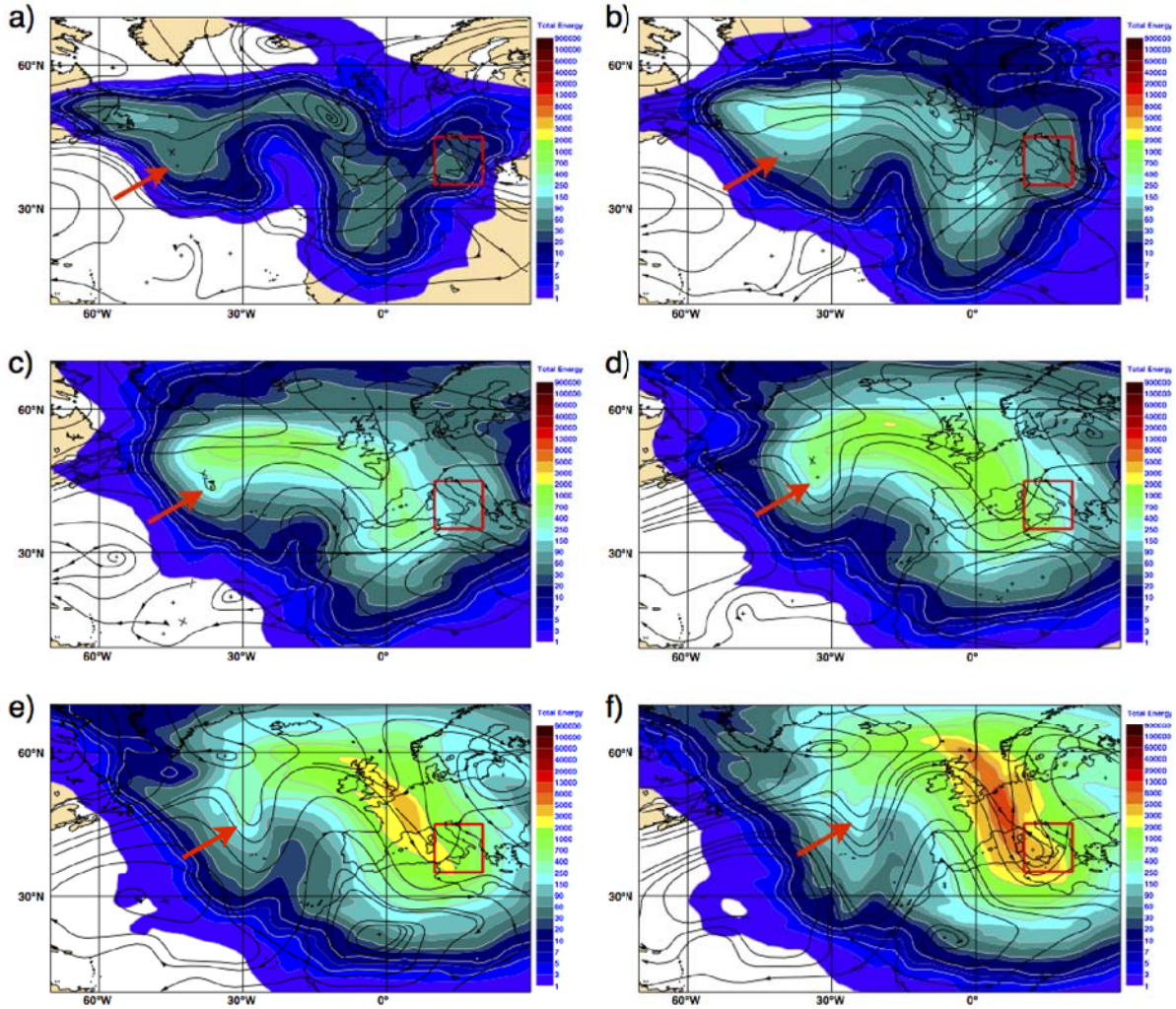

Figure 3.19: As 3.18 but for TL95 resolution

It is apparent that the high resolution moist SVs are capable of caputring the dynamical linkage between Ex-Helene, the midlatitude wave-guide and the Mediterranean cyclone. The SV formalism is a powerful tool to study the dynamics of such a complex interaction. It does not only indicate which features of the flow have an

impact on the predictability of a specific weather system but in addition also allows to quantify the respective importance.

3.9 Summary

In this part of the study we investigated the SV characteristics for Hurricane Helene (2006). Our results show that if the resolution of the SV calculation is increased or diabatic effects are accounted for, more of the SV structures are associated directly with the TC in comparison to other flow features. Also, more small scale structure occurs and the growth of the SVs is enhanced. This is consistent with previous studies that investigated either the resolution dependence of dry SVs (Komori and Kadowaki, 2010), or the sensitivity of SV calculations to diabatic effects with fixed resolution (Peng and Reynolds 2006, Kim and Jung 2009a),

We have shown that in the vicinity of a TC moist SVs are more sensitive to resolution changes than dry SVs, and that both high resolution and diabatic effects are needed within the SV calculations to properly account for growth associated with processes within Helene's core. Furthermore, we could explain the mechanisms that lead to the enhanced perturbation growth within Helene's core in the presence of diabatic effects. We demonstrated that, if calculated with sufficient resolution, the SVs are able to identify TCs as one of the most uncertain systems in the tropics. Therefore, the need for targeting the SV computation around the vicinity of the TC disappears at sufficiently high spatial resolution. In the context of ensemble forecasting this yields benefits, since it opens up the possibility of including SVs targeted on the whole tropics into the EPS instead of targeting individual TCs.

The SVs associated with Helene possess a three-dimensional structure with significant horizontal and vertical tilt. The energy flow analysis by Kwon and Frank (2008) indicates that the SVs exploit mechanisms associated with baroclinic and barotropic energy conversion for their growth. This is consistent with the results of Yamaguchi and Majumdar (2010), who analysed ECMWF ensemble perturbations generated from low resolution (T42) SVs optimized below 500 hPa. In addition, we show that spatial resolution and including / neglecting diabatic effects significantly influences both the contributions of the barotropic and baroclinic processes to the growth of the SVs and the regions where the growth occurs. In the vicinity of Helene, TL255 dry SVs show barotropic growth over the full depth of the troposphere, associated with transient growth and barotropic instability in the outer core region

of the TC. Baroclinic growth dominates at upper levels and extends horizontally from near the core to outer regions. If moist processes are accounted for, baroclinic growth is enhanced and the SVs exploit new processes closer to the center of the TC. The TL255 moist SVs possess a large amplitude within the TC, close to regions of maximum vertical shear (around 300 hPa) and tend also to be located within regions where the conditions for CSI are fulfilled. This leads to a stronger modification of the TC outflow, highlighting the importance of moist effects for the coupling between outflow and core of the TC.

If used to initialise EPS forecasts, the higher resolution moist SVs produce a larger wind spread within and near the TC and also in the upper troposphere, as a result of modifications to the outflow of the TC. This leads to an increased downstream effect of the TC, that influences the tropics during recurvature and the midlatitudes during ET. The TL255 moist SVs modify the track (except during the early tropical phase) and in particular the intensity of Helene more strongly than dry and lower resolution SVs. When the SVs are included as initial perturbations in the nonlinear model, the growth of the higher-resolution SVs is less linear than its coarser-resolution counterpart. The same is true for the inclusion of diabatic effects. The differences in linearity between moist and dry SVs are small at low resolution (T42) but become large if the resolution is increased. For TL255 moist SVs the initial amplitude has to be decreased for their growth to remain closer to the linear regime.

SV calculations for selected initialization dates for Typhoon Jangmi (2008) and Sinlaku (2008) indicate that the results derived for Hurricane Helene have general relevance. Furthermore we show that high resolution SVs capture the downstream impact of Helene's ET and enable us to quantify the importance of the ET System for the predictability of an intense Mediterranean cyclone.

4 Impact of different perturbation methods used in the ECMWF ensemble prediction system on tropical cyclone forecasts

The respective impact of initial condition perturbations and perturbations introduced by the stochastically perturbed parametrisation tendency scheme within the EPS of ECMWF in case of TCs have been investigated in the past by Puri et al. (2001) and, with a focus on the extratropical transition of TCs, by Anwender et al. (2010). In Puri et al. (2001) the authors found clear differences between the impact of the SV ensemble perturbations and the perturbations by stochastically perturbed parametrisation tendency scheme (see Sect. 2.4.5). In contrast, in the study of Anwender et al. (2010) there was no such distinction possible. Here, both perturbation methods caused significant TC track and intensity spread. Both studies investigated only a very limited number of cases. Furthermore, since these studies, the operational configuration of the ECMWF EPS and the perturbation methods have been altered considerably (Buizza et al. 2008, Palmer et al. 2009). Therefore, it is of interest to quantify the impact of the different methods on the forecasts of TCs and analyse their importance for TC track and intensity spread. As stated in the introduction (Chapter 1), this knowledge is important for ensemble design as well as for predictability studies in which ensemble methods are applied to study the dynamics of TCs (e.g. Veren et al., 2009, Keller et al., 2011). Furthermore, this knowledge is useful in order to compare the impact of different perturbation methods within the ensemble forecasts of different centers.

In our study, we focus on the structure and growth of the perturbations generated by the different methods and on how they influence the ensemble spread in the ECMWF EPS during TC events. A description of the different perturbation methods for ensemble forecasting is given in Section 2.4. In Section 4.1 we describe the set up of our experiments. The growth of the perturbations and the time evolution of their spatial structure is investigated in Section 4.2. The impact of the different methods

on the ensemble spread is analysed in Section 4.3. Finally, we give a summary and discuss our results in Section 4.4.

4.1 Experiments

For this study, 5 different ensemble setups (experiments) are used in order to isolate the impact of the different perturbation methods on the forecast of TCs. The setup of the different perturbation methods used in this study corresponds to the configuration of the operational EPS of ECMWF implemented in November 2010. All experiments have a spatial resolution of TL639 ($\approx$ 32 km), 62 vertical levels and consist of one unperturbed control forecast (thus identical for all experiments) and 20 perturbed forecasts. The 2008 operational deterministic analyses are used to define the starting point for the EPS initial conditions. The analyses in 2008 were generated using a TL799 ($\approx$ 25 km) outer loop and three inner loops with TL95, TL159 and TL255 ($\approx$ 80 km) resolution. The ensemble members of the different experiments are perturbed as follows.

- In experiment **SVINI** initial perturbations are generated from initial SVs, as described in Section 2.4.1.
- In experiment **EDA** initial perturbations are generated from the ensemble of data assimilations.
- In experiment **SKEB** perturbations are generated by the stochastic kinetic energy backscatter scheme.
- In experiment **SPPT3** perturbations are generated by the stochastically perturbed parametrisation tendency scheme
- In experiment **ALL**, all four methods are applied to generate perturbations. In contrast to the other experiments, 50 ensemble members are calculated. This configuration corresponds to the setup operational since November 2010. For parts of our study, we only use 20 of the 50 members so that the differences between the experiments can be attributed to the perturbation method only. The 20-member ensemble will be referred to by ALL, while ALL50 refers to the full 50-member ensemble.

The five experiments were run from 14 August to 4 October 2008. Given the significant computational costs of the experiments it was not possible to run the

experiments daily. Thus the forecasts were started every 48 hours at 00 UTC. This corresponds to 135 global ensemble forecasts (equivalent to 3645 individual forecasts). The forecast time is 10 days. Model level data was archived for the first three days of the forecasts. To save storage space, the model level data was archived at reduced resolution (TL255). The ensemble of analyses was run from 4 August to 5 October 2008 to generate the EDA perturbations (equivalent to 1386 individual 4D-Var analyses). The EDA had enough time to spin up in the first 10 days, which were not used in the ensemble forecasts.

In total, we consider 13 TCs from 2008 for this study (see Tab. 4.1). An ensemble forecast for an individual TC is only included in this study if the TC is detected in the control forecast at the initial time. This results in 38 EPS TC forecasts for each experiment. The tracker described by Vitart et al. (1997) and Vitart et al. (2003) is used to track the TCs . The criterion for a TC to be detected are the existence of a local maximum of vorticity with magnitude larger than $3.5 \times 10^{-5}\ s^{-1}$ and that a warm core exist (see Vitart et al. 1997 for a detailed description of the tracking algorithm). The center of the TC is defined as the minimum of the mean sea level pressure that is closest to the 850 hPa vorticity maximum. The best track data used to assess the ensemble performance is taken from the International Best Track Archive for Climate Stewardship (IBTrACS - Knapp et al. 2010).

4.2 Perturbation growth and structure

The distribution of the mean total energy of the ensemble perturbations generated with the different perturbation methods differs within the TC over time. To investigate the growth of the perturbations, the total energy of the perturbations generated by the different methods is evaluated in the vicinity of the TCs. To analyse the structure of the perturbations we assess the projection of the SVINI perturbations onto the EDA, SKEB and SPPT3 perturbations. Furthermore, we generate composites of their mean azimuthally integrated perturbation total energy. In the following the perturbations $\mathbf{x}(t)$ are defined as

$$\mathbf{x}_i(t) = \mathbf{p}_i(t) - \mathbf{c}(t), \quad i = 1, \ldots, 20 \tag{4.1}$$

with the unperturbed control forecast $\mathbf{c}(t)$ and the perturbed forecast $\mathbf{p}_i(t)$.

Name	Category	Basin	Lifespan	Nr. of Forecasts
Fay	Tropical Storm	Atlantic	15 August - 26 August	4
Gustav	Hurricane	Atlantic	25 August - 4 September	4
Hanna	Hurricane	Atlantic	28 August - 7 September	5
Ike	Hurricane	Atlantic	1 September - 14 September	6
Josephine	Tropical Storm	Atlantic	2 September - 6 September	2
Kyle	Hurricane	Atlantic	25 September - 29 September	2
Laura	Tropical Storm	Atlantic	29 September - 1 October	1
Nuri	Typhoon	West Pacific	17 August - 23 August	2
Sinlaku	Typhoon	West Pacific	8 September - 21 September	5
Hagupit	Typhoon	West Pacific	19 September - 25 September	3
Jangmi	Typhoon	West Pacific	24 September - 1 October	2
Mekkhala	Tropical Storm	West Pacific	29 September - 30 September	1
Higos	Tropical Storm	West Pacific	2 October - 3 October	1

Table 4.1: Name, category and lifespan of the TCs considered in this study.

4.2.1 Mean growth of perturbations

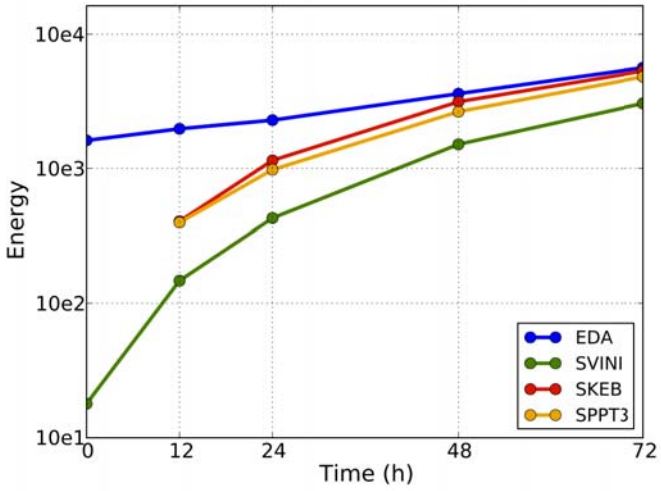

Figure 4.1: Mean perturbation total energy (integrated and area weighted) within a $20° \times 20°$ box centered on the forecast positions of the TCs. The scaling of the Y-axis is logarithmic.

On average, the SVs exhibit the largest growth rate within a $20° \times 20°$ box around the TCs followed by the stochastic representation of model uncertainty (Fig. 4.1). The box is centered on the forecast positions of the TCs from the control forecasts. The perturbation magnitude is measured by the total energy norm (Eqn. 2.5). Since the stochastic tendency perturbation methods only introduce perturbations within the forecast time, they possess no amplitude at initial time. Initially, the mean total energy of the EDA perturbations is largest. The EDA perturbations dominate within the first 24 hours of the forecast, while after 48 hours the mean total energy of the perturbations in the SKEB and SPPT3 experiments is comparable to the mean total energy of the EDA perturbations.

The EDA perturbations grow approximately exponentially, even though they grow somewhat slower during the first 24 hours of the forecasts than afterwards. The perturbations of the other methods grow much faster than the EDA perturbations initially. The growth rates decrease with increasing forecast lead time, and after 48 hours the growth rates becomes comparable in magnitude to the growth rate of the EDA perturbations. The largest mean total energy values are associated with the EDA perturbations after 72 hours, followed by the SKEB and SPPT3 perturbations. The smallest mean total energy values at this time are associated with the SVINI perturbations.

4.2.2 Projection of SVINI perturbations

While the EDA and stochastic perturbation methods aim to represent the actual uncertainty associated with a forecast, the SV formalism is designed to identify the fastest growing modes of the flow. It is assumed that errors arising from analysis uncertainty that project onto the leading SVs will dominate the forecast uncertainty after some time in the future (see Sect. 2.4.1). For ensemble design, it is of interest to investigate how similar the resulting perturbations of the different schemes are and wether they succeed in exciting the fastest growing modes of the flow. To asses this issue, we project the perturbations generated from the SVs onto the perturbations of the other methods, since the SVs are designed to identify these fastest growing modes. The projection is a rather strong test, because it takes into account the perturbation structure rather than just comparing regions where perturbations grow.

To perform the projection, the perturbations are localized around the TC. For this purpose, a box is fitted around the forecast positions of the TC in the ensemble members of the ALL experiment. Then the box is enlarged by 5° to the North, South, East and West to include the TC completely. For the projection we use model level data with TL255 resolution. The part of an SVINI perturbation $\mathbf{x}_i^{SV}$ that is orthogonal to the subspace of the state space spanned by the perturbations generated by another method is given by:

$$\mathbf{r}_i^{SV} = \mathbf{x}_i^{SV} - \sum_j^N \langle \mathbf{x}_i^{SV}, \mathbf{y}_j \rangle \mathbf{y}_j \quad i = 1 \dots N \tag{4.2}$$

Here N denotes the number of ensemble members and $\langle , \rangle$ denotes an inner product. The perturbations $\mathbf{x}_i^{SV}$ are defined as described in Section 4.2.1. The vectors $\mathbf{y}_j$ are an orthonormal base of the subspace spanned by the perturbations of an ensemble initialised with one of the other methods (EDA, SKEB, SPPT3) and $\mathbf{r}_i^{SV}$ denotes the residuum vectors. The total energy norm (Eqn. 2.5) is used for the inner product. The norm was confined below 500 hPa, since the SVs are optimized below this level (see Sect. 2.4.1). The mean explained fraction of the perturbation energy for a single (ensemble) forecast is given by

$$\alpha_{SV} = \frac{1}{N} \sum_i^N \left(1 - \frac{\langle \mathbf{r}_i^{SV}, \mathbf{r}_i^{SV} \rangle}{\langle \mathbf{x}_i^{SV}, \mathbf{x}_i^{SV} \rangle} \right) \tag{4.3}$$

Initially only a very small amount of the total energy of the SVINI perturbations,

approximately 11%, can be explained by the EDA perturbations (Tab. 4.2). This indicates that the structures are quite different at the initial time. After 12 hours, the average projection of the SVINI perturbations onto the EDA perturbations is largest. Close to 40% of the SVINI perturbations can be explained by the perturbations of the EDA experiment. The second highest projection is associated with the SPPT3 perturbations, while the SVINI perturbations project most weakly onto the SKEB perturbations. After 48 hours, the SPPT3 perturbations catch up to the other perturbation methods and now on average around 60% of the Energy of the SVINI perturbations can be explained by the other methods. It is apparent that the

Exp.	0 h	12 h	24 h	48 h	72 h
EDA	10.8%	39.7%	53.3%	64.0%	66.2%
SKEB	-	30.0%	47.6%	58.8%	61.9%
SPPT	-	37.2%	50.1%	60.5%	64.7%

Table 4.2: Mean percentage of the perturbation total energy of the SVINI experiment explained by the perturbations of the different experiments. The values are averaged over all ensemble forecasts.

EDA perturbations and the perturbations from the stochastic tendency perturbation schemes excite growing modes associated with the TCs successfully and, therefore, are useful to generate spread within the ensemble.

4.2.3 Composite Structure

We create composites of the azimuthally integrated perturbation total energy in order to analyse in more detail the structure of the perturbations generated by the different methods. The composites are averaged over all TCs and all ensemble members. For the composites, the fields are centered on the position of the TC in the control forecast on each date and at each forecast time. The azimuthally integrated perturbation total energy indicates at what distance and height the energy of the perturbations is located with respect to the TC. From previous studies it is known that structures in the outer TC core can be important for TC track and intensity forecasts (e.g. Fiorino and Elsberry, 1989, Peng et al., 2009, Yamaguchi et al., 2011, Lang et al., 2011). We integrate the perturbation total energy instead of taking the azimuthal average to better highlight these structures in the outer core region of the TC.

Figure 4.2 shows the composites of the EDA (Fig. 4.2a) and SVINI (Fig. 4.2b)

perturbations at the initialization time of the forecasts. At this time most of the energy of the EDA perturbations is either located in the upper troposphere or associated with the TC core (Fig. 4.2a). In contrast, most of the structures of the SVINI perturbations are located in the mid to lower troposphere in the outer region of the TC (Fig. 4.2b). In addition the initial amplitude of the SVINI perturbations is much smaller (Buizza et al., 2008). It is apparent that the SVINI perturbations are very different from the EDA perturbations.

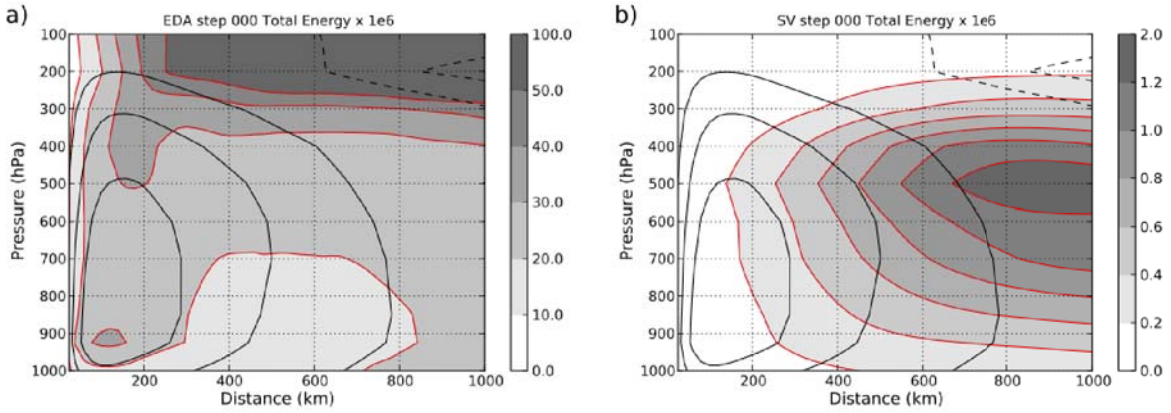

Figure 4.2: Composite of the mean azimuthally integrated total energy ($\times 10^6 J\ kg^{-1} m$; grey shading) of the EDA (a) and SVINI (b) perturbations at initialization time of the forecasts and azimuthal wind of control forecasts (black contours; contours are drawn at -10, -5, 5, 10, 15 and 25 $m\ s^{-1}$).

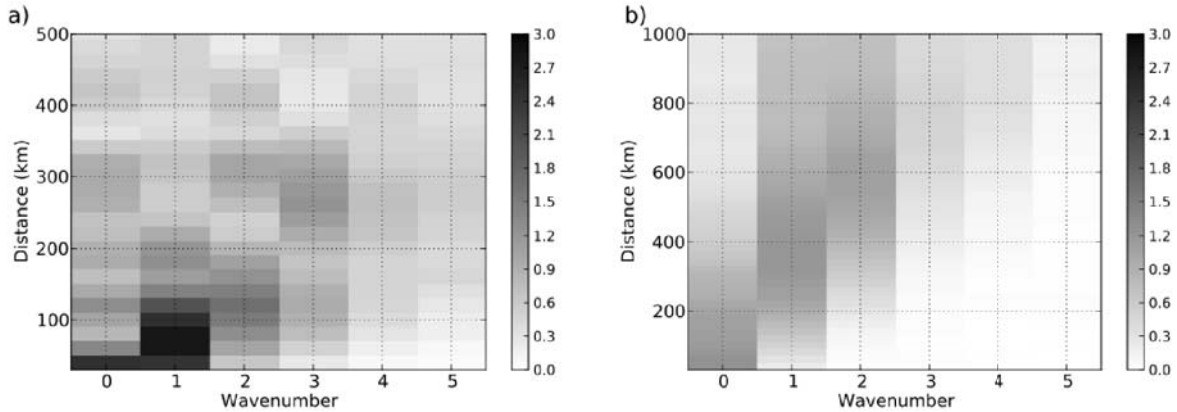

Figure 4.3: Decomposition of 700 hPa perturbation vorticity (s^{-1}) into azimuthal wavenumbers for a) EDA and b) SVINI perturbations. Depicted is the mean amplitude at initialization time as a function of wavenumber and radius, averaged over all forecasts. The amplitude of the SVINI perturbations is scaled by a factor of 20.

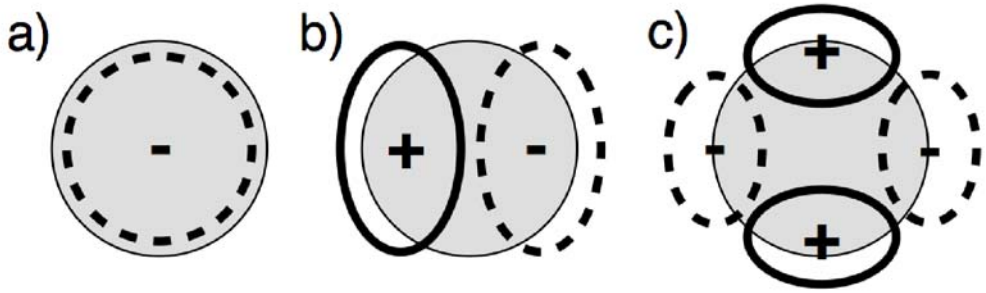

Figure 4.4: Schematics of perturbation patterns. Example for a wavenumber 0 (a), wavenumber 1 (b) and wavenumber 2 (c) perturbation. A wavenumber 0 pattern corresponds to an intensity change, a wavenumber 1 pattern to a displacement and wavenumber 2 pattern to a tilt or deformation of the TC.

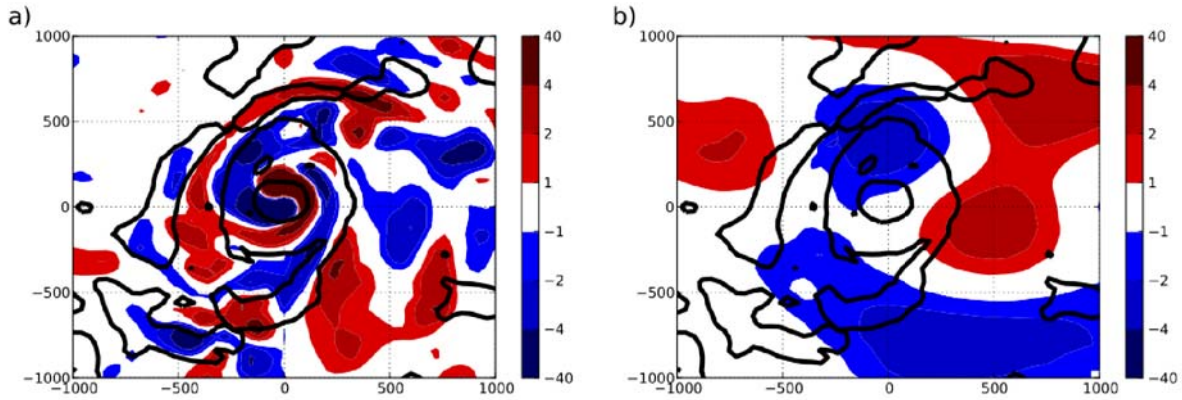

Figure 4.5: Perturbation vorticity ($\times 10^{-5}$ s^{-1}) of ensemble member 19 at 700 hPa for TC Sinlaku at initial time for the initialization date 00 UTC 11 September 2008 and vorticity of the control forecast (black contours; contours are drawn at 1 and 10 $\times 10^{-5}$ s^{-1}). EDA perturbation (a) and SVINI perturbation (b; the SVINI perturbation was scaled by a factor of 20).

An azimuthal Fourier analysis of the perturbation vorticity indicates that the EDA perturbations are dominated by a wavenumber 1 pattern on average (Fig. 4.3a). The wavenumber 1 pattern is associated with a displacement of the TC (see Fig. 4.4). There is also some amplitude of the perturbations associated with an intensity change (wavenumber 0), especially close to the center, and with a deformation of the TC (wavenumber 2). The SVINI perturbations on the other hand exhibit wavenumber 1 and 2 patterns some distance away from the TC center where most of their energy is concentrated (Fig. 4.3b).

In the following, we illustrate common features of the different perturbation methods using the randomly chosen ensemble member 19 from the forecast of Typhoon Sinlaku from 00 UTC 11 September 2008. Because the EDA perturbations tend to be associated with a displacement of the TC, their perturbation vorticity is dominated by a dipole structure within the TC. However, there are also structures to be seen that are associated with the TC environment (Fig. 4.5a). Figure 4.6 shows as an example the displacement of Typhoon Sinlaku within the EDA. The spatial distribution of the SVINI perturbations (Fig. 4.5b) is dominated by upshear tilted structures (Barkmeijer et al. 2001, Yamaguchi and Majumdar 2010, Lang et al. 2011). The upshear tilt of the SVINI perturbations is in contrast to the downshear tilted structures of the EDA perturbations (compare Fig. 4.5a and b). The EDA perturbations possess a significantly higher effective resolution than the SV perturbations, because they are generated by subtracting two high resolution 6-hour forecasts (see Sect. 2.4.2) As a result, the SVINI perturbations are more large scale than the EDA perturbations and, therefore, exhibit less small scale structures. This was also observed by Buizza et al. (2008) for global ensemble perturbations. The SVINI perturbations experience transient growth and grow because of baroclinic and barotropic processes (Yamaguchi and Majumdar 2010, Lang et al. 2011). The displacement pattern of the EDA perturbations, on the other hand, can directly shift the TC relative to the background flow that steers the TC and thereby result in a track deviation.

After 12 hours, the EDA perturbations are associated with the TC inner core and upper level outflow (Fig. 4.7a). Thus the principal patterns remain for the EDA perturbations even though their amplitude grows. At upper levels the perturbations extend further away from the TC core than at lower levels and the impact on the outflow of the TC is visible (Fig. 4.8a and b). Near the top of the TC the air flows out of the storm (Emanuel, 2003). The circulation is still cyclonic close to the cen-

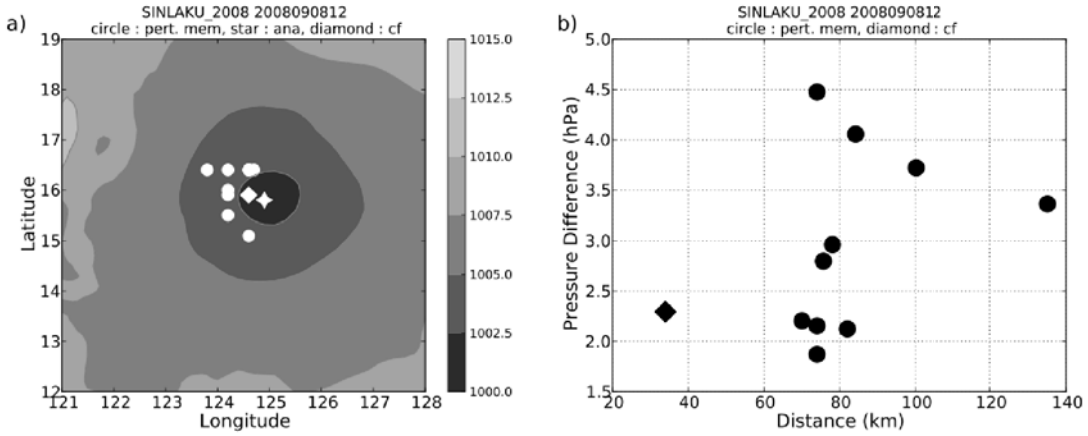

Figure 4.6: a) Mean sea level pressure of Sinlaku (8. September 2008 12 TC) from deterministic analysis (grey shading; in hPa) and minimum of mean sea level pressure of deterministic analysis (star), control analysis (diamond) and perturbed analyses (circles). b) Pressure difference and displacement of perturbed analyses (circle) and control analysis (diamond) relative to deterministic analysis.

ter of the TC but it becomes anticyclonic at larger radii (Chan and Kepert, 2010). The outflow of a TC is much larger scale, up to 3000 km, than the cyclonic vortex (Merrill, 1988). Hence perturbations associated with the TC outflow also possess a larger spatial extent and this results in a strong signal in the composites of the azimuthally integrated perturbation total energy.

The SVINI perturbations also impact the location of the TC after 12 hours, but their amplitude (measured in total energy) is still much smaller, especially in the upper troposphere since they are optimized below 500 hPa (Fig. 4.7b). Therefore, their growth is focused below that level. Their maximum is located in the TC core region where they also tend to develop a dipole structure and thus a displacement pattern. The maximum of the mean azimuthally integrated energy of the SKEB perturbations is located at some distance from the TC center. In the composite, the region of high values extends over the whole depth of the troposphere (Fig. 4.7c). Another local maximum is located in the TC core region. The strongest signal within the azimuthally integrated total energy of the SPPT3 perturbations is located at upper levels. Here the tendencies have the strongest impact. A further local maximum is located within the core region of the TC (Fig. 4.7d).

After 12 hours forecast time, the SKEB perturbations exhibit a broader distribution than the SPPT3 perturbations with more structure outside of the TC core on average (Fig. 4.9). Both perturbations show dipole like structures in the TC core region. While the SPPT3 perturbation also possesses amplitude outside of the core,

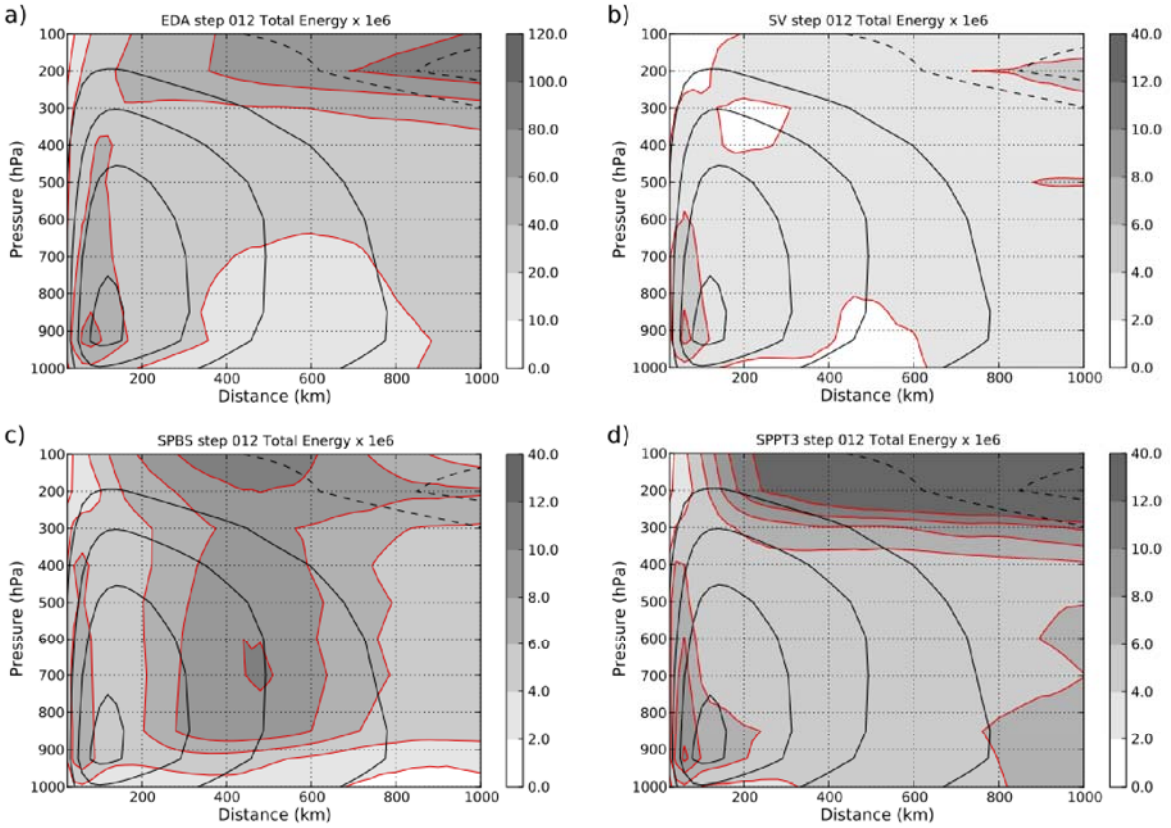

Figure 4.7: Composite of the mean azimuthally integrated total energy ($\times 10^6 J\ kg^{-1} m$; grey shading) of the EDA (a), SVINI (b), SKEB (c) and SPPT3 (d) perturbations after 12 hours forecast time and azimuthal wind of control forecasts (black contours; contours are drawn at -10, -5, 5, 10, 15 and 25 $m\ s^{-1}$).

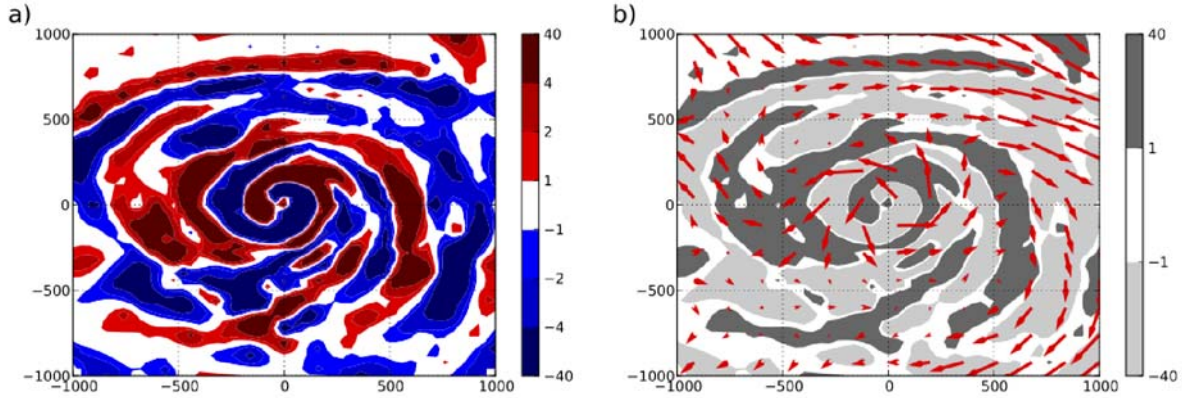

Figure 4.8: Perturbation vorticity ($\times 10^{-5}\ s^{-1}$) of ensemble member 19 at 200 hPa for TC Sinlaku after 12 hours for the initialization date 00 UTC 11 September 2008. EDA perturbation (a) and wind vectors of control forecast and perturbation vorticity (b).

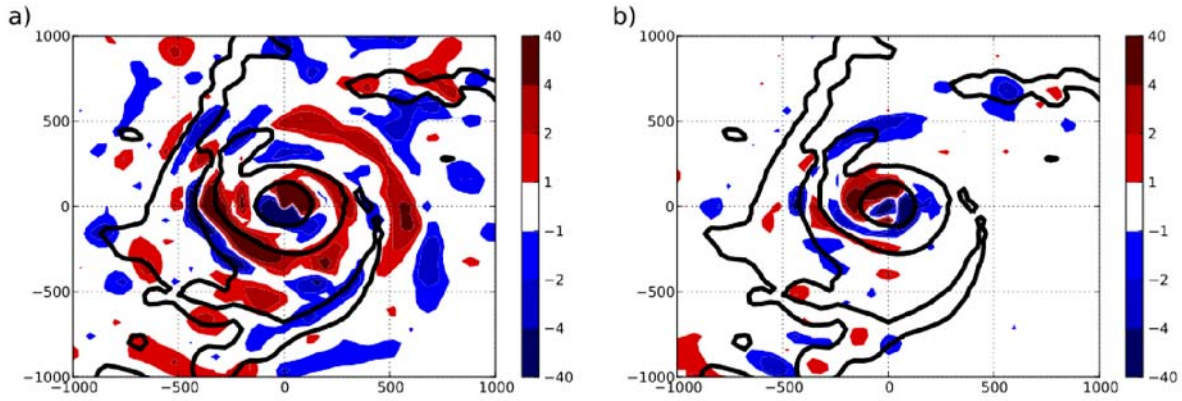

Figure 4.9: Perturbation vorticity ($\times 10^{-5}$ s^{-1}) of ensemble member 19 at 700 hPa for TC Sinlaku after 12 hours for the initialization date 00 UTC 11 September 2008 and vorticity of the control forecast (black contours; contours are drawn at 1 and 10 $\times 10^{-5}$ s^{-1}). SKEB perturbation (a) and SPPT3 perturbation (b).

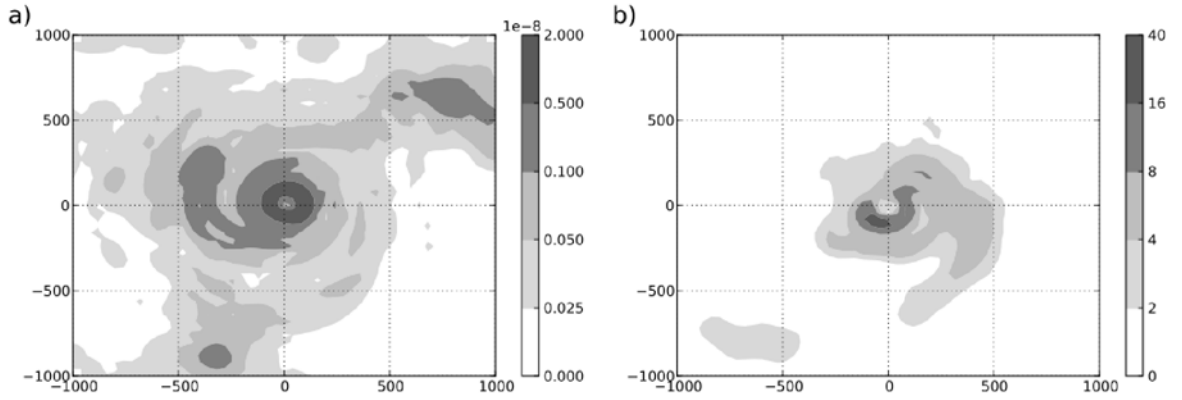

Figure 4.10: (a) Absolute values of vertically averaged radial gradient of relative vorticity (m^{-1} s^{-1}) after 12 hours forecast time for Typhoon Sinlaku. Forecast is initialized at 00 UTC 11 September 2008. (b) Vertically averaged YOTC temperature tendency (in K; 3 hours accumulated) from cloud and convection scheme for Sinlaku from forecast initialized at 12 UTC 11 September 2008. Fields are averaged between 850 and 300 hPa.

the structure of the SKEB perturbation is distributed more symmetrically around the TC. These common properties result in the differences of the composites of the azimuthally integrated total energy for the different schemes. As stated in Section 2.4.3 and 2.4.4 both schemes are active in regions of strong updrafts and where convection takes place. In addition, the stochastic forcing of the SKEB scheme also depends on the magnitude of the vorticity gradient, which is used to estimate the numerical dissipation (see Sect. 2.4.3).

The SPPT3 scheme generates perturbations by directly modifying the tendencies from the parametrisation schemes (see Sect. 2.4.4). To estimate the structure and amplitude of the model tendencies for a TC, we use the tendencies from the ECMWF year of tropical convection data set (YOTC, 2011, Waliser et al., 2011). During the YOTC period the tendencies from the parametrisation schemes of the forecast model of ECMWF were archived every 3 hours for 36 hours. The resolution of the YOTC calculations is slightly higher (TL799; $\approx$ 25km) than the resolution of our ensemble forecasts. However, we assume that the properties (location and amplitude) are qualitatively similar to the tendencies of our forecasts. For TCs, the most important tendencies from the parametrisation schemes are the ones from the cloud scheme and the convection scheme. We examined tendencies from the cloud scheme and the convection scheme for the first 3 hours of the forecasts for all the TCs in 2008. It is a common feature of these tendencies that they exhibit maximum values within the TC core region and show strong asymmetries in the TC outer region (see Fig. 4.10b for an example for Typhoon Sinlaku). The magnitude of the radial vorticity gradient is largest within the TC core but frequently possesses amplitude some distance away from the TC center (Fig. 4.10a). In addition, the radial vorticity gradient tends to be less localized than the parametrisation tendencies (compare Fig. 4.10a and b). Since the forcing by the SKEB scheme depends on spatial properties of both fields, which can also complement each other, the SKEB perturbations are less localized than the SPPT3 perturbations on average. However, as stated earlier, the SPPT3 scheme does introduce perturbations in the outer region of the TC, but in a less symmetric way than the SKEB scheme. Therefore, they do not show up as prominently within the composites as in case of the SKEB scheme.

After 48 hours similar total energy patterns emerge for the different perturbation methods (Fig. 4.11). The EDA perturbations still possess the largest amplitude (Fig. 4.11a), followed by the SKEB and SPPT3 perturbations (Fig. 4.11b and c). A local maximum is seen within the TC inner core for all experiments. The total

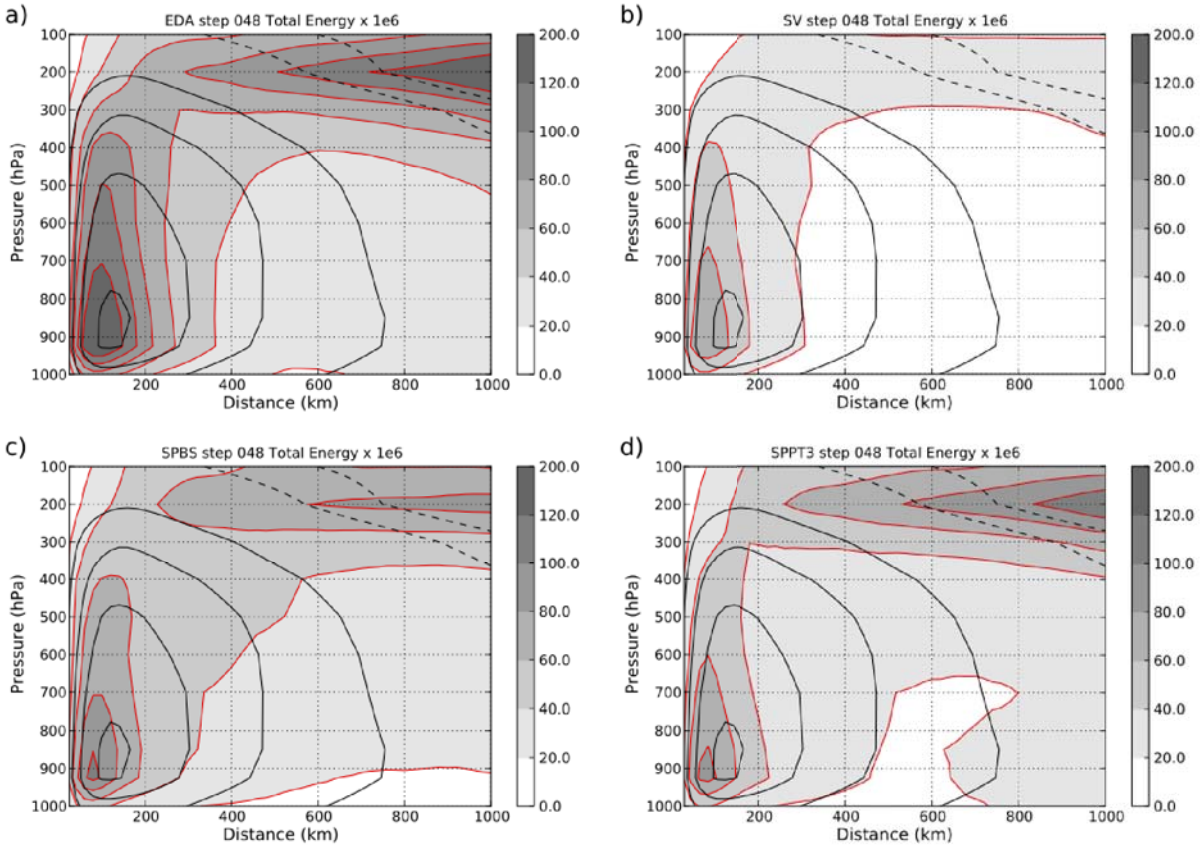

Figure 4.11: Composite of the mean azimuthally integrated total energy ($\times 10^6 J\ kg^{-1} m$; grey shading) of the EDA (a), SVINI (b), SKEB (c) and SPPT3 (d) perturbations after 48 hours forecast time and azimuthal wind of control forecasts (black contours; contours are drawn at -10, -5, 5, 10, 15 and 25 $m\ s^{-1}$).

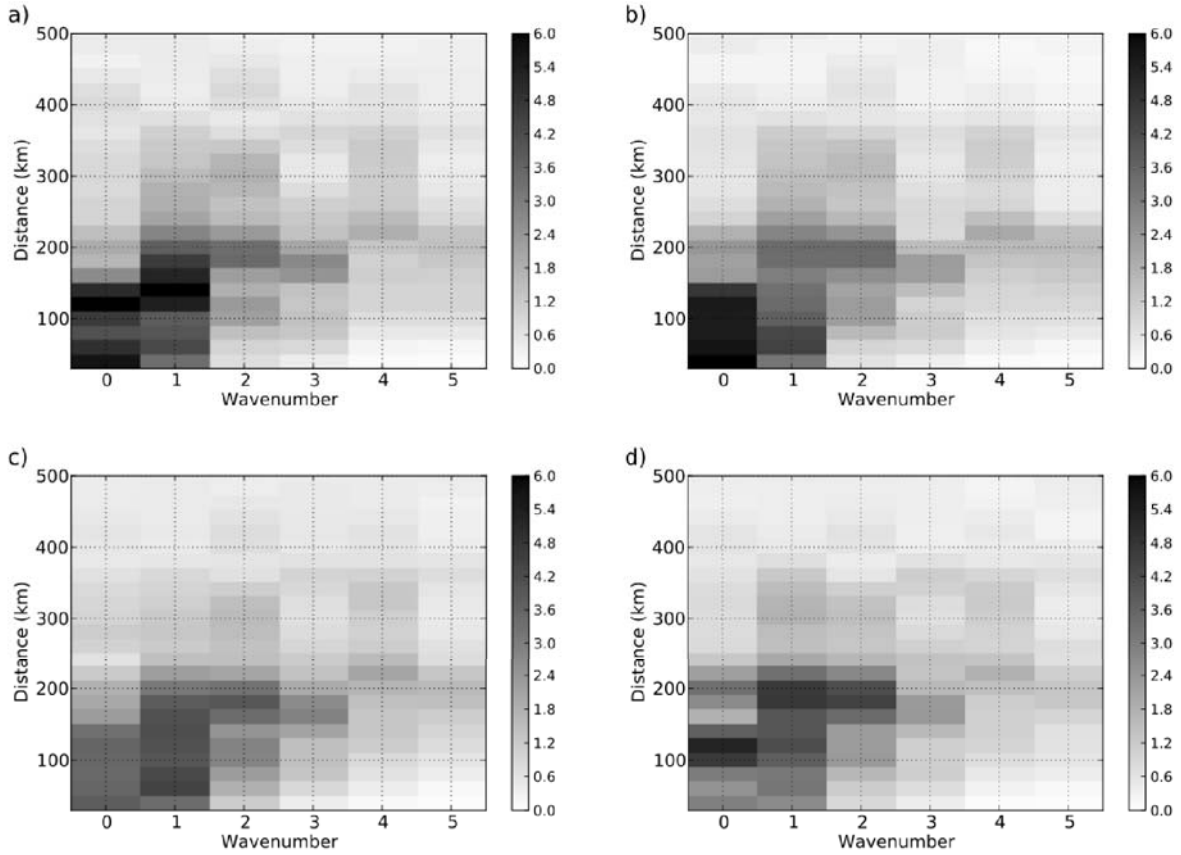

Figure 4.12: As Figure 4.3 but after 48 hours forecast time for a) EDA, b) SVINI, c) SKEB and d) SPPT3 perturbations.

energy patterns of the different experiments now resemble the pattern of the EDA experiment. Within the TC they correspond to a displacement and / or intensity change of the TC (Fig. 4.12). Wavenumber 2 structures become increasingly important at radii larger than 100 km. In contrast to the perturbations by the methods designed to represent initial condition uncertainty, the SKEB and SPPT3 schemes always reintroduce new perturbations during the forecast time. However, the forecast perturbation structure from these methods is dominated by the displacement and intensification patterns for lead times of the order of 1-2 days.

4.3 Impact on ensemble forecasts

The various perturbation methods have a different impact on the ensemble spread of the position and the central pressure of the TCs. We follow the approach of Hamill et al. (2010) to calculate the mean spread of the experiments and only use a forecast if it is possible to identify the TC at least in 40% of the ensemble members at the respective forecast time. Hence, the number of forecasts used to calculate the ensemble spread of the experiments varies over time. The spread of the ensemble for a single TC ensemble forecast at a given forecast time is defined as (Hamill et al., 2010):

$$S_l(t) = \frac{\sum_{i=1}^{n} D_{l,i}}{n} \tag{4.4}$$

Here $D_{l,i}$ denotes the great circle distance of the ith ensemble member TC position to the ensemble-mean TC position. The total number of ensemble members used for the calculation is given by n. The mean spread of the ensemble is then:

$$\bar{S}(t) = \frac{\sum_{l=1}^{m} S_l(t)}{m} \tag{4.5}$$

Where m is the total number of ensemble forecasts. The spread of the TC central pressure is defined accordingly using the absolute pressure differences. The average error of the ensemble-mean is given by:

$$\bar{E}(t) = \frac{\sum_{l=1}^{m} E_l(t)}{m} \tag{4.6}$$

with the great circle distance between the ensemble-mean and the best track TC position E_l. To test for statistical significance, we calculate 95% confidence intervals

using the paired block bootstrap algorithm described by Hamill (1999) and Hamill et al. (2010). The different ensemble forecasts for one TC are not treated as independent but shuffled as a block to account for error correlations between consecutive initialization dates.

Of the four ensembles for which only one of the perturbation methods is applied, the EDA experiment exhibits the largest mean track spread within the first 5 days of the forecast (Fig. 4.13a). This is statistically significant for the first 4 days of the forecast in terms of the SVINI experiment (Fig. 4.14a) and over 5 days in case of the SKEB and SPPT3 experiment (Fig. 4.14b and c). The spread of the EDA experiment is considerable at initialization time, since the EDA perturbations are associated with a shift and intensification / weakening of the TC (see Sect. 4.2.3). The smallest mean track spread is associated with the SVINI experiment (Fig. 4.13a). However, this difference to the SKEB and SPPT3 experiments is only barely significant between forecast-day 3 and 4 and not significant for the rest of the forecast (Fig. 4.14d and e). The difference between the mean track spread of the SKEB and SPPT3 experiment is not significant over the whole 5 day forecast (Fig. 4.14f).

In terms of central pressure, the EDA experiment initially exhibits the largest mean spread (Fig. 4.13b). The difference of the mean central pressure spread between the EDA and SVINI experiment is statistically significant within the first 96 hours of the forecasts (Fig. 4.15a). The difference between the EDA and SKEB experiment is only statistically significant for 36 and between the EDA and SPPT3 experiment for 48 hours forecast time (Fig. 4.15b and c). The difference between the mean central pressure spread of the SVINI and SPPT3 experiment is only barely significant and between the SKEB and SPPT3 experiment not significant at all. As is to be expected, the ensemble using all four methods exhibits the largest spread in terms of both, TC track and TC central pressure (Fig. 4.13a).

There is a considerable case to case variability of the impact on the central pressure and track spread of the different perturbation methods. Some TC events generally support larger growth rates than others and in some cases one perturbation method has a large impact while others do not. At initialization time, the ensemble spread of the EDA experiment is largest in close to 100% of the cases (Fig. 4.16a and b). This value quickly decreases to 60% within 48 hours forecast time for TC track and central pressure. It decreases further afterwards. The SKEB experiment exhibits the second highest percentage of cases with the largest spread, but there are also some cases for which the spread of the SPPT3 or the SVINI experiment is largest. This emphasizes the result obtained in Section 4.2.1 for the perturbation growth measured

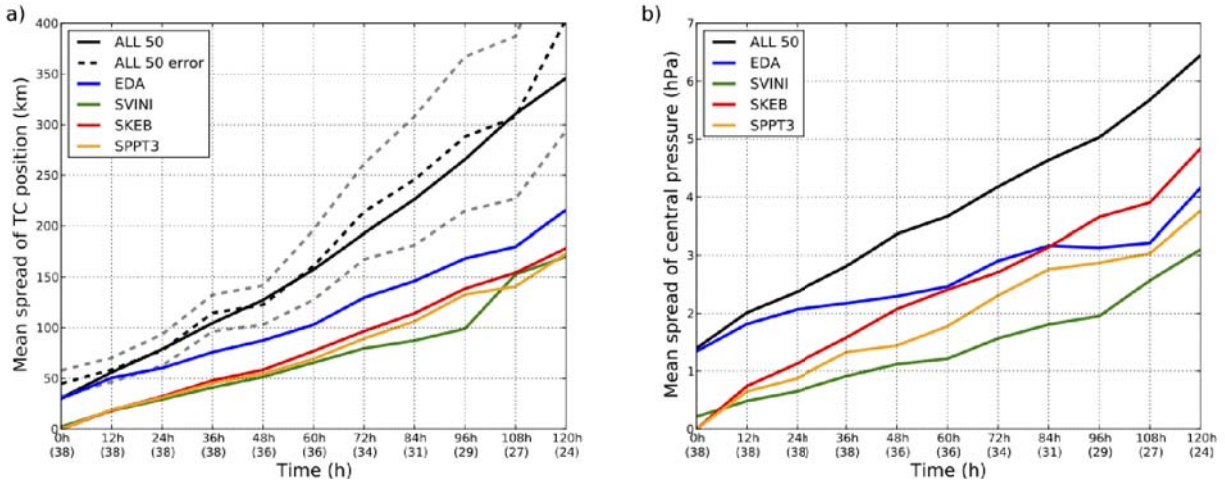

Figure 4.13: Mean ensemble spread of TC track (a) and central pressure (b) of the different ensembles. The dashed black line indicates the mean error of the ALL 50 ensemble-mean. The dashed grey lines indicate the 95% confidence interval of the difference between mean error and mean spread of the ALL 50 ensemble. Hence, if the black line lies within the range indicated by the grey dashed lines, the differences are not statistically significant. The numbers in parentheses indicate, how many forecasts were considered for the respective lead time.

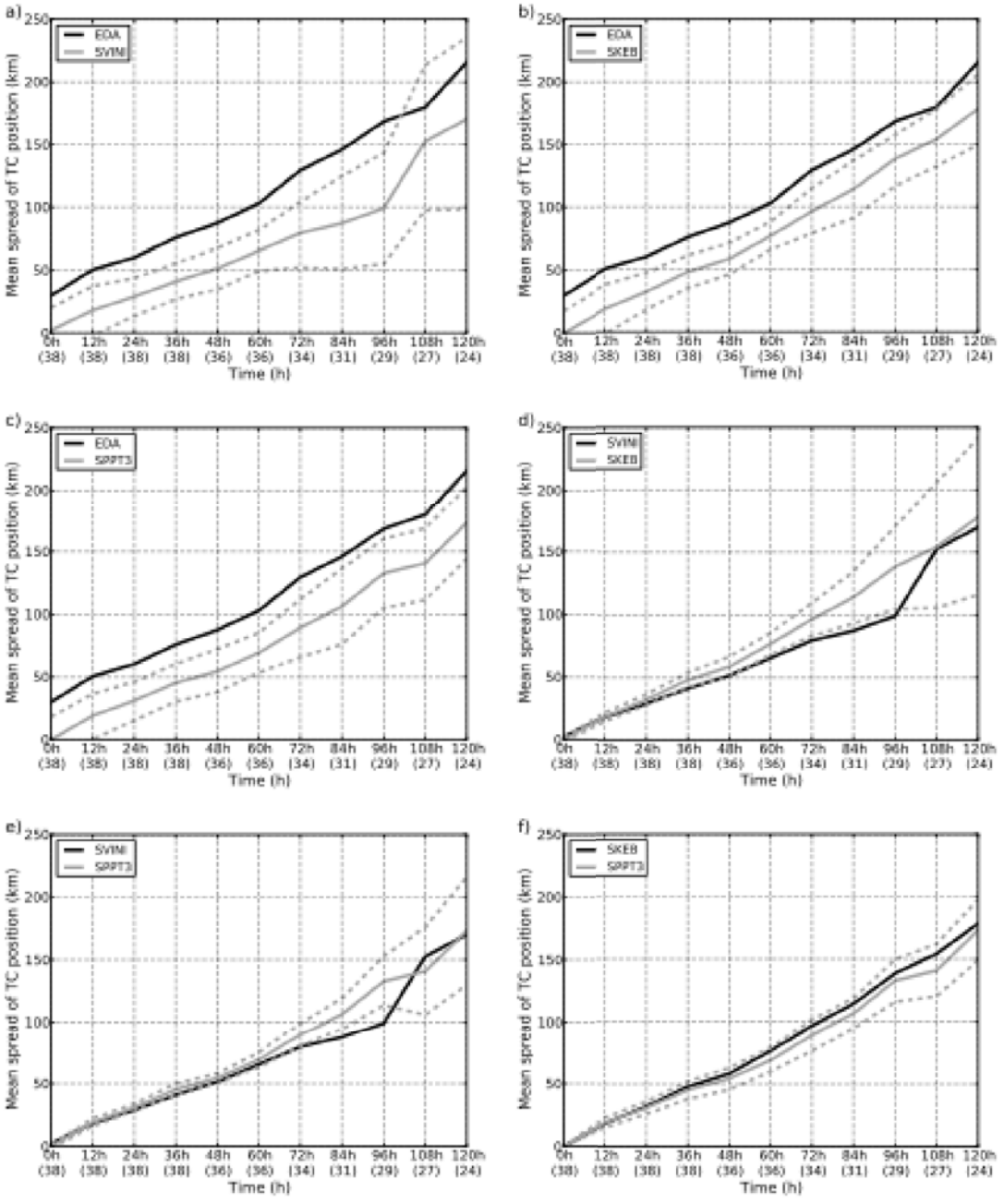

Figure 4.14: Mean ensemble spread of TC track and 95% confidence intervals (grey dashed lines) for the different experiments. The numbers in parentheses indicate how many forecasts were considered for the respective lead time.

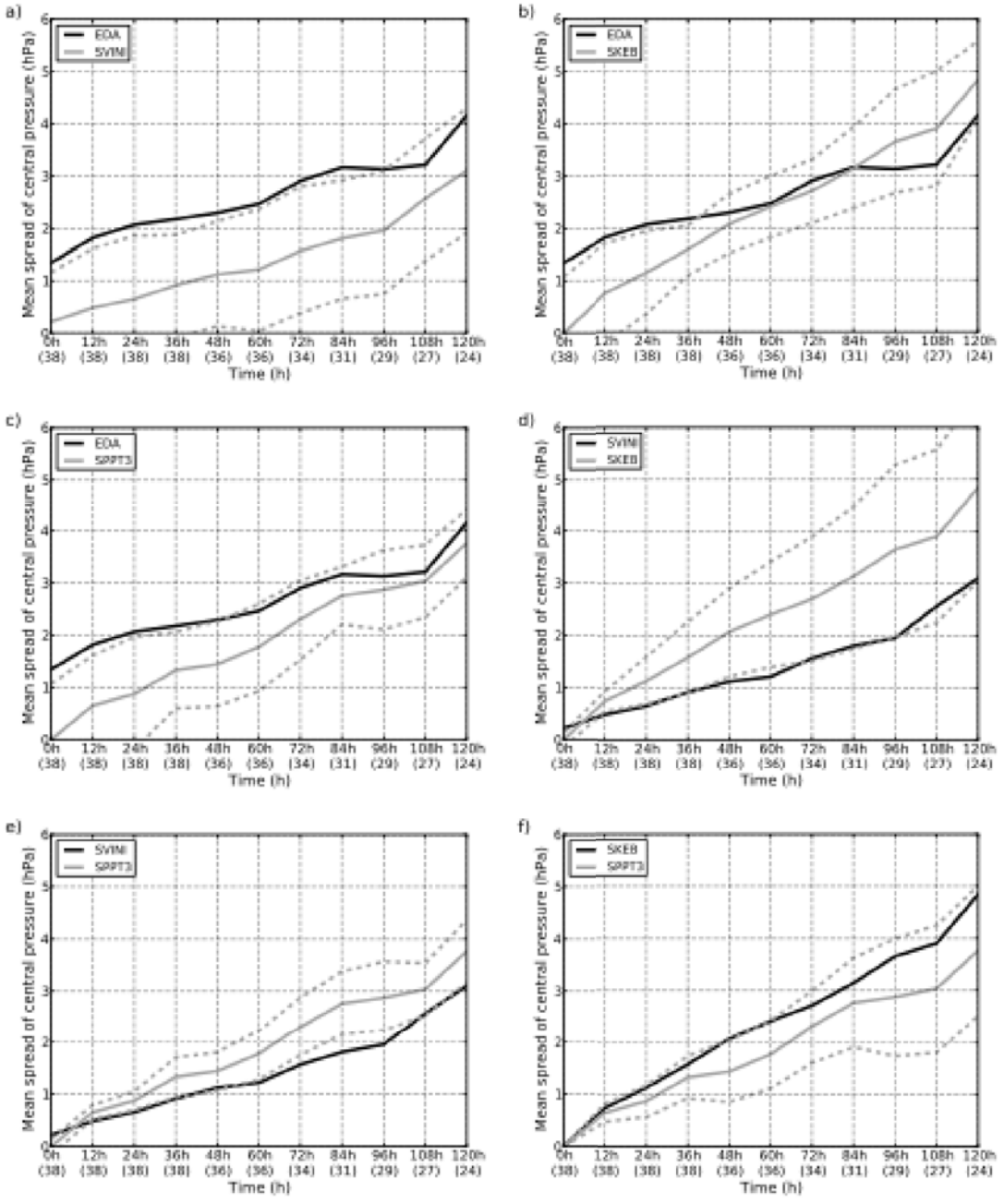

Figure 4.15: Mean ensemble spread of TC central pressure and 95% confidence intervals (grey dashed lines) for the different experiments. The numbers in parentheses indicate how many forecasts were considered for the respective lead time.

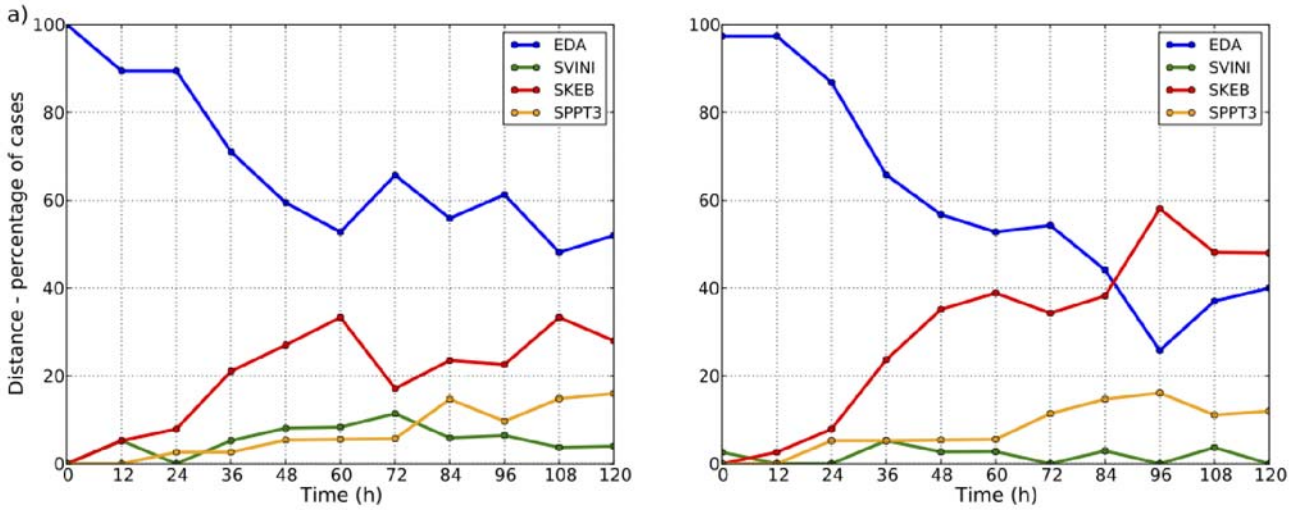

Figure 4.16: Percentage of total cases for which the EDA (blue), SVINI (green), SKEB (red) and SPPT3 (Orange) experiment exhibits the largest ensemble spread of all four experiments for a) track spread and b) central pressure spread.

in terms of total energy. The EDA perturbations dominate the ensemble spread for a rather short time, before the ensemble spread caused by the other methods becomes comparable in magnitude. After two days forecast time, the spread caused by one of the other methods is larger than the spread by the EDA experiment in around 40% of the cases.

A further point of interest is how the ALL50 ensemble performs for TC track prediction. An important indicator for ensemble performance is how well the mean spread of the ensemble compares to the mean error of the ensemble-mean. Furthermore, it is important that the ensemble is able to account for the fact that the uncertainty of the TC position is sometimes quite anisotropic, i.e. that the forecasts errors are more pronounced in one direction of the phase space than in the others.

The mean spread of the ALL50 ensemble corresponds quite well with its mean error (Fig. 4.13). The differences between the two means are not statistically significant within 5 days forecast time. To measure how well the ALL50 ensemble is able to describe the anisotropy in the position uncertainty of the TC, we follow the approach of Hamill et al. (2010). We calculate the average projection of the forecast-errors onto the eigenvectors of the forecast-error covariance matrix of the ensemble. This is then compared with the average projection of the deviation of the individual members from the ensemble-mean onto the eigenvectors. The forecast-error covariance matrix is defined as follows (Hamill et al., 2010):

$$\mathbf{X}\mathbf{X}^T \quad \text{with} \quad \mathbf{X} = \begin{bmatrix} \mathbf{X}'_\lambda \\ \mathbf{X}'_\Phi \end{bmatrix} \tag{4.7}$$

and

$$\mathbf{X}'_\lambda = \left[x_{\lambda(1)} - \bar{x}_{(\lambda)}, \ldots, x_{\lambda(1)} - \bar{x}_{(\lambda(n)}\right] / \sqrt{(N-1)} \tag{4.8}$$

$$\mathbf{X}'_\Phi = \left[x_{\Phi(1)} - \bar{x}_{(\Phi)}, \ldots, x_{\Phi(1)} - \bar{x}_{(\Phi(n)}\right] / \sqrt{(N-1)} \tag{4.9}$$

where $\bar{x}_{(\lambda)}$ and $\bar{x}_{(\Phi)}$ denote the mean longitude and latitude of the TC positions and $x_{\lambda(i)}$ and $x_{\Phi(i)}$ denote the longitude and latitude of the TC position in the ith ensemble member. The number of ensemble members is denoted by N.

The elliptic distribution of the forecast positions of the TCs is shown for the example of Typhoon Jangmi and Typhoon Sinlaku in Figure 4.17 using 90% probability ellipses. These are fitted around the position of the TC in the different ensemble members at the respective forecast time. The ellipses are centred on the ensemble-

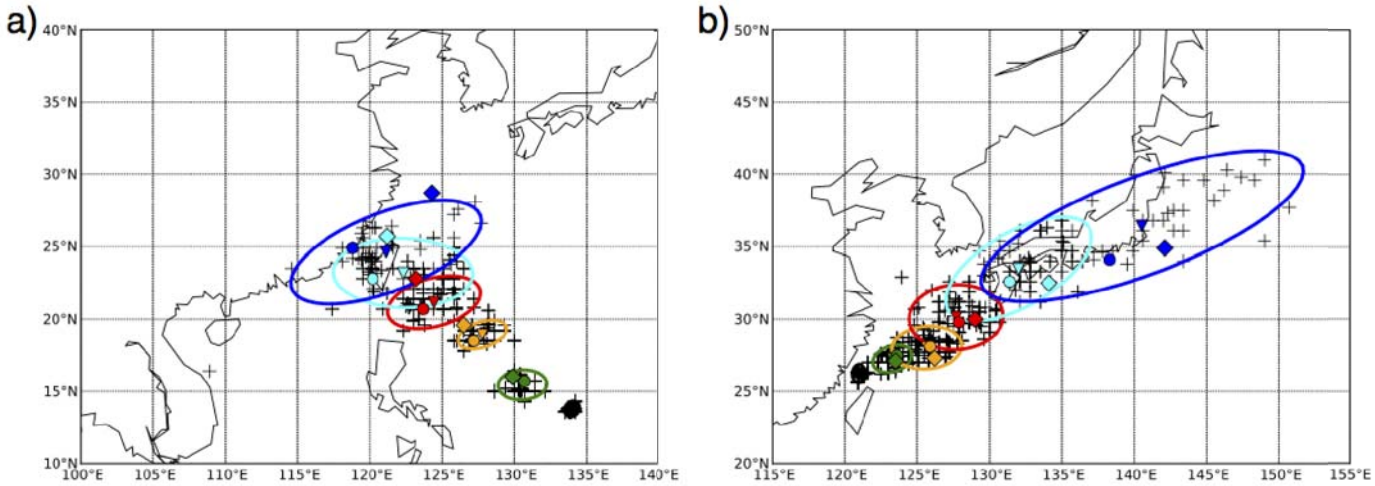

Figure 4.17: Ensemble forecast of Typhoon Jangmi (initialized on 00 UTC 25 September) and Sinlaku (initialized on 00 UTC 15 September). Depicted are the 90% probability ellipses and TC positions (diamond : best track, dot : control forecast, triangle : ensemble-mean, cross : perturbed forecasts). Positions and ellipses are drawn for forecast times of 0 (black), 24 (green), 48 (orange), 72 (red), 96 (cyan) and 120 hours (blue).

mean position of the TCs. The major axes of the ellipses are chosen in such a way that they point in the direction of the leading eigenvector of the forecast-error covariance matrices. As a consequence, the minor axes point in the direction of the second eigenvector. The axes of the ellipses are then enlarged according to the ratio of the eigenvectors until 90% of the TC positions in the ensembles are enclosed by it. The average projection of the forecast-errors and the deviation of the individual ensemble members corresponds quite well for the ALL50 ensemble (Fig. 4.18). On average the forecast-errors posses a larger projection onto the first eigenvector of the forecast-error covariance matrix than on the second one. Thus the ensemble possesses some skill in indicating in which direction of the phase space errors are more pronounced (Hamill et al., 2010). All the other four sub ensembles (EDA, SVINI, SKEB, SPPT3) are heavily under dispersive, especially in the direction of the first eigenvector (not shown).

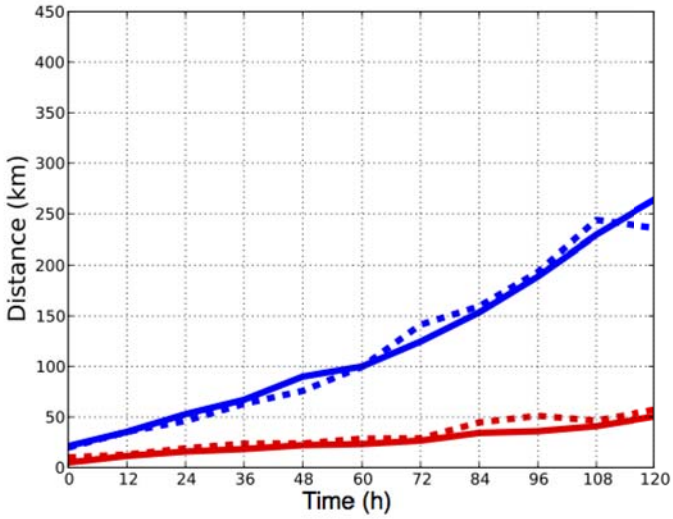

Figure 4.18: Average projection of errors (dashed) and members (solid) of the ALL50 ensemble onto the first (blue) and second (red) eigenvector of the forecast-error covariance matrix.

4.4 Summary

We assessed the impact of the different perturbation methods used within the operational ECMWF EPS on track and intensity forecasts of TCs. Furthermore, we analysed the spatial structure of the perturbations and how it evolves with time.

Projecting the SVINI perturbations onto the EDA perturbations and the perturbations of the SKEB and SPPT3 schemes indicates that these methods excite the growing modes of the flow successfully.

Within the TC, the EDA perturbations are dominated by a TC displacement / intensity change pattern (wavenumber 0 and 1) over time. In contrast, the SVINI perturbations are associated with the TC outer region at the initial time, where they show wavenumber 1 and 2 patterns. The SVINI perturbations then quickly converge towards a displacement pattern within the lower to mid troposphere during the first hours of the forecasts. Initially, there are some differences between the perturbation structures of the SKEB and SPPT3 experiment: the SKEB perturbations possess on average a larger amplitude in the TC outer region, while the SPPT3 perturbations are more focused on the TC core and upper levels. Here, the SKEB and SPPT3 perturbations reflect the properties of their respective generation method. Nevertheless, both schemes force the outer region and the inner core of the TC. This results in considerable track as well as intensity spread. After 48 hours, all the perturbations qualitatively converge towards the pattern of the EDA perturbations. This is consistent with the behaviour of global perturbation patterns that also converge for longer lead times (Magnusson et al., 2009). The EDA perturbations exhibit the largest total energy values during the first 3 days of the forecasts on average. The perturbation amplitude of the other methods, especially of the stochastic tendency perturbation schemes, becomes comparable in magnitude after 24 hours forecast time. Our results show that in the case of a TC there is some redundancy between the different perturbation methods after some forecast time. Hence, in terms of ensemble design, it is not trivial to decide how much variance should be introduced into the ensemble by each method.

The EDA experiment exhibits the largest mean ensemble spread for TC tracks. The mean TC track spread of the SVINI, SKEB and SPPT3 experiments is quite similar and the differences are only marginally statistically significant. In terms of central pressure spread, the mean spread of the EDA ensemble is largest during the first 36 hours of the forecast. At longer lead times, the differences between the experiments are barely statistical significant. The ensemble spread of the EPS is dominated by the EDA perturbations within the first 24 to 36 hours. After that time the spread of the SKEB, SPPT3 and SVINI experiments becomes comparable. After two days forecast time, one of the three experiments exhibits a larger spread than the EDA experiment in about 40% of all TC ensemble forecasts considered in this study. The spread of the ensemble using all the four perturbation methods matches

the TC track error of its ensemble mean quite well. In addition, the ensemble shows skill in capturing the spatial structure of the track errors.

5 Summary

Due to the chaotic nature of the weather a forecast will always be associated with uncertainties. The uncertainties arise both from errors in the initial conditions and errors of the forecast model. At the leading numerical weather prediction centers nowadays ensemble forecasts are used to quantify uncertainties associated with a single forecasts. The ensemble consist of a number of additional forecasts for which the initial conditions and the model physics are perturbed. If the ensemble forecasts properly represents the uncertainties of the particular single weather forecasts, the ensemble forecasts can be used to decide how trustworthy the single forecast is. For example, it is possible to assign a probability to a tropical cyclone track forecast.

In the ensemble prediction system of the European Centre for Medium-Range Weather Forecasts four different methods are applied to account for analysis uncertainty and uncertainty associated with the formulation of the forecasts model. Singular vectors and the ensemble of data assimilations and are used to generate perturbations to the initial conditions, while two stochastic tendency perturbation schemes aim to mimic the effect of model error. The two tendency perturbation schemes are the stochastic kinetic energy backscatter scheme and the stochastically perturbed parametrisation tendency scheme. Detailed knowledge of the properties of the different perturbation methods is essential in order to design future configurations of ensemble prediction systems.

In this study we explored the dynamics and the impact of the different perturbation methods for tropical cyclone forecasts. In the first part of the study we investigated the sensitivity, structure and dynamics of singular vectors associated with Hurricane Helene (2006). The singular vectors correspond to a generalized stability analysis. They identify the regions of the atmospheric flow that are most favorable for perturbation growth and indicate the structure of the fastest growing perturbations to a given forecast. Therefore the singular vectors highlight the processes that dominate the predictability of tropical cyclones. We calculated so called dry and moist singular vectors. For the moist singular vectors diabatic effects are accounted for in the computations. The computations were performed with a spatial resolution of approximately 320 km, 210 km, 125 km and 80 km. At the European Centre for

Medium-Range Weather Forecasts singular vectors are calculated operationally with a resolution of 320 km to generate the singular vector initial perturbations for the ensemble prediction system. To our knowledge this is the first study in which a spatial resolution of 80 km is used to compute global singular vectors targeted on tropical cyclones.

The singular vectors associated with Helene possess a three-dimensional spiral structure within the tropical cyclone. The spirals are tilted in the vertical and in the horizontal against the shear. The tilt indicates that the singular vectors grow by exploiting baroclinic and barotropic mechanisms. Applying higher resolution and accounting for moist effects within the computations significantly influences the structure and growth mechanisms of the singular vectors. At low resolution the singular vector formalism selects structures approximately 500 km from the center of the tropical cyclone. This is also the case for the high resolution dry singular vectors, which are dominated by barotropic structures. However, the high resolution moist singular vectors exhibit new structures within the tropical cyclone core region, approximately 100 to 200 km from Helene's center. These structures are strongly baroclinic. Singular vectors calculated for selected initialization dates for Typhoon Jangmi (2008) and Sinlaku (2008) indicate that effects seen for Hurricane Helene are not limited to a single tropical cyclone case but possess general relevance.

The reason for these differences is that at low resolution the tropical cyclone is not properly represented within the forecast used for the singular vector computations. At low resolution the model cannot represent the strong gradients associated with such an intense system. Hence the tropical cyclone is much weaker and exhibits lower windspeeds, vertical and horizontal shear. For barotropic growth the horizontal shear is important, while baroclinic growth is proportional to vertical shear and the effective static stability. Moist effects reduce the effective static stability of the atmosphere and thereby enhance the potential for baroclinic perturbation growth. As a result regions of low static stability and strong vertical shear within the tropical cyclone core region are identified as favorable for perturbation growth by the high resolution moist singular vector computations.

We have shown that the combined effect of higher resolution and diabatic processes leads to the significant differences in the singular vector structure and that baroclinic growth within the tropical cyclone core region has a strong impact on the predictability of tropical cyclones. Here, the coupling due to moist effects between the cyclonic vortex of the tropical cyclone and the upper level outflow is especially important for the downstream effect of the event. Low resolution singular vectors

fail to exploit this growth mechanism and therefore underestimate the downstream impact of the tropical cyclone.

If the singular vectors are calculated with sufficient resolution, they are able to identify tropical cyclones as one of the most uncertain systems in the tropics. Furthermore, they can be used to quantify the impact of tropical cyclones on the predictability over Europe. This emphasizes the importance of tropical cyclones for the predictability of the whole atmospheric flow. In the context of ensemble forecasting, the strong growth of high resolution singular vectors associated with tropical cyclones yields benefits. It opens up the possibility of including singular vectors targeted on the whole tropics into the ensemble prediction system instead of targeting individual tropical cyclones. To estimate the impact of high resolution singular vectors on the ensemble prediction system, we initialised ensemble forecasts with the singular vectors targeted on Helene. The high resolution moist singular vectors cause a larger ensemble spread regarding wind speed, tropical cyclone track and central pressure on average than the lower resolution singular vectors.

In the second part of our study we analysed what impact the different perturbation methods used in the operational configuration of the ensemble prediction system have on track and intensity forecasts of tropical cyclones. Furthermore, we assessed the performance of the new configuration of the ensemble prediction system for the 2008 tropical cyclone season. This configuration corresponds to the setup operational at European Centre for Medium-Range Weather Forecasts since November 2010. For our analysis we created 5 different ensemble experiments and analysed 13 tropical cyclone cases. For the five different ensemble setups global ensemble forecasts consisting of 21 members with a spatial resolution of approximately 32 km were run from 14 August to 4 October 2008 every 48 hours (equivalent to 3645 individual forecasts). In addition, the ensemble of data assimilations was run from 4 August to 5 October to generate the initial perturbations for the ensemble forecasts (equivalent to 1386 individual 4D-Var analyses).

Using this extensive dataset we have quantified the impact of the different perturbation methods on tropical cyclone forecasts and analysed the spatial properties and growth dynamics of the perturbations. We have shown that the perturbations from the different methods excite the growing modes of the flow, as identified by the singular vectors in case of tropical cyclone events. On average, the perturbations generated from the ensemble of data assimilations dominate the ensemble spread only for a rather short time of approximately 24 hours. The perturbations from the stochastic tendency perturbation schemes grow rapidly and impact both the tropical

cyclone track and central pressure. It is apparent that within the framework of the ensemble prediction system, tropical cyclone forecast errors that arise from model uncertainty quickly approach the magnitude of forecast errors caused by analysis uncertainty.

The two stochastic tendency perturbation schemes force the outer as well as the core region of the tropical cyclones significantly. However, we have shown that within the first hours of the forecasts the perturbations from the stochastic kinetic energy backscatter scheme are distributed more symmetrically around the tropical cyclone than those from the stochastically perturbed parametrisation tendency scheme. These differences in perturbation structure are caused by the different characteristics of the model variables used within the schemes to estimate the model error.

The perturbations from the ensemble of data assimilations and the perturbations from the singular vectors also show significant differences at the initial time of the forecasts. While the singular vectors are located in the outer region of the tropical cyclones, the perturbations due to the ensemble of data assimilations possess significant amplitude within the tropical cyclone core and outflow. Here they are dominated by a tropical cyclone displacement pattern. However, after 48 hours forecast-time, the perturbations from all four methods show some level of convergence towards a tropical cyclone shift and intensity change pattern.

Our results show that small scale perturbations within tropical cyclones can cause large synoptic scale forecast errors by influencing the tropical cyclone track, intensity and outflow. This is a challenging problem for numerical weather prediction, since state of the art global models and data assimilation systems still cannot resolve the tropical cyclone core properly. In terms of ensemble forecasting the perturbation methods need to account for the large variety of relevant scales to properly represent the uncertainties associated with tropical cyclones and their downstream impacts.

The ensemble of data assimilations and the stochastic tendency perturbation schemes generate effectively growing perturbations for tropical cyclone ensemble forecasting. In contrast to the purely dynamically motivated singular vector perturbations these methods aim to account for the actual uncertainty of a forecast. The perturbation patterns reflect the properties of their respective generation methods during the early forecast range, while there is some redundancy between the different perturbation methods after some forecast time. Hence, evaluating the ensemble forecasts during the early forecast range will be essential to evaluate how realistic

the perturbations generated from the different methods are and to decide and how much variance should be introduced into the ensemble by each method.

In future work we will analyse selected tropical cyclone cases to investigate the structural changes of the tropical cyclones caused by the different perturbations in greater detail. We will assess whether the strength of the tropical cyclone or the stage of the tropical cyclone life (e.g. before or after recurvature) impacts the growth and structure of the perturbation generated by the different methods. Furthermore, we will investigate for a large number of cases what impact increased resolution of the singular vector computations has on the properties and impact of the singular vector perturbations.

References

Ancell, B. C. and C. F. Mass, 2006: Structure, growth rates, and tangent linear accuracy of adjoint sensitivities with respect to horizontal and vertical resolution. *Mon. Wea. Rev.*, **134**, 2971–2988.

Ancell, B. C. and C. F. Mass, 2008: The variability of adjoint sensitivity with respect to model physics and basic-state trajectory. *Mon. Wea. Rev.*, **136**, 4612–4628.

Anwender, D., P. A. Harr, and S. C. Jones, 2008: Predictability associated with the downstream impacts of the extratropical transition of tropical cyclones: Case studies. *Mon. Wea. Rev.*, **136**, 3226–+.

Anwender, D., S. C. Jones, M. Leutbecher, and P. A. Harr, 2010: Sensitivity experiments for ensemble forecasts of the extratropical transition of typhoon Tokage (2004). *Q. J. R. Meteorol. Soc.*, 183–200.

Badger, J. and B. J. Hoskins, 2000: Simple initial value problems and mechanisms for baroclinic growth. *J. Atmos. Sci.*, **58**, 38–49.

Barkmeijer, J., R. Buizza, T. N. Palmer, and J.-F. Mahfouf, 2001: Tropical singular vectors computed with linearized diabatic physics. *Q. J. R. Meteorol. Soc.*, **127**, 685–708.

Bechtold, P., M. Köhler, T. Jung, F. Doblas-Reyes, M. Leutbecher, M. J. Rodwell, F. Vitart, and G. Balsamo, 2008: Advances in simulating atmospheric variability with the ECMWF model: From synoptic to decadal time-scales. *Q. J. R. Meteorol. Soc.*, **134**, 1337–1351.

Bennetts, D. A. and B. J. Hoskins, 1979: Conditional symmetric instability - a possible explanation for frontal rainbands. *Q. J. R. Meteorol. Soc.*, **105**, 945–962.

Berner, J., G. J. Shutts, M. Leutbecher, and T. N. Palmer, 2009: A Spectral Stochastic Kinetic Energy Backscatter Scheme and Its Impact on Flow-Dependent Predictability in the ECMWF Ensemble Prediction System. *J. Atmos. Sci.*, **66**, 603–626.

Brown, 2006: Tropical cyclone report Hurricane Helene. National Hurricane Center. http://www.nhc.noaa.gov/pdf/TCR-AL082006_Helene.pdf.

Buizza, R., 1994: Localization of optimal perturbations using a projection operator. *Q. J. R. Meteorol. Soc.*, **120**, 1647–1681.

Buizza, R., 1995: Optimal perturbation time evolution and sensitivity of ensemble prediction to perturbation amplitude. *Quart. J. Roy. Meteor. Soc.*, **121**, 1705–1738.

Buizza, R., R. Gelaro, F. Molteni, and T. Palmer, 1997: The impact of increased resolution on predictability studies with singular vectors. *Q. J. R. Meteorol. Soc.*, **123**, 1007–1033.

Buizza, R., M. Leutbecher, and L. Isaksen, 2008: Potential use of an ensemble of analyses in the ECMWF ensemble prediction system. *Quart. J. Roy. Meteor. Soc.*, **134**, 2051–2066.

Buizza, R., M. Miller, and T. N. Palmer, 1999: Stochastic representation of model uncertainties in the ECMWF ensemble prediction system. *Q. J. R. Meteorol. Soc.*, **125**, 2887–2908.

Buizza, R. and T. N. Palmer, 1995: The Singular-Vector Structure of the Atmospheric Global Circulation. *J. Atmos. Sci.*, **52**, 1434–1456.

Buizza, R., J. Tribbia, F. Molteni, and T. N. Palmer, 1993: Computation of optimal unstable structures for a numerical weather prediction model. *Tellus*, **45A**, 388–407.

Chan, J. C. L. and J. D. Kepert, (Eds.) , 2010: *Global Perspectives on Tropical Cyclones From Science to Mitigation*. World Scientific Publishing Co. Pte. Ltd.

Chen, J.-H., M. S. Peng, C. A. Reynolds, and C.-C. Wu, 2009: Interpretation of tropical cyclone forecast sensitivity from the singular vector perspective. *J. Atmos. Sci.*, **66**, 3383–3400.

Courtier, P., J.-N. Thépaut, and A. Hollingsworth, 1994: A strategy for operational implementation of 4d-var, using an incremental approach. *Q. J. R. Meteorol. Soc.*, **120**, 1367–1387.

Coutinho, M. M., B. J. Hoskins, and R. Buizza, 2004: The influence of physical processes on extratropical singular vectors. *J. Atmos. Sci.*, **61**, 195–209.

Durran, D. R. and J. B. Klemp, 1982: On the Effects of Moisture on the Brunt-Väisälä Frequency. *J. Atmos. Sci.*, **39**, 2152–2158.

Eady, E. T., 1949: Long waves and cyclone waves. *Tellus*, **1**, 33–52.

Ehrendorfer, M. and J. Tribbia, 1997: Optimal prediction of forecast error covariance through singular vectors. *J. Atmos. Sci.*, **54**, 286–313.

Emanuel, K., 2003: Tropical Cyclones. *Annu. Rev. Earth Planet Sci.*, **31**, 75–104.

Emanuel, K. A., 1989: The finite-amplitude nature of tropical cyclogenesis. *J. Atmos. Sci.*, **46**, 3431–3456.

Errico, R. M., 1997: What is an adjoint model? *Bull. Amer. Meteor. Soc.*, **78**, 2577–2591.

Farrell, B. F., 1982: The initial growth of disturbances in a baroclinic flow. *J. Atmos. Sci.*, **39**, 1663–1686.

Farrell, B. F. and P. J. Ioannou, 1996a: Generalized stability theory. Part I: Autonomous operators. *J. Atmos. Sci.*, **53**, 2025–2040.

Farrell, B. F. and P. J. Ioannou, 1996b: Generalized stability theory. Part II: Nonautonomous operators. *J. Atmos. Sci.*, **53**, 2041–2053.

Fiorino, M. and R. L. Elsberry, 1989: Some Aspects of Vortex Structure Related to Tropical Cyclone Motion. *J. Atmos. Sci.*, **46**, 975–990.

Gilmour, I., L. A. Smith, and R. Buizza, 2001: Linear regime duration: Is 24 hours a long time in synoptic weather forecasting? *J. Atmos. Sci.*, **58**, 3525–3539.

Grams, C. M., et al., 2011: The key role of diabatic processes in modifying the upper-level tropospheric wave guide: a North Atlantic case study. *Q. J. R. Meteorol. Soc.*, in press.

Hamill, T. M., 1999: Hypothesis tests for evaluating numerical precipitation forecasts. *Wea. Forecasting*, **14**, 155–167.

Hamill, T. M., J. S. Whitaker, M. Fiorino, and S. G. Benjamin, 2010: Global Ensemble Predictions of 2009's Tropical Cyclones Initialized with an Ensemble Kalman Filter. *Mon. Wea. Rev.*, **139**, 668–688.

Harr, P. A., D. Anwender, and S. C. Jones, 2008: Predictability associated with the downstream impacts of the extratropical transition of tropical cyclones: Methodology and a case study of Typhoon Nabi (2005). *Mon. Wea. Rev.*, **136**, 3205–+.

Hartmann, D. L., R. Buizza, and T. N. Palmer, 1995: Singular vectors: The effect of spatial scale on linear growth of disturbances. *J. Atmos. Sci.*, **52**, 3885–3894.

Hodyss, D. and S. J. Majumdar, 2007: The contamination of 'data' impact in global models by rapidly growing mesoscale instabilities. *Quart. J. Roy. Meteor. Soc.*, **133**, 1865–1875.

Holton, J. R., 2004: *An introduction to dynamic meteorology*. Fourth Edition, Academic Press.

Hoskins, B. J., R. Buizza, and J. Badger, 2000: The nature of singular vector growth and structure. *Q. J. R. Meteorol. Soc.*, **126**, 1565–1580.

Hoskins, B. J., M. E. McIntyre, and A. W. Robertson, 1985: On the use and significance of isentropic potential vorticity maps. *Q. J. R. Meteorol. Soc.*, **111**, 877–946.

Hoskins, B. J. and P. J. Valdes, 1990: On the existence of storm-tracks. *J. Atmos. Sci.*, **47**, 1854–1864.

IFS Documentation, 2010: ECMWF IFS Documentation Cycle 36r1. http://www.ecmwf.int/research/ifsdocs/CY36r1/index.html.

Isaksen, L., M. Bonavita, R. Buizza, M. Fisher, J. Haseler, M. Leutbecher, and L. Raynaud, 2010: Ensemble of Data Assimilations at ECMWF. *ECMWF Technical Memorandum*, **No. 636**.

Jones, S. C., 2000: The evolution of vortices in vertical shear. III: Baroclinic vortices. *Q. J. R. Meteorol. Soc.*, **126**, 3161–3185.

Jones, S. C. and A. J. Thorpe, 1992: The Three-Dimensional Nature of 'Symmetric' Instability. *Q. J. R. Meteorol. Soc.*, **118**, 227–258.

Jones, S. C., et al., 2003: The Extratropical Transition of Tropical Cyclones: Forecast Challenges, Current Understanding, and Future Directions. *Weather and Forecasting*, **18**, 1052–1092.

Kalnay, E., 2003: *Atmospheric Modeling Data Assimilation and Predictability.* Cambridge University Press, University of Maryland.

Keller, J. H., S. C. Jones, J. L. Evans, and P. Harr, 2011: Characteristics of the TIGGE multimodel ensemble prediction system in representing forecast variability associated with Extratropical Transition. *Geophys. Res. Lett.*, L12802.

Kim, H. M. and B.-J. Jung, 2009a: Influence of moist physics and norms on singular vectors for a tropical cyclone. *Mon. Wea. Rev.*, **137**, 525–543.

Kim, H. M. and B.-J. Jung, 2009b: Singular vector structure and evolution of a recurving tropical cyclone. *Mon. Wea. Rev.*, **137**, 505–524.

Knapp, K. R., M. C. Kruk, D. H. Levinson, H. J. Diamond, and C. J. Neumann, 2010: The International Best Track Archive for Climate Stewardship (IBTrACS): Unifying tropical cyclone best track data. *Bull. Amer. Meteor. Soc.*, **91**, 363–376.

Komori, T. and T. Kadowaki, 2010: Resolution Dependence of Singular Vectors Computed for Typhoon SINLAKU. *SOLA*, **6**, 45–48.

Kwon, Y. C. and W. M. Frank, 2005: Dynamic instabilities of simulated hurricane-like vortices and their impacts on the core structure of hurricanes. Part I: Dry experiments. *J. Atmos. Sci.*, **62**, 3955–3973.

Kwon, Y. C. and W. M. Frank, 2008: Dynamic instabilities of simulated hurricane-like vortices and their impacts on the core structure of hurricanes. Part II: Moist experiments. *J. Atmos. Sci.*, **65**, 106–122.

Lang, S. T. K., S. C. Jones, M. Leutbecher, M. S. Peng, and C. A. Reynolds, 2011: Sensitivity, structure and dynamics of singular vectors associated with Hurricane Helene (2006). *J. Atmos. Sci.*, accepted.

Leutbecher, M., 2003: A Reduced Rank Estimate of Forecast Error Variance Changes due to Intermittent Modifications of the Observing Network. *J. Atmos. Sci.*, **60**, 729–742.

Leutbecher, M., 2005: On Ensemble Prediction Using Singular Vectors Started from Forecasts. *Mon. Wea. Rev.*, **133**, 3038–3046.

Leutbecher, M., 2007: On the representation of initial uncertainties with multiple sets of singular vectors optimized for different criteria. *Q. J. R. Meteorol. Soc.*, **133**, 2045–2056.

Leutbecher, M. and T. N. Palmer, 2008: Ensemble Forecasting. *Journal Computational Physics*, **227**, 3515–3539.

Lopez, P. and E. Moreau, 2005: A convection scheme for data assimilation: Description and initial tests. *Q. J. R. Meteorol. Soc.*, **131**, 409–436.

Lord Rayleigh, J. W. S., 1880: On the stability, or instability, of certain fluid motions. *Proc. London Math. Soc.*, **11**, 57–70.

Lorenz, E. N., 1965: A study of predictability of a 28-variable atmospheric model. *Tellus*, **17**, 321–333.

Magnusson, L., J. Nycander, and E. Källén, 2009: Flow-dependent versus flow-independent initial perturbations for ensemble prediction. *Tellus A*, **61**, 194–209.

Mahfouf, J.-F., 1999: Influence of physical processes on the tangent-linear approximation. *Tellus*, **51A**, 147–166.

Merrill, R. T., 1988: Characteristics of the Upper-Tropospheric Environmental Flow around Hurricanes. *J. Atmos. Sci.*, **45**, 1665–1677.

Miller, M., R. Buizza, J. Haseler, M. Hortal, P. Janssen, and A. Untch, 2010: Increased resolution in the ECMWF deterministic and ensemble prediction systems. *ECMWF Newsletter No. 124*, 10–16.

Montgomery, M. T. and L. J. Shapiro, 1995: Generalized Charney-Stern and Fjortoft theorems for rapidly rotating vortices. *J. Atmos. Sci.*, **52**, 1829–1833.

Moscatello, A., M. M. Miglietta, and R. Rotunno, 2008: Observational analysis of a Mediterranean "hurricane" over south-eastern Italy. *Weather*, **63**, 306–311.

Nolan, D. S. and B. F. Farrell, 1999: Generalized stability analyses of asymmetric disturbances in one- and two-celled vortices maintained by radial inflow. *J. Atmos. Sci.*, **56**, 1282–1307.

Nolan, D. S. and M. T. Montgomery, 2002: Nonhydrostatic, three-dimensional perturbations to balanced, hurricane-like vortices. Part I: Linearized formulation, stability, and evolution. *J. Atmos. Sci.*, **59**, 2989–3020.

Orr, W. M., 1907: The stability or instability of the steady motions of a perfect liquid and of a viscous liquid. *Proc. Roy. Irish Acad.*, **A27**, 9–69.

Palmer, T. N., R. Buizza, F. Doblas-Reyes, T. Jung, M. Leutbecher, G. J. Shutts, M. Steinheimer, and A. Weisheimer, 2009: Stochastic Parametrization and Model Uncertainty. *ECMWF Technical Memorandum*, **No. 598**.

Palmer, T. N., R. Gelaro, J. Barkmeijer, and R. Buizza, 1998: SVs, metrics and adaptive observations. *J. Atmos. Sci.*, **55**, 633–653.

Pedlosky, J., 1987: *Geophysical Fluid Dynamics*. 2nd edition, Springer-Verlag, New York.

Peng, J., T. Li, M. S. Peng, and X. Ge, 2009: Barotropic instability in the tropical cyclone outer region. *Q. J. R. Meteorol. Soc.*, **135**, 851–864.

Peng, M. S. and C. A. Reynolds, 2006: Sensitivity of tropical cyclone forecasts as revealed by singular vectors. *J. Atmos. Sci.*, **63**, 2508–2528.

Persson, A., 2005: User Guide to ECMWF forecast products. Meteorological Bulletin M4.0.

Puri, K., J. Barkmeijer, and T. N. Palmer, 2001: Ensemble prediction of tropical cyclones using targeted diabatic singular vectors. *Q. J. R. Meteorol. Soc.*, **127**, 709–731.

Reynolds, C., R. Gelaro, and J. D. Doyle, 2001: Relationship between singular vectors and transient features in the background flow. *Q. J. R. Meteorol. Soc.*, **127**, 1731–1760.

Reynolds, C. A., J. G. McLay, J. S. Goerss, E. A. Serra, D. Hodyss, , and C. R. Sampson, 2011: Impact of Resolution and Design On the U.S. Navy Global Ensemble Performance in the Tropics. *Mon. Wea. Rev.*, in press.

Reynolds, C. A. and T. E. Rosmond, 2003: Nonlinear growth of singular-vector-based perturbations. *Q. J. R. Meteorol. Soc.*, **129**, 3059–3078.

Riemer, M., S. C. Jones, and C. A. Davis, 2008: The impact of extratropical transition on the downstream flow: an idealised modelling study with a straight jet. *Q. J. R. Meteorol. Soc.*, **134**, 69–91.

Schubert, W. H., M. T. Montgomery, R. K. Taft, T. A. Guinn, S. R. Fulton, J. P. Kossin, and J. P. Edwards, 1999: Polygonal Eyewalls, Asymmetric Eye Contraction, and Potential Vorticity Mixing in Hurricanes. *J. Atmos. Sci.*, **56**, 1197–1223.

Schultz, D. M. and P. N. Schumacher, 1999: The use and misuse of conditional symmetric instability. *Mon. Wea. Rev.*, **127**, 2709–2732.

Shutts, G., 2005: A kinetic energy backscatter algorithm for use in ensemble prediction systems. *Q. J. R. Meteorol. Soc.*, **131**, 3079–3102.

Tippett, M. K., 1999: Transient moist baroclinic instability. *Tellus*, **51A**, 273–288.

Tompkins, A. M. and M. Janiskova, 2004: A cloud scheme for data assimilation: Description and initial tests. *Q. J. R. Meteorol. Soc.*, **130**, 2495–2517.

van der Grijn, G., J. E. Paulsen, F. Lalaurette, and M. Leutbecher, 2004: Early medium-range forecasts of tropical cyclones. *ECMWF Newsletter*, **102**, 7–14.

Veren, D., J. L. Evans, S. Jones, and F. Chiaromonte, 2009: Novel Metrics for Evaluation of Ensemble Forecasts of Tropical Cyclone Structure. *Mon. Weather Rev.*, **137**, 2830–2850.

Vitart, F., D. Anderson, and T. Stockdale, 2003: Seasonal forecasting of tropical cyclone landfall over Mozambique. *J. Climate*, **16**, 3932–3945.

Vitart, F., J. L. Anderson, and W. F. Stern, 1997: Simulation of interannual variability of tropical storm frequency in an ensemble of GCM integrations. *J. Climate*, **10**, 745–760.

Waliser, D. E., et al., 2011: The "Year" of Tropical Convection (May 2008 to April 2010): Climate Variability and Weather Highlights. *submitted to Bull. Amer. Meteor. Soc.*

Wu, C.-C. and K. Emanuel, 1993: Interaction of a Baroclinic Vortex with Background Shear: Application to Hurricane Movement. *J. Atmos. Sci.*, **50**, 62–76.

Yamaguchi, M. and S. J. Majumdar, 2010: Using TIGGE data to diagnose initial perturbations and their growth for tropical cyclone ensemble forecasts. *Mon. Wea. Rev.*, **138**, 3634–3655.

Yamaguchi, M., D. S. Nolan, M. Iskandarani, S. J. Majumdar, M. S. Peng, and C. A. Reynolds, 2011: Singular vectors for tropical cyclone-like vortices in a nondivergent barotropic framework. *J. Atmos. Sci.*, in press.

YOTC, 2011: Year of Tropical Convection. http://www.ucar.edu/yotc/.

Zeng, Q.-C., 1983: The evolution of a Rossby-wave packet in a three-dimensional baroclinic atmosphere. *J. Atmos. Sci.*, **40**, 73–84.

Acknowledgments

Mein größtmöglicher Dank gebührt Prof. Dr. Sarah Jones für die wissenschaftliche und menschliche Betreuung dieser Arbeit. Vielen Dank Sarah!

Ich bedanke mich bei Prof. Dr. Christoph Kottmeier für die Übernahme des Korreferats.

Ich möchte mich im höchsten Maße und von ganzem Herzen bei Dr. Martin Leutbecher für die Hilfe beim Aufsetzen der numerischen Experimente, für seine Zeit, die vielen motivierenden Worte und die zahlreichen erhellenden Diskussionen bedanken.

Ich bin überaus dankbar dafür, dass ich die Möglichkeit hatte das EZMW für zwei Forschungsaufenthalte zu besuchen.

Ich möchte mich herzlich bei Dr. Carolyn Reynolds und Dr. Melinda Peng für die motivierenden und interessanten Diskussionen und die hilfreichen Kommentare bedanken. Des weiteren danke ich ihnen, dass sie mir den Besuch des Naval Research Laboratory ermöglicht haben. Der Aufenthalt wurde vom Global Visiting Scientist Program des Naval Research Laboratory and des Office of Naval Research finanziert.

Ebenfalls möchte ich herzlich Dr. Jan Barkmejier für die wissenschaftlichen Diskussionen bezüglich der tropischen SVs danken.

Ich möchte von ganzem Herzen Professor Dr. Patrick Harr für seine Gastfreundschaft und für die Ermöglichung des Aufenthalts an der Naval Postgraduate School danken.

Ich bedanke mich bei Dr. Lars Isaksen und Dr. Massimo Bonavita für ihre Hilfe beim Aufsetzen des EDA-Experiments.

Mein großer Dank gebührt auch Dr. Carsten Maass und seinen Kollegen vom

ECMWF User Support für die Beantwortung meiner zahllosen technischen Fragen bezüglich der ECMWF Computer-Infrastruktur.

Von ganzem Herzen Danke ich meinen Kollegen Dr. Leonhard Scheck, Christian Grams, Julia Keller und Dr. Doris Anwender für ihre Unterstützung. Insbesondere möchte ich Dr. Leonhard Scheck für die zahlreichen Diskussionen und Worte der Motivation danken.

Diese Arbeit wurde durch die DFG als Teil der Forschergruppe PANDOWAE (FOR 896) finanziert. Die Nutzung der ECMWF Computer-Infrastruktur war Dank des ECMWF Special Projects “The impact of tropical cyclones on extratropical predictability” möglich.